Control of Interfacial Microstructure in Solid State Diffusion Bonding of Silicon Nitride using Active Metallic Elements

Masakatsu MAEDA

September, 2003

CONTENTS

Control of Interfacial Microstructure in Solid State Diffusion Bonding of Silicon Nitride using Active Metallic Elements

Masakatsu MAEDA

Chapter 1 Introduction

I. Motivation

The livelihood range of the globe is getting severely damaged [1.1]. As the result of our economical and industrial activities, the emission rate of wastes, which are generally hazardous to the environment and to our lives, is increasing [1.1, 1.2]. It has become difficult to consider that our posterity of two generations later or three can successfully inherit the beautiful part of the earth as is, as far as we continue to emit the hazardous wastes [1.3, 1.4].

Since the era of the Industrial Revolution, science and technology have taken the most essential part in establishment of highly developed social infrastructure. Progress in those science and technology has supported innovative inventions and enriched our lives. On the counterpart of such enriched lives, however, severe problems [1.1–1.5] have risen by incorrect utilization of unaccomplished technologies or by wasteful uses of resources, such as wars. Human beings have to overcome these problems also by their wisdom and technology to maintain their civilization and culture or even to survive. That is to implement a sustainable development of our society [1.1].

The problem of energy resources has been one of the most vital problems in Japan, in which little petroleum nor nuclear fuel can be mined [1.6, 1.7]. On the other hand, growth in economy has been kept increasing the consumption amount of energy, resulting in the continuous increase of the social demand to improve the energy efficiency in the industry; especially in the power plants and the transportation services.

Among numerous types of electric power generators, steam-driven turbine systems supply the largest amount of energy [1.7]. Improvement in the energy efficiency for turbine generators corresponds to raise the operation temperature of the turbines. Thus, the problem

of energy resources is effectively alleviated by raising the operation temperature of turbine generators. Furthermore, to raise the operation temperature of turbine generators will reduce the emission of greenhouse gas in the cases of coal- or oil-fired power plants. However, metallic materials for turbine blades, which have to endure high temperature and high pressure of extremely corrosive steam environment, have reached the limit of their operation temperature [1.8]. The turbines of the latest age are operated at approximately 1900 K, which is 600 K higher temperature than that materials can directly endure, by installation of active gas-film cooling system and advanced coating technologies [1.8-1.14]. To improve the operation temperature, development of a new breaking-through technology to replace the conventional materials with advanced refractory materials is necessary for the components enduring the most severe environment in the turbine systems [1.8-1.22].

To improve the energy efficiency in the services of aerospace, locomotive, automotive and marine transportation, the mass-reduction of the vehicles is the most effective solution. Since such mass-reduction must be performed retaining the strength of the vehicle-structure, the solution corresponds to increase the strength-to-mass ratio of the components. Especially, the mass of the rocket, jet or internal-combustion engines will be reduced by replacing the conventional materials with advanced refractory materials [1.23-1.27].

Some of the fine-ceramic materials such as silicon nitride (Si_3N_4) are the candidates for the heat-resistive and mass-saving structural applications as the advanced refractory materials to replace conventional materials [1.8-1.27]. They perform excellent chemical stability, strength and resistivity against creep and wear at high temperatures, with low specific density. **Table 1.1** shows some mechanical and thermal properties of Si_3N_4 in comparison with conventional heat-resistive nickel superalloys [1.22]. The table indicates clearly that the application of Si_3N_4, replacing nickel superalloys, benefits from the high-temperature strength to make the operating temperature higher, from the low specific density to reduce the mass of rotating components, and from the low thermal expansion property and high thermal-shock resistivity to applications in which temperature changes drastically. Moreover, the less usage of precious elements approves the stable supply of the fine-ceramic materials.

These characteristics of fine-ceramics, which are difficult to achieve with metallic materials, are originated from the state of atomic connection in them. In contrast with metallic

Table 1.1 Mechanical and thermal properties of silicon nitride and conventional heat-resistive nickel superalloys. [1.22, 1.28]

Properties		Si_3N_4	Ni superalloys
Melting point or decomposition temperature, T / K		2173 (decomp.)	1623~1723 (m.p.)
Specific density, ρ / 10^3 kg m^{-3}		3.2	~8
Young's modulus, E / GPa		290 ~ 320	~200
Thermal linear expansion coefficient, α / 10^{-6} K^{-1}		3.2	~13
Heat conduction coefficient, μ / W m^{-1} K^{-1}		~25	~40
Vickers Hardness, H_V		~1700	~300
Tensile Strength, σ_f / MPa	at room temperature	300~600	~1000
	at 1073 K	300~600	~500
	at 1473 K	200~400	–
Elongation, $\delta l / l$ (%)		0.2	~20
Fracture toughness, K_C / MPa $m^{1/2}$		4~8	~100
Thermal shock resistivity, ΔT_f / K		500~1200	>1000

materials, the electrons connecting the constituent atoms in fine-ceramics are very localized, *i.e.*, each pair of atoms are connected covalently or ionically [1.29]. Materials, in which valence electrons are localized, are hardly deformed plastically because the glide of the dislocations in them are significantly restricted compared to that in metallic bonded materials. On the other hand, such chemical state of fine-ceramics implies that the ordinary processing techniques for metallic materials, such as welding, cannot be easily applied for the processing of fine-ceramic materials.

To establish a technology to enhance the utilization of fine-ceramics by overcoming the problems for the actual application of the materials will be necessary for the implementation of the sustainable development of our society.

II. Silicon Nitride and Its Position in Structural Fine-Ceramics

A. Silicon Nitride Compared to Other Fine-Ceramics for High-Temperature Structures

Fine-ceramic materials are the nonmetallic inorganic-materials produced with artificial procedures controlled to exhibit the characteristics of the substances by eliminating defects such as impurities and voids [1.30]. Numerous fine-ceramic materials have been developed and applied to practical use to take the advantages of their properties. Recently, fine-ceramic materials are applied in high-temperature structures, bio-medical structures or functional

Table 1.2 List of some characteristics of silicon nitride in comparison with some other representative structural fine-ceramic materials. [1.22, 1.28, 1.31]

Properties	Ceramic materials (dense body)			
	Si_3N_4	SiC	Al_2O_3	ZrO_2
Apparent density, ρ_V / 10^3 kg m^{-3}	3.2	3.16 ~ 3.22	3.6 ~ 3.99	5.43 ~ 6.0
Vickers hardness, H_{VI}	1420	2240 ~ 2350	1200 ~ 1630	1090 ~ 1350
3-point flexural strength, σ_f / MPa	610	450 ~ 540	310 ~ 390	750 ~ 1470
Young's modulus, E / GPa	290	430 ~ 440	280 ~ 370	200 ~ 220
Poisson's ratio, ν	0.28	0.16 ~ 0.17	0.23	0.31
Fracture toughness, K_C / MPa m$^{1/2}$	5	2 ~ 5	3 ~ 4	4 ~ 8
Linear expansion coefficient, α / 10^{-6} K^{-1}	3.2	4.4	7.7 ~ 8.1	10.5 ~ 11.3
Thermal conductivity (293 K), μ / W m^{-1}K^{-1}	20	60 ~ 200	8 ~ 32	3
Thermal shock resistivity, ΔT_f / K	823	673	473 ~ 593	573 ~ 723

devices (filters, sensors, catalysts, insulators, semiconductors, ion-conductors, piezoelectric devices, solid-state-lasers, *etc.*) and still extending the field of application [1.22].

The properties of fine-ceramic materials emphasized in high-temperature structural applications are the strength, elastic modulus, fracture toughness, resistivity against wear and corrosion, and the mass-reduction efficiency. Silicon nitride (Si_3N_4), silicon carbide (SiC), alumina (Al_2O_3) and zirconia (ZrO_2) are the major substances recently used for this purpose. In the following paragraph, the properties of Si_3N_4 is described in comparison with these fine-ceramics, focusing on those emphasized in high-temperature structural applications.

The properties of Si_3N_4 used in the present study are listed in **Table 1.2**, in comparison with some other representative structural fine-ceramics. SiC provides an excellent hardness, low density and high thermal conductivity. Its high resistivity against wear, chemical and thermal corrosion and erosion is suitable for protective coatings of the components used in high temperatures. Al_2O_3 provides a good hardness, high oxidation resistivity and low density in a low cost. In addition, it can be sintered to a dense body without sintering agents. Al_2O_3 is practically used as crucibles, heat-resistive coatings and tiles for furnace walls. ZrO_2, especially the yttria-doped partially stabilized zirconia (Y_2O_3-PSZ), performs an excellent fracture toughness and strength, with extremely low thermal conductivity and high oxidation resistivity. The high ductility of ZrO_2 is originated from its peculiar stress-induced martensitic transformation. Based on these characteristics, ZrO_2 shares an important role in the turbine

components as the thermal barrier coating material for turbine blades and vanes. However, its fracture toughness and strength are deteriorated at high temperatures, due to the temperature dependence of the martensitic transformation energy and by the ionic bonding of the constituent atoms. In addition, the specific density of ZrO_2 is considerably high. On the other hand, Si_3N_4 retains high strength and resistance against creep and wear at high temperatures. **Fig. 1.1** depicts the temperature dependence of the bend-fracture strength of Si_3N_4, in comparison with SiC and ZrO_2 [1.31, 1.32]. The strength of ZrO_2 is significantly deteriorated by increasing the temperature, while that of Si_3N_4 and SiC are retained at high temperatures. Si_3N_4 and SiC are both covalent materials. The excellence of Si_3N_4 is also placed on the low thermal expansion property, high thermal-shock resistivity, high fracture toughness and low specific density. These properties of Si_3N_4 make it suitable for high-temperature structural applications with the highest total-performance among the fine-ceramics.

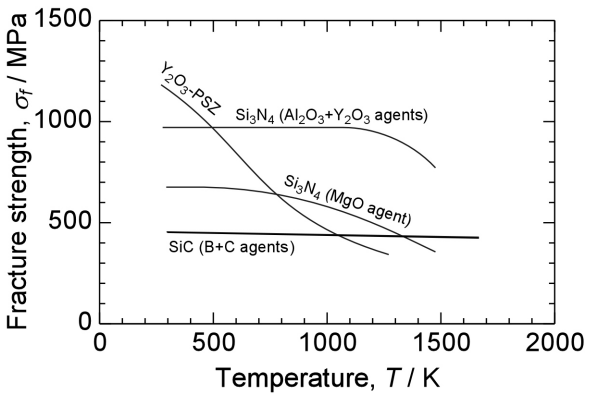

Fig. 1.1 Temperature dependence of the bend-fracture strength of Si_3N_4, SiC and ZrO_2 [1.31, 1.32].

B. Silicon Nitride – Fabrication Process and Character

Fig. 1.1 also indicates that the strength of Si_3N_4 varies by changing the sintering agents. Since Si_3N_4 cannot be mined from the nature, bulk bodies of Si_3N_4 is produced from powders by sintering. The powders of Si_3N_4 is fabricated by nitriding of silicon powders, by reduction-nitriding reaction of silica using carbon in nitrogen atmosphere, and by vapor reaction of SiH_4 and NH_3 [1.33]. The sintering of the high-purity powders of Si_3N_4 is difficult, because its strong covalent connection of atoms restricts their internal diffusion and the elimination of pores. Since the pores behave as the origin of the fracture of sintered bodies, the elimination of them is the most important point in the sintering process. Therefore, sintering agents are commonly added to enhance the elimination of pores. The sintering agents occupy the interparticle boundaries and pockets. Thus, the properties of sintered Si_3N_4 is sensitively

affected by the composition of the agents. MgO, Y_2O_3 and Al_2O_3 are usually used as the sintering agents for Si_3N_4. The exact composition-ratio of them and extra agents is, however, a proprietary of the manufacturers.

Four methods are applicable for sintering Si_3N_4: reaction sintering (RS), hot pressing (HP), hot isostatic pressing (HIP) and pressureless sintering (PLS) [1.31, 1.34]. The RS produces low-density bodies with low performance. However, only slight overall volume change occurs during the fabrication process, so that complex or accurately dimensioned shapes can be produced in a single stage from a shaped compact of silicon powder. The HP and HIP yield high-density products with less amount of sintering agents. Although the properties of the products are excellent, the HP and HIP can produce only small-sized bodies with simple geometry. The PLS is the most suitable method for mass production of structural components. It can produce complex or large-sized bodies of Si_3N_4 with favorable density. However, PLS requires high sintering temperature. As shown in Table 1.1, Si_3N_4 decomposes at 2173 K in ambient atmosphere. The dependence of the decomposition condition on the temperature and the partial pressure of nitrogen is depicted on **Fig. 1.2** [1.35]. The higher sintering temperature requires the higher partial pressure of nitrogen to avoid the decomposition. Although the decomposition rate of Si_3N_4 is very slow, the sintering is implemented in high pressure of pure nitrogen to protect the thin skin of Si_3N_4 powders from decomposition and resultant oxidation of silicon.

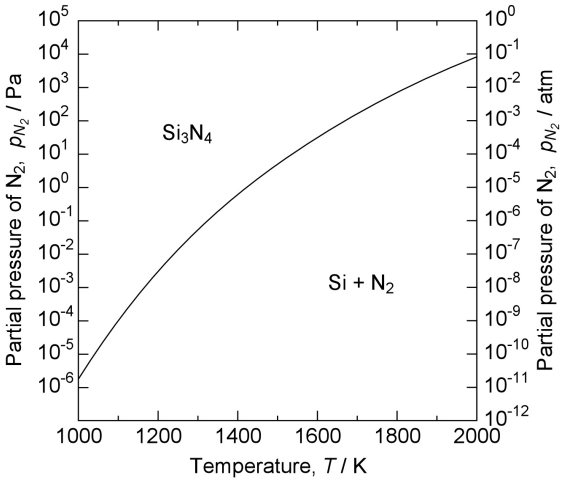

Fig. 1.2 Decomposition condition of Si_3N_4 as a function of temperature and partial pressure of nitrogen [1.35].

Si_3N_4 has two polytype structures: α and β. The crystallographic data of each structure is shown in **Table 1.3** [1.33, 1.36-1.38]. In both structures, each silicon atom is connected tetrahedrally to four nitrogen atoms and each nitrogen atom on the apex of the tetrahedron is connected to three silicon atoms in approximately trigonal planar arrangement to form a three-dimensional frame structure. The unit cell of α-Si_3N_4 has the approximate structure in which a unit cell of β-Si_3N_4 and its *0 0 0 1* mirror-symmetrical cell are alternatively stacked to the ***c***

Table 1.3 Crystallographic data for α- and β-Si_3N_4 [1.33, 1.36-1.38].

Crystallographic parameters	α-Si_3N_4	β-Si_3N_4
Bravais lattice	Trigonal (Rhombohedral)	Hexagonal
Space group	P31c (159)	$P6_3$ (173)
Pearson symbol	hP28	hP14
Lattice constant ***a*** / nm	0.77541	0.75950
c / nm	0.56217	0.29023
Atom positions: (element, Wyckoff notation: *x*, *y*, *z*)	N, 2a : 0.0000, 0.0000, 0.4503 N, 2b : 0.3333, 0.6667, 0.5926 N, 6c : 0.6558, 0.6075, 0.4320 N, 6c : 0.3154, 0.3192, 0.6962 Si, 6c : 0.0829, 0.5135, 0.6558 Si, 6c : 0.2555, 0.1682, 0.4509	N, 2b : 0.3333, 0.6667, 0.2392 N, 6c : 0.0298, 0.3294, 0.2628 Si, 6c : 0.7686, 0.1744, 0.2500

axis, revealing similar lattice parameter of ***a*** and approximately twice that of ***c***.

α-Si_3N_4 powder is used for sintering purpose. During sintering, α-Si_3N_4 transforms at 1673 K irreversibly to β-Si_3N_4 and grows to its [*0 0 0 1*] direction to form acicular grains. Sintered body of β-Si_3N_4 with developed acicular grains has better performance.

C. Problems in Practical Application of Silicon Nitride to Structural Components

Si_3N_4 is a material in which atoms are strongly covalent-bonded. The nature of atomic connection in the material retains high strength and resistivity against wear and corrosion and performs high thermal shock resistivity, being suitable for the structural components operated at elevated temperatures in the next generation. However, these properties of Si_3N_4 make it difficult for the practical application of the material, on the other hand. The following three points are recognized as the most severe problems:

(i) The covalent connection of the constituent atoms disallows the plastic deformation of the material, *i.e.*, Si_3N_4 is congenitally brittle.

(ii) The hardness of Si_3N_4 makes the machining to a precise shape difficult.

(iii) The large thermal expansion mismatch and the low affinity with metallic materials make the bonding of Si_3N_4 with metals difficult.

The first problem can be comforted by controlling the composition of the sintering agents. However, it will be impossible to compensate the brittleness without deterioration of the beneficial properties of Si_3N_4. Therefore, Si_3N_4 should be used in combination with ductile

metallic components. The second problem seems to have been overcome by the recent progress in near-net shape sintering and development of the laser machining technology. However, the cost to obtain precisely shaped products is still high. This fact also leads to an answer that Si_3N_4 should be used in combination with metallic components. To use Si_3N_4 in combination with metals requires to form joints of them. However, the third problem has to be overcome to produce reliable joints with sufficient performance to exhibit the beneficial properties of Si_3N_4.

III. History of Technology of Ceramics Bonding

A. The Incunabulum of the Bonding Technology of Ceramics

The joining of ceramics to metals came of age as an industrial process in the late 1930's, during World War II, in Germany [1.39]. The first ceramic / metal joints were produced by brazing a metallized ceramic to a metal member with a silver-base filler metal. Metallizing is a surface preparation process of ceramics to promote wetting by and flow of the brazing filler metals. The earliest metallizing of ceramic surfaces was done by sintering mixed pure-metal powders on the ceramics. In 1950, a procedure to metallize ceramic surfaces with powders of molybdenum containing 10 to 20% manganese was developed by H.J. Nolte and R. Spurck. The technique is known as the moly-manganese process. This technique was widely accepted by industry as a standard method to metallize ceramic surfaces [1.39, 1.40].

The procedure to bond ceramics with metals in this age was rather complicated. The ceramic surfaces required the following processes prior to the brazing operation; (i) cleaning with several steps of chemical treatments, (ii) metallizing process, (iii) electroplating of nickel to retard penetration of the filler into the metallize layer and copper to provide good wetting with the filler. Therefore, the fabrication process of ceramic / metal joints was costly and time-consuming. To simplify the pre-bonding processes, to paint titanium hydride powders on the unmetallized ceramic surfaces to wet directly with filler alloys was put forward by R. Bondley in 1947. His work was extended by C.S. Pearson and P.K. Zingeser, who found that powders of active metals (*e.g.*, titanium and zirconium) are effective for direct wetting of unmetallized ceramic surfaces. The technique developed by them is known as the active metal bonding process [1.39].

Although the oxide-ceramics such as Al_2O_3, BeO and MgO are all but those dealt with in this age, the essential part of the recent technique to braze ceramic materials with metals has already been established, and the problems which are common to the recent technology such as the residual stress originated from the thermal expansion mismatch and the brittle phase formation by the interfacial reaction have been recognized [1.39]. Unfortunately, since the quality of the ceramic materials in this age is poor and scattering, the actual processing parameters deduced by the researchers in this age cannot be directly applied to the recent fine-ceramic materials. In addition, the investigation on the interfacial microstructure, the reaction kinetics and the chemical state of constituent atoms were completely missing.

B. Progress in Science and Technology of Ceramics Bonding in the Last Two Decades

In the last two decades, the science and technology concerning the bonding of ceramics have innovatively progressed. The development of the new techniques for local-area analysis of the joint interfaces (*e.g.*, high-resolution transmission electron microscopy, electron probe microanalysis and X-ray photoelectron spectroscopy) has provided a way to know the local structure of the joint interface in atomic scale, the local composition profile which shows the diffusion and reaction behavior of the constituent elements during bonding, and the electronic structure which shows the chemical state of atomic bonds at the ceramic / metal interface. The improvement in calculation-speed of computers has made it possible to approach the ceramics bonding from the theoretical point of view, *e.g.*, first-principle electronic structure simulation of the ceramic / metal interface and the finite-element simulation of the stress distribution and fracture. Moreover, the quality of the fine-ceramic materials has come into a sufficient level of homogeneity, which allows to analyze and to evaluate the properties of them and their joints statistically and systematically. Based on these circumstances on the background, bonding of a wide range of fine-ceramic materials (oxides, nitrides, carbides and borides) with metallic materials has been studied by numerous researchers [1.41]. The recent studies concerning the bonding of fine-ceramics with metallic materials can be categorized into the following three fields: (1) development and application of a new technique for the ceramic / metal bonding, (2) evaluation and prediction of mechanical and other properties of the joints and (3) metallurgical analysis and control of the interfacial microstructures. The fundamental

Table 1.4 A list of bonding techniques for ceramics / metals bonding.

Category	Bonding technique	Features
mechanical connection	shrink fitting	requires precise shaping of the components.
	enveloped casting	costly.
	riveting / stapling	independent on ceramic / metal combination.
	bolting / screw fastening	independent on ceramic / metal combination.
adhesive bonding	organic adhesives (epoxy, acrylic adhesive, *etc.*)	restricted operation temperature, low cost.
	inorganic adhesives (SiO_2 based, Al_2O_3 based, *etc.*)	fire resistant, brittle.
chemical bonding	metallizing + brazing	high reliability, costly.
	active metal brazing	high reliability, suitable for mass production.
	partial transient liquid phase bonding	high reliability, favorable strength at high temperatures.
	solid state diffusion bonding	requires high temperature and pressure, retains high strength at high temperatures.
	friction bonding / ultrasonic bonding	high strength
	surface activation bonding	requires ultra-high vacuum.

achievements and current issues in each category are reviewed in the following.

(1) *Techniques to Bond Ceramics with Metals*

The recent bonding techniques can be categorized into the following three groups: mechanical connection, adhesive bonding and chemical bonding. **Table 1.4** shows a list of techniques to bond ceramics with metals.

Shrink fitting and enveloped casting utilize the thermal expansion mismatch between ceramics and metals. Although shrink fitting requires precise shape preparation of the components, it has proved its applicability to ceramic / metal bonding in combination with active metal brazing by adopting to the bonding of automotive turbo-charger rotor made of Si_3N_4 with steel shaft [1.22, 1.42]. Riveting, stapling, bolting and screw-fastening can connect ceramics and metals independent on the combination of the materials. In addition, they can be implemented without heating of the materials nor controlling of the atmosphere. However, their joint efficiency is relatively low.

Adhesive bonding is one of the simplest method to bond ceramics with metals, and to enhance the strength of the riveted or bolted joints [1.43, 1.44]. It has been applied to bond ceramic tiles to the bottom surface of the space-shuttles. However, the adhesive-bonded joints cannot be used in high temperatures or for long duration.

Chemical bonding utilizes diffusion, reaction or solution phenomena of the constituent atoms at the interface to bond ceramics with metals. To fabricate high strength, air tight and reliable ceramic / metal joints, chemical bonding has been considered to be the most suitable method and extensive research and development has been conducted on the method. The moly-manganese metallizing + brazing has been a well-established and reliable technique for bonding oxide ceramics. For non-oxide ceramics, the bonding techniques has been developed on the basis of the active metal bonding. Active metal bonding utilizes the good affinity and wettability of ceramic surfaces with the metallic elements in the III, IV and V families of the periodic table.

Active metal brazing is one of the active metal bonding methods. Since molten braze metal is spread on the ceramic surfaces during bonding, the technique can be applied to complex bond-faces. In addition, active metal brazing can fabricate ceramic / metal joints with high reliability in a way suitable for mass production. A number of active metal brazing alloys, centering to silver-copper eutectic braze containing approximately 2 mass% titanium, has been applied to ceramic / metal bonding [1.45-1.66]. However, the strength of the brazed joints at elevated temperatures is deteriorated because of the low solidus temperature of the brazing alloys. The operation of the joints is restricted to the temperature below 873 K [1.64].

In order to improve the high-temperature strength of the brazed joints, partial transient liquid-phase brazing has been developed [1.58, 1.67-1.69]. This technique utilizes a multi-layered brazing sheet, which melts partially in the vicinity of the bonding interface and then solidifies isothermally. The local composition change of the brazing sheet by the interlayer diffusion induces this unique melting-solidification sequence. Since the joint interface fabricated with this technique has no longer the brazing material with low solidus temperature, high-temperature strength of the joints can be improved with this technique.

Solid state diffusion bonding is an another active metal bonding technique to fabricate joints with high strength at high temperatures. Refractory metals or alloys are bonded with ceramics at lower temperatures than their melting points, directly or by being used as the filler insert. Generally, such refractory metals have low thermal expansion coefficients and possibility to reduce the magnitude of the thermal residual stress when they are bonded with ceramics. Since no melt is formed at the interface during bonding, a sufficient pressure to

achieve close-fitting between the bonding surfaces of ceramics and metals is necessary for this technique. Attributed to the potential to fabricate ceramic / metal joints with high strength at high temperatures, solid state diffusion bonding has been investigated extensively [1.41, 1.58, 1.70-1.88].

Active metal bonding requires an amount of energy to enhance wetting, adsorption or reaction at the ceramic / metal interface. Generally, the energy is supplied to the interface by heating the bonding components in an atmosphere-controlled furnace. Besides heating in the furnace, numerous energy-supplying methods has been investigated. Friction bonding [1.65, 1.89, 1.90] and ultrasonic bonding [1.91] supply mechanical energy to the interface. Spark plasma bonding [1.92], direct and alternating conduction bonding [1.93, 1.94] utilize electric energy to form a joint.

Surface activation bonding [1.41, 1.95-1.99] is a unique technique which stands on the philosophy that the surface of materials, regardless of ceramics or metals, is adhesive when the constituent atoms on the surface are not contaminated, terminated nor reconstructed. The contaminating and terminating atoms on the surface are removed by irradiation of accelerated ions or atoms of inert gas in ultra-high vacuum. Then, the cleaned surfaces are put together and pressed to fit the surfaces in atomic scale. Bond is achieved without heating. Therefore, surface activation bonding is considered to be one of the active metal bonding in which the energy for bonding is supplied to the interface by energetic atom bombardment. Although this technique is not suitable for mass production, its feature to fabricate joints without any reaction product and thermal residual stress has made the technique be a powerful method for fundamental researches on ceramics / metal bonding.

The recent issues of active metal bonding of ceramics with metals can be summarized to the thermal residual stress and the brittle phase formation. The research achievements and current issues of them are reviewed in the following sections.

(2) *Evaluation and Prediction of Mechanical Properties of Ceramic / Metal Joints*

The thermal residual stress is originated from the thermal shrinkage mismatch between ceramic and metal during cooling down from the bonding temperature to the ambient temperature. In addition, the stress is intensified by the high elastic modulus of the ceramics

Table 1.5 Methods to relieve the thermal residual stress at the ceramic / metal interfaces.

Strategy	Methods
To decrease the thermal expansion mismatch	- insertion of single or multiple interlayers of materials with intermediate thermal expansion characteristics. - insertion of functionally gradient interlayers.
To decrease the difference between the bonding and room temperature	- low temperature brazing. - surface activation bonding.
To absorb the interfacial elastic energy	- insertion of soft metals.

and changes depending on the size and shape of the bond area. Some methods to relieve the stress have been proposed and listed in **Table 1.5**. The utilization of soft (low-yield-stress) interlayers can relax the stress by the plastic deformation of the layer [1.70, 1.76, 1.100-1.104]. However, the strength of the joints is inevitably deteriorated at high temperatures, due to the existence of the soft layer at the interface. Also the utilization of low-temperature brazing alloys can suppress the stress generation, though it is not suitable for the joints used in high temperatures. The utilization of functionally gradient interlayers, which changes its thermal expansion coefficient within the range between those of ceramics and metals continuously or stepwise, is an another method to relieve the stress [1.105]. Although this method requires rather thick interlayer, it is suitable for ceramic / metal joints used in high-temperatures.

Ishida *et al.* [1.106-1.108] have investigated the relaxation mechanism of thermal stress in atomic scale, and proposed a strategy to design structural defects such as misfit dislocations and ledges at the ceramic / metal interfaces to take advantages of the stress relaxation by the migration of the defects. Although this strategy gives the fundamental knowledge on relieving the thermal residual stress, it can be adopted only to the joints free of reaction phases. Moreover, to control the orientation of crystals at the interfaces implies the restriction of its applicability only to the joints of single crystals, which are rarely used in actual applications.

The local magnitude of the thermal residual stress in the vicinity of the ceramic / metal joint interfaces has been investigated both experimentally and theoretically. The experimental approach has been carried out by the X-ray diffraction method [1.109, 1.110], the indentation-fracture method [1.111], the ultrasonic microscopy [1.112] and the strain-gauge method [1.71]. Tanaka and Takahashi have shown the effect of the X-ray collimation on the measured

residual stress, being larger with smaller irradiation area [1.109]. This result indicates that the residual stress is concentrated in a very narrow region of the vicinity of the interface and that sufficient spatial resolution is required to obtain the real magnitude of the residual stress. However, the distribution of the thermal residual stress measured by these methods show the same tendency [1.113], indicating that the most harmful tensile stress appears at the ceramic side of the vicinity of the interface to the direction perpendicular to the interface. On the other hand, the theoretical approach is mainly implemented by the finite- and boundary-element calculations [1.101, 1.111, 1.113-1.117]. The results of these calculations have shown a good agreement with those of experimental measurements. In addition, the calculations have been adopted to joints with complex geometry [1.42], and have proposed the optimum thickness of the soft metal interlayers [1.117].

To evaluate the strength, standards for bend (three or four point-loading) [1.118] and tensile [1.119, 1.120] testing have been established. However, most of researchers have used their own method for evaluation: bend [1.121], tensile [1.70] and shear [1.122] test are the most commonly used methods [1.100]. Bend test and tensile test can perform almost ideal stress distributions as those derived from analytical equations. However, bend test and tensile test require respectively a long specimen and a precise setting of the specimen to the loading axis to obtain the reproducible strength value with less scatter. Generally, the tensile strength appears lower than the bend strength [1.100]. On the other hand, shear test is one of the simplest evaluation methods. However, the stress applied to the specimen by the test cannot be a pure shear, *i.e.*, it always contains tensile stress component originated from the bending moment. In addition, the stress distribution is severely affected by the slight shift of the load position. Therefore, the method is not recommended for accurate evaluation purpose. Although the method has these disadvantages, it is frequently used due to its simplicity and the applicability to the test of small and short specimens.

The studies on the strength evaluation and prediction has not taken into account the actual active metal bonded interfacial microstructures with brittle reaction products or flaws in the vicinity of the interfaces so far. Since the experimental measurement of the thermal residual stress is difficult to increase the spatial resolution higher than 0.1 mm of diameter, to take the advantages of finite-element simulation becomes quite important to predict the

strength performance of the joints. However, the lack of the non-destructive flaw inspection techniques for ceramic / metal joints and the information about the interfacial microstructures and the mechanical properties of the reaction products are making to build a correspondent calculation model difficult.

(3) *Analysis and Control of Ceramic / Metal Interfaces*

The metallurgical phenomena occurring at the ceramic / metal interfaces during active metal bonding, such as wetting, diffusion, reaction and adhesion, and the resultant interfacial microstructure has been also studied from both experimental and theoretical approaches. Taking advantages of the new analyzing techniques, these interfacial phenomena and the nature of the constituent and impurity atoms, which have been missing in the earliest age, are gradually coming into the knowledge.

Wetting is the critical property for braze metals. Recent investigations of the wetting phenomena has proven that even the active braze metals generally do not wet the ceramic surfaces directly, but metallize the surfaces by the reaction between the active elements with ceramics [1.52, 1.60, 1.61, 1.123]. The wetting proceeds on the metallized surfaces. Therefore, the contact angle measured by sessile drop method do not correspond to that of the ceramics and the braze metals, but to that of the metallizing reaction product and the braze metals. Nogi *et al.* have demonstrated the effect of the chemical potential at the interface on the wettability of ceramics by commonly non-reactive molten metals [1.93].

Diffusion, reaction and the resultant interfacial microstructure of the joints have been actively studied, because to control them precisely is necessary for fabrication of the joints with their highest performance. Two representative methods have been used for the study on the diffusion and reaction behavior between ceramics and metals: the powder method [1.124-1.141] and the diffusion couple method [1.142-1.148]. The powder method is a simple but accurate method to investigate the reaction. The compacted specimens of the mixed powder of ceramics and metals are suitable for thermal analysis and X-ray diffraction measurement. By this method, the onset temperature of each partial reaction process and the crystallographic information of the phases existing in the equilibrium state of the system can be accurately obtained. However, the reaction rate becomes considerably high and changes depending on

the grain size of the powders, which determine the specific surface area in the specimens. Therefore, the knowledge of the interfacial transition phenomena such as the phase sequence is difficult to obtain with this method. In addition, to conserve the stoichiometry in the ceramic / metal system is difficult when a reaction producing gas phases takes place, which might cause a different reaction behavior from that occurs at the actual bonding interface. On the other hand, the diffusion couple method reveals the diffusion and reaction behaviors and the resultant interfacial microstructures which occur at the actual bonding interfaces. The morphology of the reaction products including the phase sequence and the growth kinetics of them can be accurately obtained. The results obtained with both methods has been discussed on the basis of metallurgical thermodynamics and diffusion and reaction theories.

Although the interfacial diffusion, reaction and microstructures of a number of ceramic / metal systems has been reported, the reports by different researchers appear sometimes quite different from each other. It is natural to be different when the bonding techniques and conditions are different. However, the problem is placed on that no theory, which successfully explains the difference and unifies the knowledge of the interfacial phenomena, has been established.

The advanced techniques for materials analysis made an another research activity possible. It is to investigate the atomic and electronic state of ceramic / metal bonds. Since the atomic cohesion of ceramics (covalent or ionic) are rather different from that of metals (metallic), the transition in physical state of valence electrons [1.149, 1.50] and the lattice arrangement and structure of misfit dislocations including its glide / climb motion [1.106-1.108, 1.51-1.57] have come into interest. For these purposes, a ceramic / metal interface free of reaction products and residual stresses (*e.g.*, Al_2O_3 / Nb joint) have been intensively investigated. The theoretical approach to these issues have been conducted on the basis of the first-principle *ab-initio* simulation [1.158-1.161] and molecular-dynamic simulation [1.162-1.164]. Unfortunately, the researches on the issues are still under development. The recent achievements cannot be directly adopted to the actual active metal bonded ceramic / metal interfaces in which reaction products and thermal residual stresses are formed.

IV. Purpose and Flow of the Present Research

At the active metal bonded ceramic / metal interfaces, reaction takes place. The reaction products such as intermetallic compounds or silicides are generally brittle, and can cause the deterioration in joint strength. However, to achieve a strong chemical bond between ceramics and metals without formation of brittle reaction phases is a contradictory propositions, which is very difficult to overcome simultaneously. To suppress the effects of the brittle reaction phases on the joint strength by precise control of the interfacial reaction and the resultant microstructure is an acceptable solution for the issue. Therefore, to develop a technology to control the interfacial microstructure is required. The technology should be established on the basis of metallurgical thermodynamics and diffusion and reaction theories.

The present research deals with the solid state diffusion bonding of Si_3N_4 using active filler metals of titanium, vanadium and niobium, with the following two purposes: (1) to clarify the interfacial microstructure and the reaction behavior at the Si_3N_4 / metal interface, and (2) to propose some methods to control the interfacial reaction and the resultant microstructure on the basis of metallurgical thermodynamics and diffusion and reaction theories. As described in the section II, Si_3N_4 is the candidate material for the next generation turbine generators. To realize the application, the bonding technology has to be established. The former purpose corresponds to obtain the basic knowledge of the interfacial phenomena in detail of each Si_3N_4 / metal system. The knowledge will allow researchers and engineers to conduct an accurate thermal residual analysis and life assessment of the joints, which is essential for practical structure design. Based on the obtained knowledge, some methods to control the interfacial microstructure are proposed, being the latter purpose.

The solid state diffusion bonding was selected due to the following two points: (1) its applicability to the bonding of ceramics and metals which joints are used at high temperatures, and (2) the simplicity of the interfacial phenomena compared to brazing (*e.g.*, the effect of convection on the interfacial reactions can be neglected).

Table 1.6 shows some properties of titanium, vanadium and niobium [1.165-1.170]. These metallic elements have high melting temperatures, low thermal expansion coefficients and sufficient reactivity with silicon nitride. These properties are beneficial to fabrication of high temperature ceramic / metal joint-structures.

Table 1.6 Properties of titanium, vanadium and niobium [1.165-1.170].

Properties	Active metallic elements		
	titanium (Ti)	vanadium (V)	niobium (Nb)
Family on the periodic table	IV B	V B	V B
Density, ρ_V / kg m^{-3}	4.508×10^3 (298 K) 4.400×10^3 (1173 K)	6.09×10^3 (303 K)	8.578×10^3 (293 K)
Transition temperature, T_T / K	1156 ± 2 ($\alpha \leftrightarrow \beta$)	–	–
Melting temperature, T_M / K	1953 ± 4	2108 ± 10	2793 ± 10
Boiling Temperature, T_B / K	3535	(3673)	5200
Thermal conductivity, μ / W m^{-1}K^{-1}	21.9 (300 K)	30.7 (300 K)	53.7 (300 K)
Linear thermal expansion coefficient, α / K^{-1}	8.9×10^{-6}	8.3×10^{-6}	7.2×10^{-6}
Elastic modulus, E / GPa	114.2 (298 K)	132.6 (298 K)	104.6 ± 0.2 (293 K)
Shear modulus, G / GPa	(39.8)	(46.6)	37.3 (293 K)
Crystal structure	αTi: Hexagonal, $P6_3/mmc$ (194) a = 2.9505 Å c = 4.6826 Å (298 K) βTi: Cubic, Im3m (229) a = 3.3065 Å (1173 K)	Cubic, Im3m (229) a = 3.0274 Å (293 K)	Cubic, Im3m (229) a = 3.3066 Å (293 K)

This thesis consists of eight chapters. **Fig. 1.3** shows the flow and the relation of each chapter. In Chapter 1, the motivation, the nature of Si_3N_4 and other ceramic materials, the historical review on the bonding technology of ceramics to metals and the purpose of the present study are described. In Chapter 2, the theories lying on the background of the present study are briefly described. In Chapter 3, the materials and the facilities used in the present study and the experimental conditions are described. In Chapters 4, 5 and 6, the interfacial microstructures and their evolution kinetics of the solid state diffusion bonded Si_3N_4 and titanium, vanadium and niobium, respectively, are described in detail. In these chapters, the results of the interfacial control are also presented. In Chapter 7, the general discussion on the methods to control the interfacial microstructure is conducted. In Chapter 8, the conclusion of the present study is described.

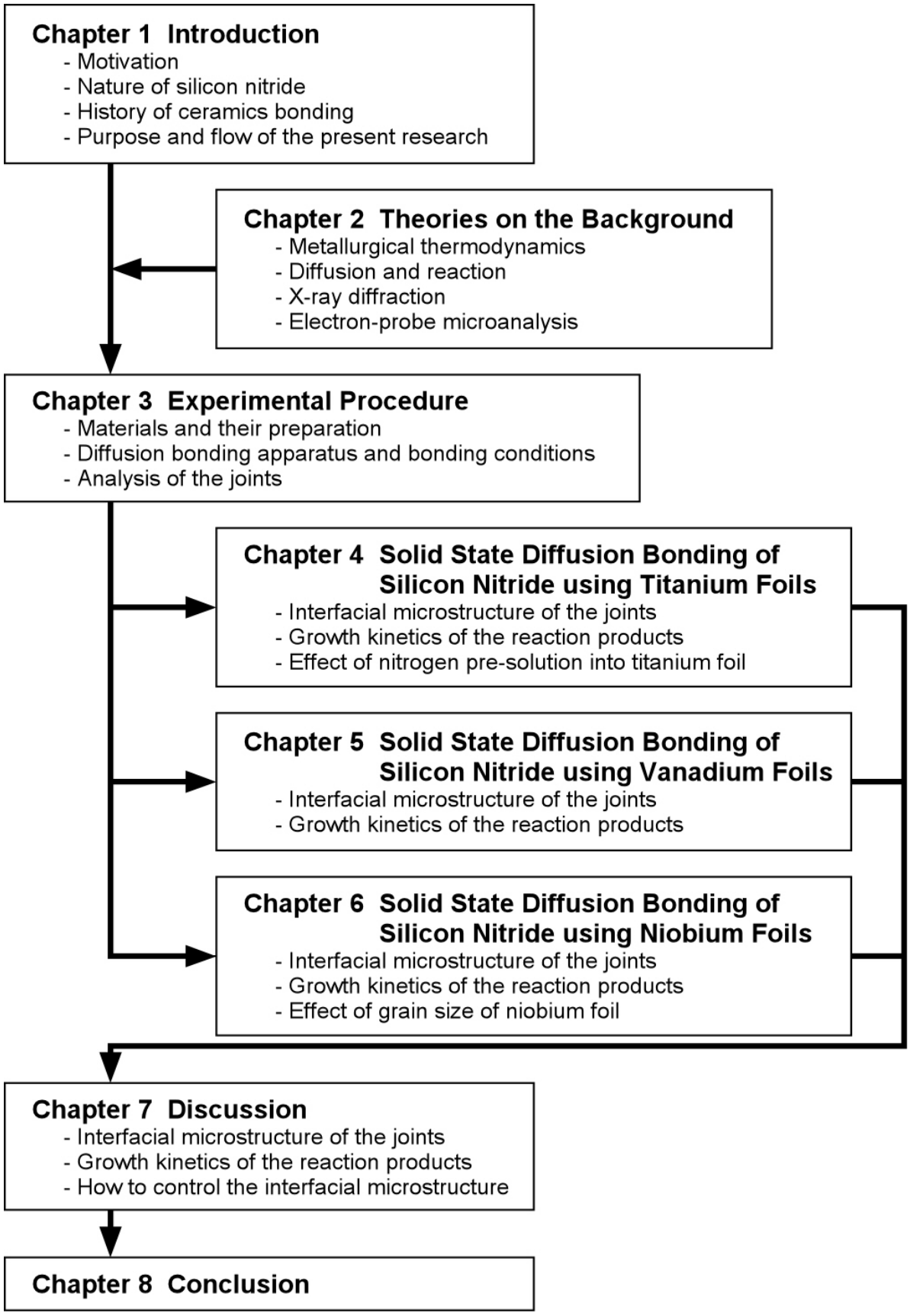

Fig. 1.3 Flow chart of the present thesis.

References

[1.1] *UNEP Annual Report*, United Nations Environment Programme, 2002.

[1.2] United Nations Environment Programme website. http://www.unep.org/ or http://www.grida.no/db/maps/collection/climate6/index.htm

[1.3] *Children in the new millennium: environmental impact on health*, United Nations Environment Programme, United Nations Children's Fund and World Health Organization, UNEP, Nairobi (Kenya), 2002.

[1.4] B. Menne and R. Bertollini: *Down to Earth: The Newsletter of the Convention to Combat Desertification*, December 2000, No. 14, pp. 4-7.

[1.5] J. Kemm: *Bulletin of the World Health Organization*, 2003, Vol. 81, No. 6, pp. 387.

[1.6] *Supply-and-Demand of Energy in the 2001 fiscal year (authentic report)*, Agency for Natural Resources and Energy of Japan, May 21, 2003, in Japanese.

[1.7] *Balance Sheet of Energy in the 2001 fiscal year*, Agency for Natural Resources and Energy of Japan website, in Japanese. http://www.enecho.meti.go.jp/info/statistics/index4.htm

[1.8] K. Yamaguchi: *J. High Temp. Soc. Jpn.*, 1997, Vol. 23, pp. 203-208, in Japanese.

[1.9] U. Schulz, C. Leyens, K. Fritscher, M. Peters, B.B. Saruhan, O. Lavigne, J.-M. Dorvaux, R. Mevrel and M. Caliez: *Aerospace Sci. Technol.*, 2003, Vol. 7, pp. 73-80.

[1.10] N.A. Kumar and S.R. Kale: *Int. J. Heat and Mass Transfer*, 2002, Vol. 45, pp. 4831-4845.

[1.11] M. Konter and M. Thumann: *J. Mater. Process. Technol.*, 2001, Vol. 117, pp. 386-390.

[1.12] A.K. Ray, and R.W. Steinbrech: *J. Europ. Ceram. Soc.*, 1999, Vol. 19, pp. 2097-2109.

[1.13] T. Troczynski, S. Cockcroft and H. Wong: *Key Eng. Mater.*, 1996, Vol. 122-124, pp. 451-462.

[1.14] A.S. Osyka, A.I. Rybnikov, S.A. Leontiev, N.V. Nikitin and I.S. Malashenko: *Surface Coat. Technol.*, 1995, Vol. 76, pp. 86-94.

[1.15] C.M. Grondahl and T. Tsuchiya: *Trans. ASME, J. Eng. Gas Turbines and Power*, 2001, Vol. 123, pp. 513-519.

[1.16] M. Yoshida, K. Tanaka, S. Tsuruzono and T. Tatsumi: *Industrial Ceramics*, 1999, Vol. 19, pp. 188-192.

[1.17] K. Nakakado, T. Machida, H. Miyata, T. Hisamatsu, N. Mori and I. Yuri: *Trans. ASME, J. Eng. Gas Turbines and Power*, 1995, Vol. 117, pp. 245-250.

[1.18] T.B. Gibbons: *Z. Metallkd.*, 1992, Vol. 83, pp. 409-415.

[1.19] T. Hisamatsu, T. Abe, T. Mimaki, H. Miyata, T. Machida and R. Ooshima: *Trans. Jpn. Soc. Mech. Eng., Part B*, 1991, Vol. 57, pp. 819-824, in Japanese.

[1.20] T. Derkacs, I.M. Matay and W.D. Brentnall: *Trans. ASME, J. Eng. Power*, 1978, Vol. 100, pp. 549-552.

[1.21] A.F. McLean: *Engineer*, 1970, Vol. 231, pp. 29-31.

[1.22] *Functions and Applications of Advanced Ceramics*, S. Somiya (Editor-in-chief), Gihodo Publ., Tokyo (Japan), 2002, pp. 204-207, in Japanese.

[1.23] M.R. Effinger, G.G. Genge and J.D. Kiser: *Adv. Mater. Process.*, 2000, Vol. 157, pp. 69-73.

[1.24] T. Tetsui: *J. Jpn. Inst. Met.*, 2000, vol. 64, pp. 971-976.

[1.25] K. Funatani, K. Kurosawa, P.A. Fabiyi and M.F. Puz: *Automotive Eng.*, 1995, Vol. 103, pp. 15-20.

[1.26] M. Wilhelm: *J. Phys.*, 1993, Vol. 3, pp. 31-40.

[1.27] D.C. Larsen, J.W. Adams, L.R. Johnson, A.P.S. Teotia and L.G. Hill: *Ceramic Materials for Advanced Heat Engines: Technical and Economic Evaluation*, William Andrew Publ., New York (USA), 1985.

[1.28] *CRC Materials Science and Engineering Handbook*, 2nd Edition, James F. Shackelford, William Alexander and Jun S. Park (Eds.), CRC Press, Boca Raton, Florida (USA), 1994.

[1.29] H. Yanagida: *Fine Ceramics*, Blue Backs B-517, Kodansha, Tokyo (Japan), 1990, in Japanese.

[1.30] *Specification of Ceramic Materials*, Product Catalogue of KYOCERA Corp., 2001, in Japanese.

[1.31] T. Ishino: in *Basis of Solid State Chemistry and Inorganic Materials*, G. Adachi (editor-in-chief), Maruzen, Tokyo (Japan), 1995, pp. 239-241, in Japanese.

[1.32] M. Sakamoto: *10th Powder Seminar Text*, Japan Society of Powder and Powder Metallurgy, 1986, pp. 30, in Japanese.

[1.33] F.S. Galasso: Structure and Properties of Inorganic Solids, International Series of Monographs in Solid State Physics, Vol. 7, Pergamon Press, Oxford (UK), 1970, Translated by M. Kato and K. Uematsu, 2nd edition, Agne Technology Center, Tokyo (Japan), 1987, pp. 307-312, in Japanese.

[1.34] F. L. Riley: in *Encyclopedia of Materials Science and Engineering*, M. B. Bever (Editor-in-Chief), Pergamon Press, New York (USA), 1986, Vol. 6, pp. 4412-4415.

[1.35] W.B. Hincke and L.R. Brantley: *J. Amer. Chem. Soc.*, 1930, Vol. 52, pp. 48-52.

[1.36] P. Villars and L.D. Calvert: Pearson's Handbook of Crystallographic Data for Intermetallic Phases, American Society for Metals, Metals Park, Ohio (USA), 1985, Vol. 3, pp. 2789-2790.

[1.37] *Powder Diffraction Files*, JCPDS–International Centre for Diffraction Data, Newtown Square, Pennsylvania (USA), 41-360.

[1.38] *Powder Diffraction Files*, JCPDS–International Centre for Diffraction Data, Newtown Square, Pennsylvania (USA), 33-1160.

[1.39] H.E. Pattee: *Weld. Res. Council Bull.*, 1972, Vol. 178, pp. 1-43.

[1.40] G.M. Slaughter: *Weld. J.*, 1979, Vol. 58, No. 10, pp. 17-28.

[1.41] G. Elssner and G. Petzow: *ISIJ Int.*, 1990, Vol. 30, pp. 1011-1032.

[1.42] K. Kato: *Bull. Ceram. Soc. Jpn.*, 1995, Vol. 30, pp. 94-96, in Japanese.

[1.43] H. Nakayama and M. Imanaka: *Bull. Ceram. Soc. Jpn.*, 1995, Vol. 30, pp. 97-101, in Japanese.

[1.44] L. Esposito, A. Bellosi and S. Landi: *J. Amer. Ceram. Soc.*, 1999, Vol. 82, pp.3597-3604.

[1.45] K. Suganuma, T. Okamoto, M. Koizumi and M. Shimada: *J. Mater. Sci.*, 1987, Vol. 22, pp. 1359-1364.

[1.46] M. Morita, K. Suganuma and T. Okamoto: *J. Mater. Sci. Lett.*, 1987, Vol. 6, pp. 474-476.

[1.47] X.S. Ning, T. Okamoto, Y. Miyamoto, A. Koreeda and K. Suganuma: *J. Mater. Sci.*, 1989, Vol. 24, pp. 2865-2870.

[1.48] X.S. Ning, K. Suganuma, T. Okamoto, A. Koreeda and Y. Miyamoto: *J. Mater. Sci.*, 1989, Vol. 24, pp. 2879-2883.

[1.49] Y. Nakao, K. Nishimoto and K. Saida: *Trans. Jpn. Weld. Soc.*, 1989, Vol. 20, pp. 66-76.

[1.50] Y. Nakao, K. Nishimoto and K. Saida: *Trans. Jpn. Weld. Soc.*, 1990, Vol. 21, pp. 135-143.

[1.51] R.E. Loehman, A.P. Tomsia, J.A. Pask and S.M. Johnson: *J. Amer. Ceram. Soc.*, 1990, Vol. 73, pp. 552-558.

[1.52] M. Naka, M. Tsuyoshi and I. Okamoto: *ISIJ Int.*, 1991, Vol. 30, pp. 1108-1113.

[1.53] T. Kuzumaki, T. Ariga, Y. Miyamoto: *ISIJ Int.*, 1991, Vol. 30, pp. 1135-1141.

[1.54] Y. Nakao, K. Nishimoto and K. Saida: *ISIJ Int.*, 1991, Vol. 30, pp. 1142-1150.

[1.55] R.E. Loehman and A.P. Tomsia: *Acta Metall. Mater.*, 1992, Vol. 40, Suppl., pp. S75-S83.

[1.56] Y. Morizono, T. Nakata, M. Nishida and A. Chiba: *J. Ceram. Soc. Jpn.*, 1995, Vol. 103, pp. 810-815, in Japanese.

[1.57] A.M. Hadian, R.A.L. Drew: *J. Amer. Ceram. Soc.*, 1996, Vol. 79, pp. 659-665.

[1.58] S.D. Peteves, M. Paulasto, G. Ceccone and V. Stamos: *Acta Mater.*, 1998, Vol. 46, pp. 2407-2414.

[1.59] H. Xiong, C. Wan and Z. Zhou: *Metall. Mater. Trans. A*, 1998, Vol. 29A, pp. 2591-2596.

[1.60] C. Iwamoto and S.-I. Tanaka: *Acta Mater.*, 1998, Vol. 46, pp. 2381-2386.

[1.61] M. Nomura, C. Iwamoto and S.-I. Tanaka: *Acta Mater.*, 1999, Vol. 47, pp. 407-413.

[1.62] A.M. Hadian and R.A.L. Drew: *J. Euro. Ceram. Soc.*, 1999, Vol. 19, pp.1623-1629.

[1.63] M. Naka: *Bonding Metals to Ceramics*, N. Iwamoto and S. Somiya (Eds.), Uchida Rokakuho Publ., Tokyo (Japan), 1990, pp. 95-105, in Japanese.

[1.64] S.-I. Tanaka: *Bonding Metals to Ceramics*, N. Iwamoto and S. Somiya (Eds.), Uchida Rokakuho Publ., Tokyo (Japan), 1990, pp. 191-209, in Japanese.

[1.65] A. Suzumura: *Bonding Metals to Ceramics*, N. Iwamoto and S. Somiya (Eds.), Uchida Rokakuho Publ., Tokyo (Japan), 1990, pp. 265-283, in Japanese.

[1.66] M. Nakahashi and S. Suenaga: *Bull. Ceram. Soc. Jpn.*, 1995, Vol. 30, pp. 102-105, in Japanese.

[1.67] Y. Iino: *J. Mater. Sci. Lett.*, 1990, Vol. 10, pp. 104-106.

[1.68] G. Ceccone, M.G. Nicholas, S.D. Peteves, A.P. Tomsia, B.J. Dalgleish and A.M. Glaeser: *Acta Mater.*, 1996, Vol. 44, pp. 657-667.

[1.69] M. Paulasto, G. Ceccone and S.D. Peteves: *Scripta Mater.*, 1997, Vol. 36, pp. 1167-1173.

[1.70] K. Suganuma, T. Okamoto, Y. Miyamoto, M. Shimada and M. Koizumi: *Mater. Sci. Technol.*, 1986, Vol. 2, pp. 1156-1161.

[1.71] K. Suganuma, T. Okamoto and K. Kamachi: *J. Mater. Sci.*, 1987, Vol. 22, pp. 2702-2706.

[1.72] Y. Iino and N. Taguchi: *J. Mater. Sci. Lett.*, 1988, Vol. 7, pp. 981-982.

[1.73] M. Nakamura and S.D. Peteves: *J. Amer. Ceram. Soc.*, 1990, Vol. 73, pp. 1221-1227.

[1.74] S. Morozumi, K. Hamaguchi, M. Iwasaki, M. Kikuchi and Y. Minonishi: *J. Jpn. Inst. Met.*, 1990, Vol. 54, pp. 1392-1400.

[1.75] I.E. Reimanis: *Acta Metall. Mater.*, 1992, Vol. 40, Suppl., pp. S67-S74.

[1.76] A. Frisch, W.A. Kaysser, W. Zhang and G. Petzow: *Acta Metall. Mater.*, 1992, Vol. 40, Suppl., pp. S361-S368.

[1.77] S.D. Peteves, M. Moulaert and M.G. Nicholas: *Metall. Mater. Trans. A*, 1992, Vol. 23A, pp. 1773-1781.

[1.78] Y. Ito, K. Kitamura and M. Kanno: *J. Mater. Sci.*, 1993, Vol. 28, pp. 5014-5018.

[1.79] B.T.J. Stoop and G. den Ouden: *Metall. Mater. Trans. A*, 1993, Vol. 24A, pp. 1835-1843.

[1.80] B.T.J. Stoop and G. den Ouden: *Metall. Mater. Trans. A*, 1995, Vol. 26A, pp. 203-208.

[1.81] Y.C. Chen, C. Iwamoto and Y. Ishida: *Scripta Mater.*, 1996, Vol. 35, pp. 675-681.

[1.82] L. Eposito, A. Bellosi and G. Celotti: *Acta Mater.*, 1997, Vol. 45, pp. 5087-5097.

[1.83] M. Naka, J.C. Feng, and J.C. Schuster: *Metall. Mater. Trans. A*, 1997, Vol. 28A, pp. 1385-1390.

[1.84] W.-C. Lee: *J. Mater. Sci.*, 1997, Vol. 32, pp. 221-228.

[1.85] R.H. Vegter and G. den Ouden: *J. Mater. Sci.*, 1998, Vol. 33, pp. 4525-4530.

[1.86] A.E. Martinelli and R.A.L. Drew: J. Euro. Ceram. Soc., 1999, Vol. 19, pp. 2173-2181.

[1.87] R.H. Vegter, M. Maeda, M. Naka and G. den Ouden: *J. Mater. Sci.*, 2002, Vol. 37, pp. 1179-1182.

[1.88] T. Ishikawa, M.E. Brito, Y. Inoue, Y. Hirotsu and A. Miyamoto: *ISIJ Int.*, 1990, Vol. 30, pp. 1071-1077.

[1.89] A. Nishimoto, M. Ando, M. Takahashi, M. Aritoshi and K. Ikeuchi: *Mater. Trans., Jpn. Inst. Met.*, 1999, Vol. 40, pp. 953-956.

[1.90] A. Nishimoto, M. Ando, M. Takahashi, M. Aritoshi and K. Ikeuchi: *Mater. Trans., Jpn. Inst. Met.*, 2000, Vol. 41, pp. 1636-1645.

[1.91] T. Watanabe and T. Saito: *J. Jpn. Inst. Light Met.*, 2000, Vol. 50, pp. 313-319, in Japanese.

[1.92] K. Kobayashi, K. Ozaki and A. Sugiyama: *J. Jpn. Soc. Powder and Powder Metall.*, 1997, Vol. 44, pp. 275-279, in Japanese.

[1.93] K. Nogi, H. Takeda and K. Ogino: *ISIJ Int.*, 1990, Vol. 30, pp. 1092-1100.

[1.94] A. Shimpo, T. Nakano and H. Kubo: *ISIJ Int.*, 1990, Vol. 30, pp. 1101-1107.

[1.95] T. Suga: *Bull. Jpn. Inst. Met.*, 1990, Vol. 29, pp. 944-947, in Japanese.

[1.96] B. Gibbesch and G. Elssner: *Acta Metall. Mater.*, 1992, Vol. 40, Suppl., pp. S59-S66.

[1.97] T. Suga, Y. Takahashi, H. Takagi, B. Gibbesch and G. Elssner: *Acta Metall. Mater.*, 1992, Vol. 40, Suppl., pp. S133-S137.

[1.98] D. Korn, G. Elssner, H.F. Fischmeister and M. Rühle: *Acta Metall. Mater.*, 1992, Vol. 40, Suppl., pp. S355-S360.

[1.99] T. Suga: *Bull. Ceram. Soc. Jpn.*, 1995, Vol. 30, pp. 106-109, in Japanese.

[1.100] K. Suganuma: *ISIJ Int.*, 1990, Vol. 30, pp. 1046-1058.

[1.101] Y.C. Kim, K. Saida, Y. Zhou and T.H. North: *Trans. Jpn. Weld. Res. Inst.*, 1993, Vol. 22, No. 1, pp. 121-126.

[1.102] T. Yamamoto, T. Takashima and K. Sato: *J. Ceram. Soc. Jpn.*, 1996, Vol. 104, pp. 535-539, in Japanese.

[1.103] Y. Arai, E. Tsuchida, J. Miyagaki, M. Yoshino and M.J. Meisner: *J. Soc. Mater. Sci. Jpn.*, 1997, Vol. 46, pp. 952-956, in Japanese.

[1.104] J.H. Kim and S.B. Lee: *Theoret. Appl. Fracture Mechanics*, 1998, Vol. 30, pp. 27-38.

[1.105] J.Q. Li, X.R. Zeng, J.N. Tang and P. Xiao: *J. Euro. Ceram. Soc.*, 2003, Vol. 23, pp. 1847-1853.

[1.106] Y. Ishida: *Bull. Jpn. Inst. Met.*, 1990, Vol. 29, pp. 888-892, in Japanese.

[1.107] Y. Ishida, J.-Y. Wang and T. Suga: *ISIJ Int.*, 1990, Vol. 30, pp. 1041-1045.

[1.108] Y. Ishida, J. Wang and T. Suga: *Acta Metall. Mater.*, 1992, Vol. 40, Suppl., pp. S289-S293.

[1.109] S.-I. Tanaka and Y. Takahashi: *ISIJ Int.*, 1990, Vol. 30, pp. 1086-1091.

[1.110] S.-I. Tanaka: *Bull. Jpn. Inst. Met.*, 1990, Vol. 29, pp. 924-930, in Japanese.

[1.111] S.-B. Lee and J.-H. Kim: *J. Mater. Process. Technol.*, 1997, Vol. 67, pp. 167-172.

[1.112] T. Narita: *Bull. Jpn. Inst. Met.*, 1990, Vol. 29, pp. 918-923.

[1.113] Y.-C. Kim: *J. Jpn. Weld. Soc.*, 1996, Vol. 65, pp. 319-323.

[1.114] J.-W. Park, P.F. Mendez and T.W. Eagar: *Acta Mater.*, 2002, Vol. 50, pp. 883-899.

[1.115] H. Serizawa, C.A. Lewinsohn and H. Murakawa: *Mater. Trans.*, 2002, Vol. 43, pp. 994-1000.

[1.116] H. Serizawa, C.A. Lewinsohn and H. Murakawa: *Trans. Join. Weld. Res. Inst.*, 2002, Vol. 31, pp. 71-76.

[1.117] M. Takahashi, N. Okabe, X. Zhu and K.-I. Kagawa: *J. Soc. Mater. Sci. Jpn.*, 2001, Vol. 50, pp. 7-12, in Japanese.

[1.118] *Testing Method for Bending Strength of Fine Ceramic Joint*, Japanese Industrial Standard, 1995, R 1624.

[1.119] *Test Methods for Tensile Strength of Fine Ceramic Joint*, Japanese Industrial Standard, 1997, R 1630.

[1.120] *Tension and Vacuum Testing Metallized Ceramic Seals*, ASTM Specification F19-64, American Society for Testing and Materials Standards, Part 8, 1964, pp. 336.

[1.121] References 1.45, 1.47, 1.48, 1.57, 1.59, 1.68, 1.69, 1.72, 1.94, 1.102, 1.103, 1.104.

[1.122] References 1.52, 1.53, 1.56, 1.78, 1.79, 1.80, 1.84, 1.85, 1.86.

[1.123] H. Fujii and H. Nakae: *ISIJ Int.*, 1990, Vol. 30, pp. 1114-1118.

[1.124] J.C. Schuster: *J. Mater Sci.*, 1988, Vol. 23, pp. 2792-2796.

[1.125] J.C. Schuster, F. Weitzer, J. Bauer and H. Nowotny: *Mater. Sci. Engineer.*, 1988, Vol. A105/106, pp. 201-206.

[1.126] I. Gotman and E.Y. Gutmanas: *J. Mater. Sci. Lett.*, 1990, Vol. 9, pp. 813-815.

[1.127] I. Gotman and E.Y. Gutmanas: *Acta Metall. Mater.*, 1992, Vol. 40, pp. S121-131.

[1.128] T. Shimoo, Y. Kobayashi and K. Okamura: *J. Ceram. Soc. Jpn.*, 1992, Vol. 100, pp. 808-814, in Japanese.

[1.129] T. Shimoo, Y. Moriuchi and K. Okamura: *J. Jpn. Inst. Met.*, 1992, Vol. 56, pp. 1030-1036, in Japanese.

[1.130] T. Shimoo, Y. Kobayashi and K. Okamura: *J. Ceram. Soc. Jpn.*, 1993, Vol. 101, pp. 675-680, in Japanese.

[1.131] T. Shimoo, Y. Kobayashi and K. Okamura: *J. Ceram. Soc. Jpn.*, 1993, Vol. 101, pp. 1012-1017, in Japanese.

[1.132] T. Shimoo and K. Okamura: *J. Mater. Sci.*, 1994, Vol. 29, pp. 2231-2237.

[1.133] T. Shimoo, S. Adachi and K. Okamura: *J. Jpn. Inst. Met.*, 1994, Vol. 58, pp. 796-802, in Japanese.

[1.134] T. Shimoo, T. Yamazaki and K. Okamura: *J. Jpn. Inst. Met.*, 1995, Vol. 59, pp. 415-422, in Japanese.

[1.135] T. Shimoo, S.-I. Adachi and K. Okamura: *J. Ceram. Soc. Jpn.*, 1995, Vol. 103, pp. 1027-1032, in Japanese.

[1.136] T. Shimoo, D. Shibata, T. Yamasaki and K. Okamura: *J. Ceram. Soc. Jpn.*, 1997, Vol. 105, pp. 52-56, in Japanese.

[1.137] T. Shimoo, K. Okamura and S. Adachi: *J. Mater. Sci.*, 1997, Vol. 32, pp. 3031-3036.

[1.138] T. Shimoo, D. Shibata and K. Okamura: *J. Ceram. Soc. Jpn.*, 1998, Vol. 106, pp. 545-550.

[1.139] T. Shimoo, K. Okamura and M. Itoh: *J. Mater. Sci.*, 1998, Vol. 33, pp. 5169-5175.

[1.140] T. Shimoo, K. Okamura and T. Yamasaki: *J. Mater. Sci.*, 1999, Vol. 34, pp. 5525-5532.

[1.141] T. Shimoo, K. Okamura and D. Shibata: *J. Mater. Sci.*, 2000, Vol. 35, pp. 5485-5492.

[1.142] References 1.45, 1.47, 1.48, 1.49, 1.50, 1.51, 1.52, 1.53, 1.54, 1.55, 1.56, 1.57, 1.58, 1.59, 1.62, 1.66, 1.68, 1.69, 1.70, 1.71, 1.72, 1.73, 1.74, 1.76, 1.78, 1.79, 1.80, 1.81, 1.82, 1.84, 1.85, 1.86, 1.88, 1.100, 1.102, 1.105, 1.106, 1.107, 1.123.

[1.143] T. Okamoto: *ISIJ Int.*, 1990, Vol. 30, pp. 1033-1040.

[1.144] T. Wagner, R. Kirchheim and M. Rühle: *Acta Metall. Mater.*, 1992, Vol. 40, Suppl., pp. S85-S93.

[1.145] M. Backhaus-Ricoult: *Acta Metall. Mater.*, 1992, Vol. 40, Suppl., pp. S95-S103.

[1.146] E. Heikinheimo, A. Kodentsov, J.A. van Beek, J.T. Klomp and F.J.J. van Loo: *Acta Metall. Mater.*, 1992, Vol. 40, Suppl., pp. S111-S119.

[1.147] M. Paulasto, J.K. Kivilahti and F.J.J. van Loo: *J. Appl. Phys.*, 1995, Vol. 77, pp. 4412-4416.

[1.148] J. Lemus and R.A.L. Drew: *British Ceram. Trans.*, 2000, Vol. 99, pp. 200-205.

[1.149] F.S. Ohuchi and Q. Zhong: *ISIJ Int.*, 1990, Vol. 30, pp. 1059-1065.

[1.150] F.S. Ohuchi: *Bull. Jpn. Inst. Met.*, 1990, Vol. 29, pp. 902-909, in Japanese.

[1.151] C.H. Lee and K.S. Liang: *Acta Metall. Mater.*, 1992, Vol. 40, Suppl., pp. S143-S147.

[1.152] W. Mader and D. Knauss: *Acta Metall. Mater.*, 1992, Vol. 40, Suppl., pp. S207-S215.

[1.153] J. Mayer, G. Gutekunst, G. Möbus, J. Dura, C.P. Flynn and M. Rühle: *Acta Metall. Mater.*, 1992, Vol. 40, Suppl., pp. S217-S225.

[1.154] A. Trampert, F. Ernst, C.P. Flynn, H.F. Fischmeister and M. Rühle: *Acta Metall. Mater.*, 1992, Vol. 40, Suppl., pp. S227-S236.

[1.155] D.X. Li, P. Pirouz, A.H. Heuer, S. Yadavalli and C.P. Flynn: *Acta Metall. Mater.*, 1992, Vol. 40, Suppl., pp. S237-S247.

[1.156] K.L. Merkle, M.I. Buckett and Y. Gao: *Acta Metall. Mater.*, 1992, Vol. 40, Suppl., pp. S249-S257.

[1.157] P. Lu and F. Cosandey: *Acta Metall. Mater.*, 1992, Vol. 40, Suppl., pp. S259-S266.

[1.158] M. Kohyama and R. Yamamoto: *Bull. Jpn. Inst. Met.*, 1990, Vol. 29, pp. 893-901, in Japanese.

[1.159] U. Schönberger, O.K. Andersen and M. Methfessel: *Acta Metall. Mater.*, 1992, Vol. 40, Suppl., pp. S1-S10.

[1.160] W.R.L. Lambrecht and B. Segall: *Acta Metall. Mater.*, 1992, Vol. 40, Suppl., pp. S17-S24.

[1.161] M.W. Finnis: *Acta Metall. Mater.*, 1992, Vol. 40, Suppl., pp. S25-S37.

[1.162] D.M. Duffy, J.H. Harding and A.M. Stoneham: *Acta Metall. Mater.*, 1992, Vol. 40, Suppl., pp. S11-S16.

[1.163] H.J. Fecht: *Acta Metall. Mater.*, 1992, Vol. 40, Suppl., pp. S39-S44.

[1.164] C.P. Flynn and S. Yadavalli: *Acta Metall. Mater.*, 1992, Vol. 40, Suppl., pp. S45-S52.

[1.165] *Metals Data Book*, Third Edition, The Japan Institute of Metals, Maruzen, Tokyo (Japan), 1993, in Japanese.

[1.166] J. Emsley: *The Elements*, Second Edition, Clarendon Press, Oxford (UK), 1991.

[1.167] *Powder Diffraction Files*, JCPDS–International Centre for Diffraction Data, Newtown Square, Pennsylvania (USA), 44-1288.

[1.168] *Powder Diffraction Files*, JCPDS–International Centre for Diffraction Data, Newtown Square, Pennsylvania (USA), 44-1294.

[1.169] *Powder Diffraction Files*, JCPDS–International Centre for Diffraction Data, Newtown Square, Pennsylvania (USA), 22-1058.

[1.170] *Powder Diffraction Files*, JCPDS–International Centre for Diffraction Data, Newtown Square, Pennsylvania (USA), 35-789.

Chapter 2 Theories on the Background

This chapter describes some of the essential theories on which the present study stands. Physical, chemical and mechanical phenomena are simultaneously taking their place at the interface of the joints during diffusion bonding. Therefore, the observed phenomena should be analyzed from multiple viewpoints with established theories in order to understand the entire phenomena occurring at the interface. In this chapter, the metallurgical thermodynamics, diffusion theory and basic theories on experimental techniques of X-ray diffraction and electron probe microanalysis are described.

I. Metallurgical Thermodynamics [2.1, 2.2, 2.3]

A. The First Law of Thermodynamics

Once the state of a system changes from state I to II by an input of external energy (Q) and by a work done by the system (W), the change of the internal energy (ΔU) is described as

$$\Delta U = Q - W \tag{2.1}$$

on the basis of the energy conservation law. This equation is called the First Law of Thermodynamics. This law implies that the change of the internal energy is determined only by the two terminal states, I and II, being independent to the path of the change (Hess' principle). Therefore, if once the standard state is defined, any state of the system can be described as the deviation from the standard state. The state of the system at the temperature of 298 K is defined as the standard.

The work done by the system (W) can be described using the atmospheric pressure (P) and the volume of the system (V) as ΔPV. The external energy required for changing the state

in the isobaric condition is defined with the following equation, called enthalpy (H).

$$\Delta Q_P = \Delta H = \Delta U + P\Delta V. \tag{2.2}$$

The enthalpy of elementary substances at the standard state (P = 101325 Pa, T = 298 K) is defined to be zero.

Since the internal energy of a system is reflected to its temperature (T), the relation between the temperature and the energy is required. The isobaric molar heat capacity (c_P) is therefore defined as the energy required to raise the temperature of unit mole of the system up 1 K with the following equation:

$$c_P = \frac{dQ_P}{dT} = \left(\frac{\partial H}{\partial T}\right)_P \text{ or } \Delta H = \int_{\Delta T} c_P dT\ . \tag{2.3}$$

The isobaric molar heat capacity is a function of the temperature. The values of c_P is obtained experimentally and listed on the thermodynamic databases [2.3] using the following empirical description:

$$c_P\,(T) = a + bT + cT^{-2} + dT^2 + eT^{-1/2}, \tag{2.4}$$

where a, b, c, d, and e are constants. In order to describe $c_P\,(T)$ in a selected temperature range, the equation (2.4) can be simplified to

$$c_P\,(T) = a + bT. \tag{2.5}$$

The first-order phase-transition, such as vaporization, melting, and solid-state phase transformation, induces a latent heat at the temperature of phase transition. The enthalpy of phase transition (ΔH_T) is expressed as a constant, accompanied with the value of the phase-transition temperature, on the thermodynamic databases. The enthalpy of the system at a certain temperature (T) is described as

$$\Delta H(T) = \int_{298}^{T_1} c_{P1} dT + \Delta H_T(T_1) + \int_{T_1}^{T_2} c_{P2} dT + \cdots + \int_{T_{n-1}}^{T} c_{Pn} dT \tag{2.6}$$

where $T_1 \sim T_{n-1}$ are the phase-transition temperatures, $c_{P1} \sim c_{Pn}$ are respectively the heat capacity of phases 1 to n.

Reaction is a phenomenon that multiple different systems come into contact and interact exchanging their constituent elements to form a system different from the original systems. The enthalpy of reaction (ΔH^R) is defined as the difference between the enthalpy of the product system (ΔH^p) and the total enthalpy of the reactant systems (ΔH^r) as

$$\Delta H^R = \Delta H^p - \Delta H^r. \tag{2.7}$$

Differentiating both sides of the formula (2.7) by temperature in isobaric condition, the formula is transformed as

$$\left(\frac{\partial H^R}{\partial T}\right)_P = \left(\frac{\partial H^p}{\partial T}\right)_P - \left(\frac{\partial H^r}{\partial T}\right)_P = c_P^p - c_P^r = \Delta c_P, \tag{2.8}$$

where c_P^p, c_P^r, and Δc_P are respectively the heat capacity of the product system, that of the reactant system, and the difference between them. Hence, the following Kirchhoff's equation is obtained.

$$\Delta H^p = \Delta H^r + \int_{298}^{T} \Delta c_P dT. \tag{2.9}$$

This equation implies that the enthalpy of the product system can be derived from the total enthalpy of the reactant system and the difference of the heat capacity between them, being independent on the path of reaction. Namely, the Hess' principle is established also in the case of reaction.

B. The Second Law of Thermodynamics

The Second Law of Thermodynamics determines whether the change in a system progresses spontaneously or not. Generally, a spontaneous change in a system, like oxidation, is a irreversible process. On the other hand, melting or evaporation at the melting or boiling point are examples of reversible processes. Such reversible processes may be defined as one which is implemented under conditions such that the system at all times differs only infinitesimally from the state of equilibrium, the quasi-static process. Therefore, the energy of change in the system by a irreversible process (δQ_{ir}) is expressed in relation with that by a reversible process (δQ_r) and the uncompensated energy ($\delta Q'$) as

$$\delta Q_{ir} = \delta Q_r - \delta Q' \quad (\delta Q' > 0). \tag{2.10}$$

A consideration on the energy efficiency (η) of a reversible Carnot cycle, which does a work (W) through the process of energy (Q_1) absorption from high-temperature source (T_1) and energy emission (Q_2) to low-temperature source (T_2), results in the following equation:

$$\eta = \frac{W}{Q_1} = \frac{Q_1 - Q_2}{Q_1} = \frac{T_1 - T_2}{T_1}, \text{ hence, } \frac{Q_1}{T_1} - \frac{Q_2}{T_2} = 0. \tag{2.11}$$

Dividing the process to infinitesimal cycle processes, the following equation is obtained.

$$\oint \frac{\delta Q}{T} = 0 \,. \tag{2.12}$$

The equation (2.12) indicates that the $\delta Q / T$ is an exact differential, being independent on the path of change. Therefore, the $\delta Q / T$ is also a state variable. This state variable is called entropy (S). Generally, the following formula is established for any reversible change in closed systems.

$$dS = \delta Q_r / T \,. \tag{2.13}$$

In the next step, the entropy change for irreversible processes should be considered. The First Law of Thermodynamics indicates that the change of internal energy is independent on the path of the process, whether it is reversible or irreversible. Therefore, the following relation is established on the basis of the equation (2.1).

$$dU = \delta Q_r - \delta W_r = \delta Q_{ir} - \delta W_{ir}. \tag{2.14}$$

where the subscript r and ir are respectively indicating the reversible and the irreversible processes. Referring to the equation (2.10), the δQ_r and the δW_r are respectively larger than the δQ_{ir} and the δW_{ir}. Therefore, the following equation is obtained.

$$dS = \frac{\delta Q_r}{T} = \frac{\delta Q_{ir}}{T} + \frac{\delta Q'}{T} > \frac{\delta Q_{ir}}{T} \,. \tag{2.15}$$

The spontaneous change of the system corresponds to the increase in the entropy by increase in the $\delta Q' / T$ which is positive in irreversible processes.

The combination of equations (2.1), (2.2), (2.3) and (2.13) deduces the following relation between enthalpy and entropy in the isobaric condition.

$$T\left(\frac{\partial S}{\partial T}\right)_P = \left(\frac{\partial H}{\partial T}\right)_P = c_P \text{, hence, } \; dS = \frac{c_P}{T} dT \,. \tag{2.16}$$

The third Law of Thermodynamics, postulated by Nernst and extended by Planck, indicates that the entropy of any perfectly ordered crystalline pure substance at 0 K is zero. Unlike the values of enthalpy or internal energy, which are related to arbitrary standards, those of entropy can be determined absolutely. Thus, the equation (2.16) can be modified as

$$S = \int_0^T \frac{c_P}{T} dT \quad . \tag{2.17}$$

If any phase change occurs in the temperature range considered, a transformation, melting or evaporation, its effect on the entropy must be taken into account. Such phase transitions are thermodynamically reversible, in consequence, their associated entropy changes are obtained by dividing the respective latent heats by the temperature at which they occur. The equation (2.16) may then be expanded to the form;

$$S(T) = \int_0^{T_1} \frac{c_P}{T} dT + \frac{Q_T(T_1)}{T_1} + \int_{T_1}^{T_2} \frac{c_P}{T} dT + \cdots + \int_{T_{n-1}}^{T} \frac{c_P}{T} dT \quad . \tag{2.18}$$

C. Gibbs Energy and Equilibrium

Gibbs energy (G) for any substance under given conditions is the maximum portion of its energy which can be converted into mechanical work. Any process which take place is accompanied by the change in Gibbs energy of the system. Gibbs energy is defined as

$$G = H - TS. \tag{2.19}$$

Hence, the differentiation of the equation (2.19) derives the following formula.

$$dG = d(H - TS) = dU + PdV + VdP - TdS - SdT = VdP - SdT. \tag{2.20}$$

Consider the following chemical reaction occurring in a homogeneous system.

$$\nu_A \mathrm{A} + \nu_B \mathrm{B} = \nu_D \mathrm{D} + \nu_E \mathrm{E}, \tag{2.21}$$

where ν_A, ν_B, ν_D, and ν_E are respectively the stoichiometric coefficients. Assuming the composition of each substance as C_A, C_B, C_D, and C_E, respectively, the following relationship is established on the basis of the mass action law at the equilibrium state.

$$K = \frac{C_D^{\nu_D} C_E^{\nu_E}}{C_A^{\nu_A} C_B^{\nu_B}} = \text{constant}, \tag{2.22}$$

where K is the equilibrium constant. The equilibrium constant changes depending on the temperature, while it is independent on the composition.

When two different substances come into contact, the tendency to form a bond is estimated by the Gibbs energy. Since the chemical reaction is implemented under an isothermal and isobaric condition, the chemical affinity is quantitatively evaluated by the reduction in the Gibbs energy as follows.

$$\Delta G = G_{product} - G_{reactant}. \tag{2.23}$$

If the change in Gibbs energy by the reaction is negative, the reaction occurs spontaneously.

When it is positive, the reverse-reaction proceeds. When it is zero, the system is in an equilibrium state. Therefore, the value of $-\Delta G$ is called the "driving force." It points out the direction of the reaction, its tendency, and the state of the equilibrium. The condition for equilibrium is expressed as

$$\Delta G = 0 \,. \tag{2.24}$$

Gibbs Energy is a state variable, which absolute value cannot obtained like enthalpy. Therefore, the standard state is defined as $P^{\emptyset}$ = 101325 Pa (1 atm). The Gibbs energy for production of unit mole of compound in standard state from pure elemental substances in standard state is defined as the standard Gibbs energy of formation (ΔG^0). In an isothermal condition, the equation (2.20) can be transformed using the state equation of ideal gas as

$$dG = RT\, dP / P \,. \tag{2.25}$$

Integrating this equation from the standard state ($P^{\emptyset}$, G^0) to an arbitrary state (T, P, G),

$$G = G^0 + RT \ln (P / P^{\emptyset}) = G^0 + RT \ln p \,, \tag{2.26}$$

where p is the dimensionless pressure which value equals to the pressure in atm unit, is obtained. Considering the reaction (2.21) with substances A, B, D, and E to be ideal gases with each partial pressure being respectively P_A, P_B, P_D and P_E (*i.e.* the dimensionless partial pressure being respectively p_A, p_B, p_D and p_E), the change in Gibbs energy by the reaction is described using the equation (2.26) as

$$\begin{aligned} \Delta G &= (\nu_D G_D + \nu_E G_E) - (\nu_A G_A + \nu_B G_B) \\ &= \{(\nu_D G_D^0 + \nu_E G_E^0) - (\nu_A G_A^0 + \nu_B G_B^0)\} + RT \ln \frac{p_D^{\nu_D} p_E^{\nu_E}}{p_A^{\nu_A} p_B^{\nu_B}} \,, \end{aligned} \tag{2.27}$$

which is called the van't Hoff's isotherm. At the equilibrium state, the equation (2.27) can be transformed using equations (2.22) and (2.24) as

$$\Delta G = \Delta G^0 + RT \ln K = 0 \,, \quad \text{hence,} \quad \Delta G^0 = -RT \ln K \,. \tag{2.28}$$

The equations (2.25) to (2.28) are derived on an assumption of ideal gas. Although it is possible to derive the equations for non-ideal gases in the same way, the obtained equations are complex and less useful. Therefore, fugacity (f), the corrected partial pressure, is defined to establish the compatibility with the equations (2.25) to (2.28). However, the difference between the fugacity and the partial pressure is generally small, usually the partial pressure can be used also in the case of non-ideal gases.

D. Solution, Activity and Chemical Potential

Solution is defined as a homogeneous condensed system consisting of two or more constituents. In such systems, the atomic interaction among the elements is generally different. Consequently, an ideal state of solution is defined by the Raoult's law. Every element in the ideal solution satisfies the following condition;

$$P_i = P_i^o N_i \ , \tag{2.29}$$

where P_i is the partial pressure of the element *i* in equilibrium with the solution, P_i^o is the pressure of the pure substance of the element *i*, N_i is the mole fraction of the element *i* in the solution.

The partial pressure of an element in equilibrium with the solution system reflects the interaction between the element and other constituents. The attractive interaction reduces the partial pressure of the element, while the repulsive interaction increases the partial pressure. Therefore, the partial pressure P_i for actual gas becomes different from that derived using the state equation of ideal gas. In order to compensate this deviation, fugacity is defined to replace the partial pressure as

$$f V = RT \ . \tag{2.30}$$

Thus, the reactivity of the actual gas can be successfully expressed with the fugacity. On the other hand, in order to reflect the correct reactivity of the condensed solution, activity (a_i) is defined to replace the composition or the molar fraction of the element *i* as;

$$a_i = f_i \big/ f_i^0 \ , \tag{2.31}$$

where f_i^0 is the fugacity of the pure substance of the element *i*. Hence, the equilibrium constant in equation (2.22) is more precisely expressed in the following equation.

$$K = \frac{a_D^{\nu_D} a_E^{\nu_E}}{a_A^{\nu_A} a_B^{\nu_B}} = \text{constant} \ . \tag{2.32}$$

Chemical potential of the element *i* (μ_i) is an alias of the partial molar Gibbs energy. It is defined as the contribution of unit mole of the element *i* to the Gibbs energy of the solution system with the following expression;

$$\mu_i = \left(\frac{\partial G}{\partial N_i} \right)_{T,P,N_j (j \neq i)} = RT \ln a_i \ . \tag{2.33}$$

E. Phase Diagram and Chemical Potential Diagram

Both phase diagrams and chemical potential diagrams describe the relation of phases which are stable at the state (T, P, N_i). Phase diagrams can be said as those oriented for manufacturers or engineers of materials. They are useful for prediction of the existing phases and the fraction of each coexisting phases at a known temperature, pressure, and composition. The mass fraction is taken as the compositional axis for manufacture-oriented diagrams, while the molar fraction is taken for crystallographic- and defect-engineering-oriented diagrams. On the other hand, chemical potential diagrams are oriented for scientists of materials chemistry. Chemical potential diagrams are used for understanding phase equilibria from the energy state of each element.

For almost of inorganic binary systems and numerous industrially-important ternary systems, phase diagrams are available from the literature [2.5–2.7]. However, chemical potential diagrams are scarcely available. Therefore, each chemical potential diagram is usually required to be constructed by oneself. Since both phase diagrams and chemical potential diagrams describe the relation of phases which are stable at the state, the constructed chemical potential diagram must be consistent with the corresponding phase diagram. In the following section, a method to construct a chemical potential diagram of V-Si-N ternary system at 1473 K is presented for example.

In the V-Si-N ternary system, ten phases can exist stably at 1473 K [2.8, 2.9, 2.10]: V, V_3Si, V_5Si_3, V_6Si_5, VSi_2, Si, V_2N, VN, Si_3N_4, and $V_5Si_3N_{1-X}$. The standard Gibbs energy of formation for each compound phase is known as follows [2.8];

$$\frac{3}{7}\mathrm{Si} + \frac{2}{7}\mathrm{N_2} = \frac{1}{7}\mathrm{Si_3N_4} \qquad \Delta G^0 = -124602 + 57.95\ T, \tag{2.34}$$

$$\frac{1}{3}\mathrm{V} + \frac{2}{3}\mathrm{Si} = \frac{1}{3}\mathrm{VSi_2} \qquad \Delta G^0 = -40700 + 3.15\ T, \tag{2.35}$$

$$\frac{6}{11}\mathrm{V} + \frac{5}{11}\mathrm{Si} = \frac{1}{11}\mathrm{V_6Si_5} \qquad \Delta G^0 = -49600 + 3.10\ T, \tag{2.36}$$

$$\frac{5}{8}\mathrm{V} + \frac{3}{8}\mathrm{Si} = \frac{1}{8}\mathrm{V_5Si_3} \qquad \Delta G^0 = -53800 + 4.10\ T, \tag{2.37}$$

$$\frac{3}{4}\mathrm{V}+\frac{1}{4}\mathrm{Si}=\frac{1}{4}\mathrm{V_3Si} \qquad \Delta G^0 = -43100 + 3.33\,T, \tag{2.38}$$

$$\frac{1}{3}\mathrm{V}+\frac{1}{3}\mathrm{N_2}=\frac{1}{3}\mathrm{V_2N} \qquad \Delta G^0 = -83719 + 19.79\,T, \tag{2.39}$$

$$\frac{1}{2}\mathrm{V}+\frac{1}{4}\mathrm{N_2}=\frac{1}{2}\mathrm{VN} \qquad \Delta G^0 = -101249 + 20.07\,T. \tag{2.40}$$

The standard Gibbs energy of formation for $V_5Si_3N_{1-X}$ is not found on the literature. The energy of the $V_5Si_3N_{1-X}$ will be discussed later. Before that, it is required to proceed without this information. On the basis of equations (2.28) and (2.32), the relation among the activity of vanadium (a_V) and silicon (a_{Si}) and the dimensionless partial pressure of nitrogen (p_{N2}) for each compound phase is derived as follows;

for Si_3N_4: $3 \ln a_{Si} + 2 \ln p_{N2} = -22.43$, (2.41)

for VSi_2: $\ln a_V + 2 \ln a_{Si} = -8.83$, (2.42)

for V_6Si_5: $6 \ln a_V + 5 \ln a_{Si} = -40.45$, (2.43)

for V_5Si_3: $5 \ln a_V + 3 \ln a_{Si} = -31.20$, (2.44)

for V_3Si: $3 \ln a_V + \ln a_{Si} = -12.47$, (2.45)

for V_2N: $4 \ln a_V + \ln p_{N2} = -26.73$, (2.46)

for VN: $2 \ln a_V + \ln p_{N2} = -23.41$. (2.47)

In the next step, each two-phase equilibrium of binary compounds is considered referring to the corresponding phase diagram [2.8, 2.9, 2.10]. The equilibrium condition are obtained as the solution of simultaneous equations selected from (2.41) to (2.47), corresponding to each phase, as follows;

for Si / VSi_2 equilibrium: $\ln a_V = -8.83$, $\ln a_{Si} = 0$, (2.48)

for VSi_2 / V_6Si_5 equilibrium: $\ln a_V = -5.25$, $\ln a_{Si} = -1.79$, (2.49)

for V_6Si_5 / V_5Si_3 equilibrium: $\ln a_V = -4.95$, $\ln a_{Si} = -2.15$, (2.50)

for V_5Si_3 / V_3Si equilibrium: $\ln a_V = -1.56$, $\ln a_{Si} = -7.81$, (2.51)

for V_3Si / V equilibrium: $\ln a_V = 0$, $\ln a_{Si} = -12.47$, (2.52)

for Si / Si_3N_4 equilibrium: $\ln a_{Si} = 0$, $\ln p_{N2} = -11.21$, (2.53)

for V / V_2N equilibrium: $\ln a_V = 0$, $\ln p_{N2} = -26.73$, (2.54)

for V_2N / VN equilibrium: $\ln a_V = -1.66$, $\ln p_{N2} = -20.09$. (2.55)

The three-phase equilibria of two vanadium-silicide phases and one vanadium- or silicon-nitride phase are then considered. The result is summarized on **Table 2.1**. Since only the most stable combination of phases is allowed to exist in the equilibrium state, the nitride phase allowed to coexist with each two vanadium-silicide phases are determined to be the phase indicated without hatching in the table, *i.e.*, the following phase equilibria are stable; Si / VSi_2 / Si_3N_4, VSi_2 / V_6Si_5 / VN, V_6Si_5 / V_5Si_3 / VN, V_5Si_3 / V_3Si / V_2N, and V_3Si / V / V_2N.

Table 2.1 Consideration of three-phase equilibria for two vanadium-silicide phases and one vanadium- or silicon-nitride phase.

V-Si binary equilibrium condition			eq. with V_2N	eq. with VN	eq. with Si_3N_4
	$\ln a_V$	$\ln a_{Si}$	$\ln p_{N2}$	$\ln p_{N2}$	$\ln p_{N2}$
Si / VSi_2	*–8.83*	*0*	*8.60*	*–5.75*	*–11.21*
VSi_2 / V_6Si_5	*–5.25*	*–1.79*	*–5.74*	*–12.92*	*–8.53*
V_6Si_5 / V_5Si_3	*–4.95*	*–2.15*	*–6.94*	*–13.51*	*–7.99*
V_5Si_3 / V_3Si	*–1.56*	*–7.81*	*–20.51*	*–20.30*	*0.49*
V_3Si / V	*0*	*–12.47*	*–26.73*	*–23.41*	*7.50*

Table 2.1 indicates also the three-phase equilibria of two nitrides and one vanadium silicide to be V_2N / VN / V_5Si_3 and VN / Si_3N_4 / VSi_2. The condition of chemical potential at these phase equilibria are also derived respectively from the simultaneous equations (2.44), (2.46), and (2.47), and (2.41), (2.42), and (2.47) as follows.

for V_2N / VN / V_5Si_3 equilibrium: $\ln a_V = -1.66$, $\ln a_{Si} = -7.63$, $\ln p_{N2} = -20.09$, (2.56)

for VN / Si_3N_4 / VSi_2 equilibrium: $\ln a_V = -6.84$, $\ln a_{Si} = -0.99$, $\ln p_{N2} = -9.72$. (2.57)

Then, the energy state of the $V_5Si_3N_{1-X}$ phase should be taken into consideration at this step of procedure. At first, an assumption on the chemical stoichiometry of $V_5Si_3N_{1-X}$ is made to simplify the calculation to be V_5Si_3N. Therefore the standard Gibbs energy of formation of $V_5Si_3N_{1-X}$ is described as

$$\frac{5}{9}\mathrm{V}+\frac{3}{9}\mathrm{Si}+\frac{1}{18}\mathrm{N_2}=\frac{1}{9}\mathrm{V_5Si_3N}\,,\quad \Delta G=\Delta G^0+RT\ln\frac{a_{V_5Si_3N}^{1/9}}{a_V^{5/9}a_{Si}^{3/9}p_{N_2}^{1/18}}=0\,,$$

$$\text{hence,}\quad 10\ln a_V + 6\ln a_{Si} + \ln p_{N_2} = \frac{18\Delta G^0}{RT} \equiv \xi\,. \tag{2.58}$$

Although the precise data of its standard Gibbs energy of formation is missing, the range of ξ can be restricted on the basis of the equilibria with other existing phases and the conditions of equilibria for other phases, calculated above. Referring to the phase diagram [2.8], the $V_5Si_3N_{1-X}$ phase coexists with V_3Si, V_5Si_3, V_6Si_5, VSi_2, V_2N, and Si_3N_4, indicating that it cannot coexist with V and Si. Hence, the standard Gibbs energy of formation for $V_5Si_3N_{1-X}$ is limited within a range that allows to coexist with V_3Si, V_5Si_3, V_6Si_5, VSi_2, V_2N, and Si_3N_4 and disallow to coexist with V and Si. From each three-phase equilibrium condition, the following inequality formula are deduced;

$$\text{from } VSi_2 / Si_3N_4 / V_5Si_3N \text{ equilibrium:}\quad -99.54 < \xi < -84.14, \tag{2.59}$$

$$\text{from } V_6Si_5 / VSi_2 / V_5Si_3N \text{ equilibrium:}\quad \xi < -76.15. \tag{2.60}$$

$$\text{from } V_5Si_3 / V_6Si_5 / V_5Si_3N \text{ equilibrium:}\quad \xi < -76.74, \tag{2.61}$$

$$\text{from } V_3Si / V_5Si_3 / V_5Si_3N \text{ equilibrium:}\quad \xi < -82.90, \tag{2.62}$$

$$\text{from } V_2N / V_3Si / V_5Si_3N \text{ equilibrium:}\quad -101.58 < \xi < -82.90, \tag{2.63}$$

Hence, the range of the value of ξ fulfilling all these conditions is

$$-99.54 < \xi < -84.14\,. \tag{2.64}$$

Therefore, the standard Gibbs energy of formation for $V_5Si_3N_{1-X}$ must take a value fulfilling this condition. Assuming the value of ξ to be –86.00, the condition for each three-phase equilibrium related to $V_5Si_3N_{1-X}$ is derived as listed on **Table 2.2**.

Table 2.2 Conditions for three-phase equilibria related to $V_5Si_3N_{1-X}$.

phases in equilibrium	$\ln a_V$	$\ln a_{Si}$	$\ln p_{N2}$
$VSi_2 / Si_3N_4 / V_5Si_3N_{1-X}$	–7.09	–0.87	–9.90
$V_6Si_5 / VSi_2 / V_5Si_3N_{1-X}$	–5.25	–1.79	–22.77
$V_5Si_3 / V_6Si_5 / V_5Si_3N_{1-X}$	–4.95	–2.15	–23.60
$V_3Si / V_5Si_3 / V_5Si_3N_{1-X}$	–1.56	–7.81	–23.60
$V_2N / V_3Si / V_5Si_3N_{1-X}$	–1.30	–8.58	–21.54

In the final step, the consistency of the chemical potential diagram with the corresponding

phase diagram should be verified. In addition, the phase diagram must obey the phase rule;

$$F = 2 + n - r - s - \phi\,, \qquad (2.65)$$

where F is the freedom of intensive state variables, n is the number of elements in the system, r is the number of equilibrium reactions, s is the number of compositional restriction by stoichiometric relations, and ϕ is the number of existing phases. Comparing the equilibrium conditions calculated above with the V-Si-N ternary phase diagram [2.8], the equilibrium of V_2N appears inconsistent. The phase diagram indicates that V_2N coexists with VN, Si_3N_4, $V_5Si_3N_{1-X}$, V_3Si, and V. Therefore, V_2N extends its stable state in the chemical potential diagram to equilibrate with Si_3N_4. Finally, the chemical potential diagram can be drawn as shown in **Fig. 2.1**, in consistency with the phase diagram and the phase rule.

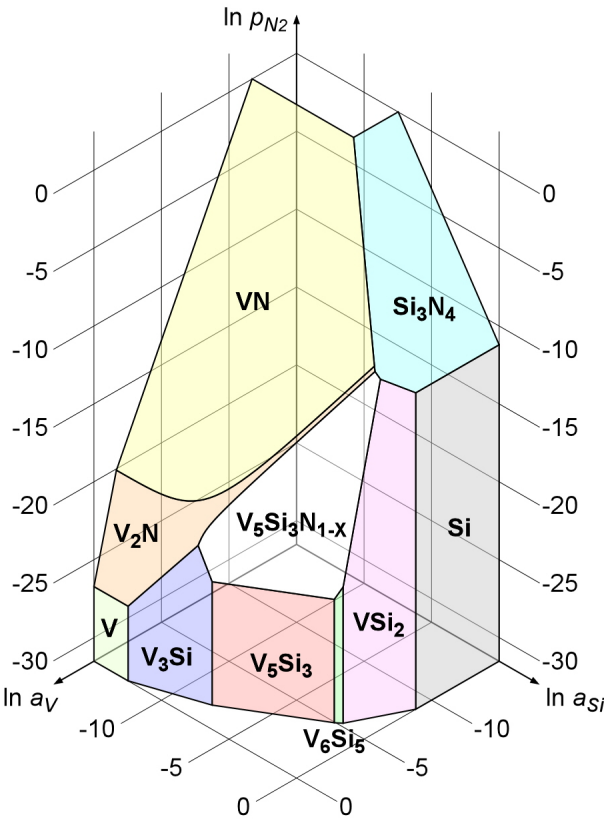

Fig. 2.1 Chemical potential diagram for V-Si-N ternary system at 1473 K.

II. Diffusion and Reaction [2.2, 2.11]

The metallurgical thermodynamics is indeed a powerful theory for materials designing. However, to describe a phenomenon such as diffusion and reaction in detail solely with the metallurgical thermodynamics is difficult, because the concept to treat the "time" is missing. Therefore, such time-dependent phenomena requires to be discussed on the basis of the theory of the transportation phenomena in addition to the metallurgical thermodynamics.

A. Fick's Diffusion Theory

In order to simplify the consideration and description, a one-dimensional diffusion is treated in the following of this section. To extend the following description to two- or three-dimensional consideration, those parameters such as the position (x) and the diffusion flux (J)

are replaced respectively to the vector variants ***r*** and ***J***.

Consider a diffusion couple of an A–B binary system. The diffusion flux of the component A (J_A) is expressed on the basis of the Fick's First Law as

$$J_A = -D\frac{\partial C_A}{\partial x}, \tag{2.66}$$

where D is the diffusion coefficient, C_A is the composition of the component A, and x is the position. The diffusion coefficient is generally a function of the temperature, the pressure and the composition. In the next step, the change of the composition as a function of the time (t) is considered. The change of the composition in a small volume-element corresponds to the amount of the flux of the component A coming into the element subtracted by that going out of the element, when no consumption of the component A by reaction occurs in the element (the mass conservation law). Hence, the change of the composition is described as the function of the time as follows;

$$\frac{\partial C_A}{\partial t}\Delta x = J_A\Big|_{x(\text{incoming})} - J_A\Big|_{x+\Delta x(\text{outgoing})}. \tag{2.67}$$

Hence, the following equation is obtained by taking the limit of Δx to zero;

$$\frac{\partial C_A}{\partial t} = -\frac{\partial}{\partial x}J_A. \tag{2.68}$$

The combination of the equations (2.66) and (2.68) derives the following equation;

$$\frac{\partial C_A}{\partial t} = \frac{\partial}{\partial x}\left(D\frac{\partial C_A}{\partial x}\right). \tag{2.69}$$

When the diffusion coefficient can be assumed to be a constant, *i.e.*, being independent on the composition with isothermal and isobaric condition, the Fick's Second Law is deduced as

$$\frac{\partial C_A}{\partial t} = D\frac{\partial^2 C_A}{\partial x^2}. \tag{2.70}$$

The general solution of this formula is then put into consideration. A diffusion zone between two semi-infinite bodies in contact, whose

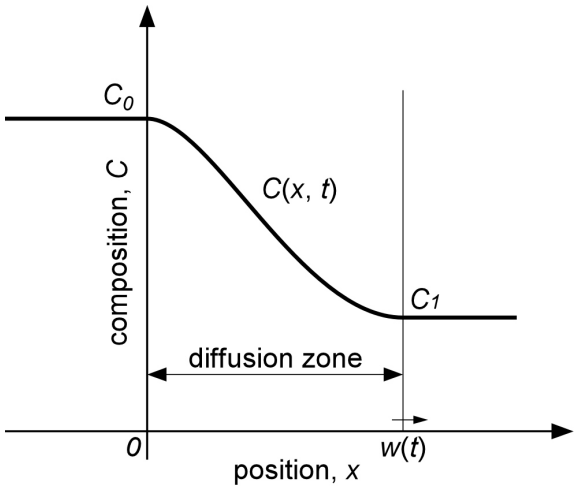

Fig. 2.2 A diffusion model with one moving boundary.

composition are respectively C_0 and C_1 is considered (see **Fig. 2.2**). Thus, the boundary conditions are defined as

$$x = 0,\ C = C_0 \quad \text{and} \quad x = w,\ C = C_1. \tag{2.71}$$

The formula (2.70) can be solved with the method of the combination of variables. A variable ψ is defined at first, which is dependent only on ξ as follows.

$$\psi = \frac{C - C_0}{C_1 - C_0}, \quad \xi = \frac{x}{w(t)}\ (0 \le \xi \le 1)\ . \tag{2.72}$$

Since $C = (C_1 - C_0)\ \psi + C_0$ is obtained from equation (2.72), each side of formula (2.70) is transformed as follows.

$$\frac{\partial C}{\partial t} = (C_1 - C_0)\frac{d\psi}{d\xi}\frac{\partial \xi}{\partial t} = -\frac{C_1 - C_0}{w}\frac{dw}{dt}\xi\frac{d\psi}{d\xi}\ , \tag{2.73}$$

$$\frac{\partial C}{\partial x} = (C_1 - C_0)\frac{d\psi}{d\xi}\frac{d\xi}{dx} = \frac{C_1 - C_0}{w}\frac{d\psi}{d\xi}\ , \tag{2.74}$$

$$\frac{\partial^2 C}{\partial x^2} = \frac{d}{d\xi}\frac{d\xi}{dx}\left(\frac{\partial C}{\partial x}\right) = \frac{C_1 - C_0}{w^2}\frac{d^2\psi}{d\xi^2}\ . \tag{2.75}$$

By substituting these equations for equation (2.70), the following formula is obtained.

$$-\frac{C_1 - C_0}{w}\frac{dw}{dt}\xi\frac{d\psi}{d\xi} = D\frac{C_1 - C_0}{w^2}\frac{d^2\psi}{d\xi^2}\ , \text{ hence,}$$

$$\frac{d^2\psi}{d\xi^2} + \left(\frac{w}{D}\frac{dw}{dt}\right)\xi\frac{d\psi}{d\xi} = 0\ . \tag{2.76}$$

The boundary conditions are also transformed respectively as

$$\xi = 0,\ \psi = 0 \quad \text{and} \quad \xi = 1,\ \psi = 1\ . \tag{2.77}$$

Since ψ is defined as a function dependent only on ξ, the factor $(w / D)(dw / dt)$ on the second term in equation (2.76) must be a constant. Therefore, it is stated as

$$\frac{w}{D}\frac{dw}{dt} = k_1\ \text{(constant)}\ . \tag{2.78}$$

With the initial condition of $w = 0$ at $t = 0$, the solution of equation (2.78) is deduced as

$$w = \sqrt{2k_1 Dt}\ . \tag{2.79}$$

This equation indicates that the thickness of the diffusion zone increases proportionately with the square root of the diffusion time. This result is called the parabolic law, which fits to most

of the growth behavior of reaction products in ceramic / metal interfaces. The substitution of equation (2.78) for equation (2.76), introducing a parameter $\zeta = d\psi / d\xi$, deduces

$$\frac{d\zeta}{d\xi} + k_1 \xi \zeta = 0 \text{ , hence, } \int \frac{d\zeta}{\zeta} = -k_1 \int \xi d\xi \text{ , therefore,}$$

$$\zeta = \frac{d\psi}{d\xi} = \exp\left(-\frac{k_1}{2} \xi^2 + k_2 \right) = k_2^* \exp\left(-\frac{k_1}{2} \xi^2 \right) , \tag{2.80}$$

where k_2 is an integration constant, and $k_2^* = \exp(k_2)$ is a constant, introduced to simplify the description. The solution of equation (2.80) is derived as

$$\psi = k_2^* \int_0^\xi \exp\left(-\frac{k_1}{2} \xi^2 \right) d\xi + k_3 , \tag{2.81}$$

where k_3 is an another integration constant. By substituting the boundary conditions (2.77), the values of k_2^* and k_3 are respectively obtained as

$$k_2^* = \frac{1}{\int_0^1 \exp\left(-\frac{k_1}{2} \xi^2 \right) d\xi} \text{ , and } k_3 = 0 . \tag{2.82}$$

Hence,

$$\psi = \frac{\int_0^\xi \exp\left(-\frac{k_1}{2} \xi^2 \right) d\xi}{\int_0^1 \exp\left(-\frac{k_1}{2} \xi^2 \right) d\xi} . \tag{2.83}$$

Introducing two parameters ι and η defined respectively as

$$\iota = \sqrt{\frac{k_1}{2}} \quad \text{and} \quad \eta^2 = \frac{k_1}{2} \xi^2 , \tag{2.84}$$

equation (2.83) can be transformed in a form utilizing the error function as

$$\psi = \frac{\int_0^\eta \exp\left(-\eta^2 \right) \frac{d\eta}{\iota}}{\int_0^\iota \exp\left(-\eta^2 \right) \frac{d\eta}{\iota}} = \frac{\frac{\sqrt{\pi}}{2\iota} \operatorname{erf}(\eta)}{\frac{\sqrt{\pi}}{2\iota} \operatorname{erf}(\iota)} = \frac{\operatorname{erf}(\iota \xi)}{\operatorname{erf}(\iota)} , \tag{2.85}$$

where the error function is described as

$$\operatorname{erf}(x) = \frac{2}{\sqrt{\pi}} \int_0^x \exp\left(-r^2 \right) dr . \tag{2.86}$$

Thus, the general solution for formula (2.70) is finally deduced as follows;

$$C(x,t) = (C_1 - C_0)\psi + C_0 = \frac{C_1 - C_0}{\mathrm{erf}(\iota)}\,\mathrm{erf}(\iota\xi) + C_0 = \alpha\,\mathrm{erf}\left(\frac{x}{2\sqrt{Dt}}\right) + \beta \ . \qquad (2.87)$$

where α and β are constants.

B. Transition State Theory for Chemical Reaction

Even if the metallurgical thermodynamics predicts that a reaction is allowed to occur with a large driving force, the reaction might not occur in some cases such as at very low temperatures. This phenomenon is explained on the basis of the transition state theory for chemical reaction. The theory takes into account a transition state with high potential between the reactant state and the product state of the reaction; the reactant substances require getting over this potential barrier with an amount of extra energy to reach the product state. Thus, a reaction of A, B and C (the reactant substances) to form P (the product), through the transition state M* (the activated complex) is considered as

$$\nu_A\mathrm{A} + \nu_B\mathrm{B} + \nu_C\mathrm{C} = \mathrm{M}^* \rightarrow \mathrm{P}\ , \qquad (2.88)$$

where the reactant substances is in equilibrium with the activated complex, while the reaction from the activated complex to the product is irreversible. The overall reaction rate of the reaction (2.88) is described as the multiplication of two factors; the composition of the activated complex, and the frequency of the reaction from the activated complex to the product. The former factor can be deduced on the basis of metallurgical thermodynamics. When the equilibrium between the reactant substances and the activated complex is achieved, the equilibrium constant (K^*) is described as follows. (See equations (2.22) and (2.28)).

$$K^* = \frac{C_{M^*}}{C_A^{\nu_A} C_B^{\nu_B} C_C^{\nu_C}} = \exp\left(-\frac{\Delta G^*}{RT}\right)\ , \qquad (2.89)$$

where C_{M^*}, C_A, C_B, and C_C are respectively the composition of M*, A, B, and C, and ΔG^* is the activation Gibbs energy. On the other hand, the latter factor is deduced on the basis of statistical thermodynamics as $\kappa_B T / h$, where κ_B is the Boltzmann constant and h is the Planck constant. Thus, the reaction rate (r) is described as

$$r = kC_A^{\nu_A} C_B^{\nu_B} C_C^{\nu_C} = \frac{\kappa_B T}{h} C_{M^*} = \frac{\kappa_B T}{h} C_A^{\nu_A} C_B^{\nu_B} C_C^{\nu_C} \exp\left(-\frac{\Delta G^*}{RT}\right)\ , \qquad (2.90)$$

where k is the reaction rate constant. Assuming that the activation enthalpy (ΔH^*) and the

activation entropy (ΔS^*) are independent on the temperature, the differentiation of the reaction rate constant by the temperature is derived as

$$\frac{dk}{dT} = \frac{e\kappa_B T}{h}\exp\left(\frac{\Delta S^*}{R}\right)\exp\left(-\frac{\Delta H^* + RT}{RT}\right)\left(\frac{\Delta H^* + RT}{RT^2}\right) . \tag{2.91}$$

This equation accords with the differentiation of Arrhenius-type function, $A = A_0 \exp(-E / RT)$, being described as

$$\frac{dA}{dT} = A_0 \exp\left(-\frac{E}{RT}\right)\left(\frac{E}{RT^2}\right) . \tag{2.92}$$

Hence, the reaction rate constant can be described as an Arrhenius-type function as follows;

$$k = k_0 \exp\left(-\frac{E}{RT}\right) , \quad k_0 = \frac{e\kappa_B T}{h}\exp\left(\frac{\Delta S^*}{R}\right) \text{ , and } \quad E = \Delta H^* + RT , \tag{2.93}$$

where k_0 and E are respectively the frequency factor and the apparent activation energy. Although k_0 and E are both functions of the temperature, they can be treated as constants when narrow range of the temperature is on consideration.

III. X-ray Diffraction (XRD) [2.12, 2.13]

When X-ray is irradiated to a substance, interaction phenomena such as coherent scatter, X-ray absorption and photoelectron emission occur between the X-ray and the substance. These phenomena are all useful for materials characterization as XRD, EXAFS / XANES and XPS, respectively. XRD, which can be operated in the ambient atmosphere, is the simplest technique to obtain the crystallographic information of a substance. Although to focus the X-ray in a narrow area of micrometer-scale is difficult, its performance to identify the existing phases in the substance from the crystallographic approach is indispensable for the analysis of materials structure. Furthermore, the cumulative database of diffraction patterns [2.14] enhances the capability of the technique.

A. Real Space and Reciprocal Space

Every inorganic or metallic substance in stable solid state is crystalline. Crystalline substances consist of crystals, whose constituent atoms are arranged periodically. The unit cell, whose base vectors are respectively $\boldsymbol{a}_1$, $\boldsymbol{a}_2$, and $\boldsymbol{a}_3$, is defined as the minimum volume of

the crystal, in which no symmetry element [2.15] of the periodical arrangement of the atoms is lost. Relative directions to the unit cell are described with these base vectors as

$$[u\ v\ w] = u\boldsymbol{a}_1 + v\boldsymbol{a}_2 + w\boldsymbol{a}_3 \,. \tag{2.94}$$

These base vectors $\boldsymbol{a}_1$, $\boldsymbol{a}_2$, and $\boldsymbol{a}_3$ are defined in the real space. On the other hand, the reciprocal space is described with the base vectors $\boldsymbol{a}_1^*$, $\boldsymbol{a}_2^*$ and $\boldsymbol{a}_3^*$ defined as follows;

$$\boldsymbol{a}_1^* = \frac{\boldsymbol{a}_2 \times \boldsymbol{a}_3}{\boldsymbol{a}_1 \cdot (\boldsymbol{a}_2 \times \boldsymbol{a}_3)} \,, \quad \boldsymbol{a}_2^* = \frac{\boldsymbol{a}_3 \times \boldsymbol{a}_1}{\boldsymbol{a}_2 \cdot (\boldsymbol{a}_3 \times \boldsymbol{a}_1)} \,, \quad \boldsymbol{a}_3^* = \frac{\boldsymbol{a}_1 \times \boldsymbol{a}_2}{\boldsymbol{a}_3 \cdot (\boldsymbol{a}_1 \times \boldsymbol{a}_2)} \,. \tag{2.95}$$

A reciprocal vector

$$\boldsymbol{r}^* = h\boldsymbol{a}_1^* + k\boldsymbol{a}_2^* + l\boldsymbol{a}_3^* \tag{2.96}$$

defines a plane in the real space: the direction of the reciprocal vector indicates the normal direction of the (h k l) plane in the real space, and the length of the reciprocal vector ($|\boldsymbol{r}^*|$) equals to d_{hkl}^{-1}, where d_{hkl} is the interplanar spacing of the (h k l) plane. The parameters h, k, and l defining the crystallographic plane are called the Miller indices. It is a very important point that a plane in crystallography is not defined by its position as a single plane, but by its normal direction and interplanar spacing of planes stacking one another. The values of h, k, and l must be integers, otherwise the definition of the unit cell is wrong. Therefore, only the points with integer coordinates have a meaning in the reciprocal space.

B. Bragg's Condition for Diffraction

The superposition of X-ray coherently scattered by atoms in a crystal is intensified at some specific relation of the angles between the incident and the scattered X-ray. This phenomenon is called diffraction. Diffraction occurs when the difference of the optical path (δ) between the X-ray coherently scattered by each two atoms in a crystal is the same to the wavelength of the X-ray (λ), *i.e.*, when the phase of the X-ray scattered by different atoms harmonizes. **Fig. 2.3** shows a schematic illustration of the optical path of the X-ray scattered by two atoms at O and A in different stack of the (h k l) plane. $\boldsymbol{s}_0$ and $\boldsymbol{s}_1$ in the figure are respectively the unit vectors

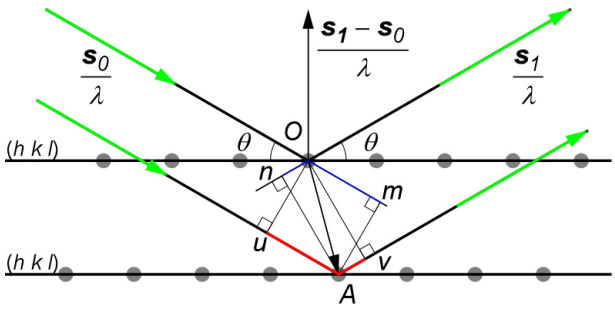

Fig. 2.3 Schematic illustration of diffraction.

indicating the incident and the scattered direction of the X-ray. The difference of the optical path of the X-ray is described as

$$\delta = \overline{uA} + \overline{Av} = \overline{Om} + \overline{nO} = \overrightarrow{OA} \cdot \boldsymbol{s}_0 + \overrightarrow{OA} \cdot (-\boldsymbol{s}_1) = -\overrightarrow{OA} \cdot (\boldsymbol{s}_1 - \boldsymbol{s}_0) \ . \tag{2.97}$$

Thus, the difference of the phase ($\Delta\phi$) of the X-ray is described as

$$\Delta\phi = 2\pi \frac{\delta}{\lambda} = -2\pi \left(\frac{\boldsymbol{s}_1 - \boldsymbol{s}_0}{\lambda} \right) \cdot \overrightarrow{OA} \ . \tag{2.98}$$

The vector $(\boldsymbol{s}_1 - \boldsymbol{s}_0) / \lambda$ is called the scatter vector. It directs to the normal of the (h k l) plane. Therefore, it is described using the reciprocal base vectors as

$$\frac{\boldsymbol{s}_1 - \boldsymbol{s}_0}{\lambda} = x\left(h\boldsymbol{a}_1^* + k\boldsymbol{a}_2^* + l\boldsymbol{a}_3^* \right) . \tag{2.99}$$

On the other hand, the relative positions of atoms are described using real base vectors as

$$\overrightarrow{OA} = p\boldsymbol{a}_1 + q\boldsymbol{a}_2 + r\boldsymbol{a}_3 \ , \tag{2.100}$$

where p, q, and r can be selected to be integers. Thus, the substitution of equations (2.99) and (2.100) for equation (2.98) deduces

$$\Delta\phi = -2\pi x\left(h\boldsymbol{a}_1^* + k\boldsymbol{a}_2^* + l\boldsymbol{a}_3^* \right) \cdot \left(p\boldsymbol{a}_1 + q\boldsymbol{a}_2 + r\boldsymbol{a}_3 \right) = -2\pi x\left(hp + kq + lr \right) . \tag{2.101}$$

As described above, diffraction occurs when $\Delta\phi$ equals to integral multiples of 2π. Since h, k, l, p, q, and r are all integers, the condition to occur the diffraction is x to be an integer, for which generally 1 is substituted. Therefore, the condition of diffraction is derived as

$$\frac{\boldsymbol{s}_1 - \boldsymbol{s}_0}{\lambda} = \boldsymbol{r}^* = h\boldsymbol{a}_1^* + k\boldsymbol{a}_2^* + l\boldsymbol{a}_3^* \ . \tag{2.102}$$

This condition indicates that diffraction occurs when the scatter vector corresponds to the reciprocal lattice points. Thus, in order to consider every possible diffraction of a incident X-ray ($\boldsymbol{s}_0/\lambda$) by a crystal corresponds to consider a sphere with its radius being $1/\lambda$ in the reciprocal space of the crystal, as shown in **Fig. 2.4**. This sphere is called the Ewald's sphere.

Consequently, the size of the vectors on both sides of the equation (2.102) is considered.

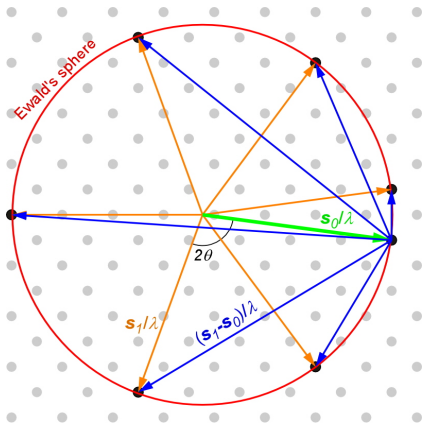

Fig. 2.4 The condition of diffraction schematically drawn on two-dimensional reciprocal space.

Since $\boldsymbol{s}_0$ and $\boldsymbol{s}_1$ are unit vectors, the following relation is derived (see Fig. 2.3):

$$\left|\boldsymbol{s}_1 - \boldsymbol{s}_0\right| = 2\sin\theta \ . \tag{2.103}$$

On the other hand, the (*h k l*) reciprocal vector establishes the following relation with the interplanar distance of the (*h k l*) plane.

$$\left|\boldsymbol{r}^*\right| = \left|h\boldsymbol{a}_1^* + k\boldsymbol{a}_2^* + l\boldsymbol{a}_3^*\right| = \frac{1}{d_{hkl}} \ . \tag{2.104}$$

Thus, the Bragg's condition, which relates the wavelength of the X-ray, the diffraction angle, and the interplanar distance of the (*h k l*) plane, is deduced as

$$\frac{\left|\boldsymbol{s}_1 - \boldsymbol{s}_0\right|}{\lambda} = \frac{2\sin\theta}{\lambda} = \left|h\boldsymbol{a}_1^* + k\boldsymbol{a}_2^* + l\boldsymbol{a}_3^*\right| = \frac{1}{d_{hkl}} \ , \quad \text{hence,} \quad \lambda = 2d_{hkl}\sin\theta \ . \tag{2.105}$$

C. Diffraction Intensity

Diffraction occurs by superposition of coherently scattered X-rays by atoms in a crystal. Such scattering of X-ray occurs only by the interaction with electrons in the atom, while the interaction with the core, the Compton scattering, no longer keeps the coherency of the X-ray. Therefore, the atomic scatter factor (*f*), the possibility to scatter the X-ray to a certain direction by an atom, is described as

$$f(\boldsymbol{s}) = \int_{\text{atom}} \rho(\boldsymbol{r}) \exp(2\pi i\, \boldsymbol{s}\cdot\boldsymbol{r}) d\tau \ , \tag{2.106}$$

where $\boldsymbol{r}$ is the position in the atom, ρ is the density of electron, $\boldsymbol{s}$ is the scatter vector, and τ is the volume element. In consequence, the possibility to scatter the X-ray to a certain direction by a crystal is described as

$$c(\boldsymbol{s}) = \int_{\text{crystal}} \rho(\boldsymbol{R}) \exp(2\pi i\, \boldsymbol{s}\cdot\boldsymbol{R}) d\tau \ , \tag{2.107}$$

where $\boldsymbol{R}$ is the position in the crystal. Since the unit cells in the crystal are all equivalent, equation (2.107) can be transformed using the position of the original point of the unit cell in the crystal ($\boldsymbol{r}_i$), the position of the atom in the unit cell ($\boldsymbol{r}_j$), and the position in the atom ($\boldsymbol{r}$) as

$$\begin{aligned} c(\boldsymbol{s}) &= \int_{\text{crystal}} \rho(r_i + r_j + r) \exp\{2\pi i\, \boldsymbol{s}\cdot(r_i + r_j + r)\} d\tau \\ &= \sum_i \int_{\text{unit cell}} \rho(r_j + r) \exp\{2\pi i\, \boldsymbol{s}\cdot(r_i + r_j + r)\} d\tau \\ &= \sum_i \exp(2\pi i\, \boldsymbol{s}\cdot r_i) \times \int_{\text{unit cell}} \rho(r_j + r) \exp\{2\pi i\, \boldsymbol{s}\cdot(r_j + r)\} d\tau \\ &= \sum_i \exp(2\pi i\, \boldsymbol{s}\cdot r_i) \times \sum_j \exp(2\pi i\, \boldsymbol{s}\cdot r_j) \int_{\text{atom}} \rho(r) \exp(2\pi i\, \boldsymbol{s}\cdot r) d\tau \end{aligned}$$

$$= \sum_i \exp(2\pi i\, \boldsymbol{s} \cdot r_i) \times \sum_j f_j(\boldsymbol{s}) \exp(2\pi i\, \boldsymbol{s} \cdot r_j)$$

$$= G(\boldsymbol{s}) \times F(\boldsymbol{s}) \ . \tag{2.108}$$

$G(\boldsymbol{s})$ is related to the Laue function $|G(\boldsymbol{s})|^2$. The Laue function describes the intensity of the scattered X-ray in relation with the size of the crystal and the scatter vector. It takes its maximum value at the condition of diffraction (2.102). $F(\boldsymbol{s})$ is the structure factor, which describes the scatter by a unit cell. The intensity of the scattered X-ray (I) is described as

$$I = |G(\boldsymbol{s})|^2 \, |F(\boldsymbol{s})|^2 \ . \tag{2.109}$$

However, the measured intensity of the scattered X-ray appears different from the value derived from equation (2.109). The following four correction factors must be considered.

(i) The Lorentz-polarization factor (LP)

The polarization factor is deduced from the equation of Thomson scatter, which describes the intensity of the scattered X-ray by an electron. For an X-ray diffractometer with the optical geometry in which the monochrometer is located on the path of the scattered X-ray, the polarization factor (P) is described as

$$P = \frac{1 + \cos^2 2\theta_{ss} \cos^2 2\theta}{2} \ . \tag{2.110}$$

where θ_{ss} is the open angle of the scatter slit.

The Lorentz factor corresponds to the deviation of scatter intensity caused by the angular dispersion of the incident and the scattered X-ray. The Lorentz factor (L) is described as $L = (\sin^2\theta \cos\theta)^{-1}$. These factors are generally combined, and treated as the Lorentz-polarization factor as

$$LP = \frac{1 + \cos^2 2\theta_{ss} \cos^2 2\theta}{2(\sin^2 \theta \cos\theta)} \ . \tag{2.111}$$

(ii) The multiplication factor (p)

The multiplication factor corresponds to the number of equivalent planes of each ($h\ k\ l$) plane. This factor multiplies the probability to orientate the $\{h\ k\ l\}$ planes to the measurement direction in randomly oriented powder specimens.

(iii) The absorption factor (A)

The intensity of the X-ray penetrating a substance is reduced by incoherent interaction

between the X-ray and the substance. This phenomenon is called absorption. The reduction rate of the intensity is in proportion with the path-length of the X-ray in the substance. Hence, the intensity of the X-ray (I) in the substance at the path-length l is described as

$$-dI = \mu I dl \ , \quad I = I_0 \exp(-\mu l) \ . \tag{2.112}$$

where μ is the linear absorption coefficient, and I_0 is the intensity of the incident X-ray. Taking into account that only the (h k l) planes parallel to the surface-plane of the specimen are measured with the 2θ–θ diffractometry, the X-ray scattered by a small volume element dx at depth x and measured out of the surface of the specimen is described as

$$dI = I_1 \frac{dx}{\sin\theta} \exp\left(-\frac{2\mu x}{\sin\theta}\right) \ . \tag{2.113}$$

where I_1 is the intensity of the scattered X-ray at the surface of the specimen, *i.e.*, $x = 0$. Thus, the intensity of the scattered X-ray by a specimen with thickness (w) is described as

$$I = \frac{I_1}{\sin\theta} \int_0^w \exp\left(-\frac{2\mu x}{\sin\theta}\right) dx = \frac{I_1}{2\mu} \left\{1 - \exp\left(-\frac{2\mu w}{\sin\theta}\right)\right\} \ . \tag{2.114}$$

Therefore, the absorption factor is described as

$$A = \frac{1}{2\mu} \left\{1 - \exp\left(-\frac{2\mu w}{\sin\theta}\right)\right\} \ . \tag{2.115}$$

(iv) The Debye-Waller factor (DW)

The Debye-Waller factor corresponds to the uncertainty of the position of the atoms in the crystal, originated by the thermal vibration of the atoms. The factor corrects the atomic scatter factor in the following form;

$$f_{\text{actual}} = f \exp(-M) \ , \tag{2.116}$$

where the value of M is obtained experimentally. Therefore, the intensity of the scattered X-ray is corrected with $\exp(-2M)$.

Taking into account all these correction factors, the general formula to describe the intensity of the scattered X-ray measured with a diffractometer is deduced as

$$I = |G(\boldsymbol{s})|^2 |F(\boldsymbol{s})|^2 \frac{1 + \cos^2 2\theta_{ss} \cos^2 2\theta}{2(\sin^2\theta \cos\theta)} p \frac{1}{2\mu} \left\{1 - \exp\left(-\frac{2\mu w}{\sin\theta}\right)\right\} \exp(-2M) \ . \tag{2.117}$$

IV. Electron Probe Microanalysis (EPMA) [2.16, 2.17]

EPMA is one of the most important technique for microstructure analysis of a substance, because of its performance to detect constituent and impurity elements quantitatively within a local (micrometer-scale) area of the substance. A focused electron beam irradiated to the surface of a substance induces such interaction with the substance as the emission of the characteristic X-rays, the continuous X-rays, the secondary electrons, the back-scattered electrons, and the Auger electrons. EPMA analyzes the wavelength (*i.e.*, the photon-energy) and the intensity of the characteristic X-rays. There are two methods to analyze the X-rays. One is the wavelength-dispersive spectrometry (WDS), and the other method is the energy-dispersive spectrometry (EDS).

A. WDS and EDS

WDS utilizes the X-ray diffraction of the dispersive crystals, whose interplanar spacing is known, to detect the characteristic X-rays emitted from the specimen. **Fig. 2.5** shows the geometry of a wavelength dispersive spectrometer. The dispersive crystal moves on the line of the take-out angle of the characteristic X-ray, synchronized by the movement of the scintillation counter, keeping the Rowland radius (R) to be a constant. Regarding to the geometry, the distance between the analyzing point of the specimen and the dispersive crystal (L) is expressed as

$$L = 2R \sin\theta . \qquad (2.118)$$

Substitution of the Bragg's condition (2.105) for equation (2.118) derives

$$L = (R / d)\,\lambda , \qquad (2.119)$$

where d is the interplanar spacing of the dispersive crystal. Therefore, the detection of the characteristic X-rays can be implemented by moving the dispersive crystal. In addition, the analysis using a dispersive crystal with lower value of d, which makes L longer, results in higher resolution of the wavelength.

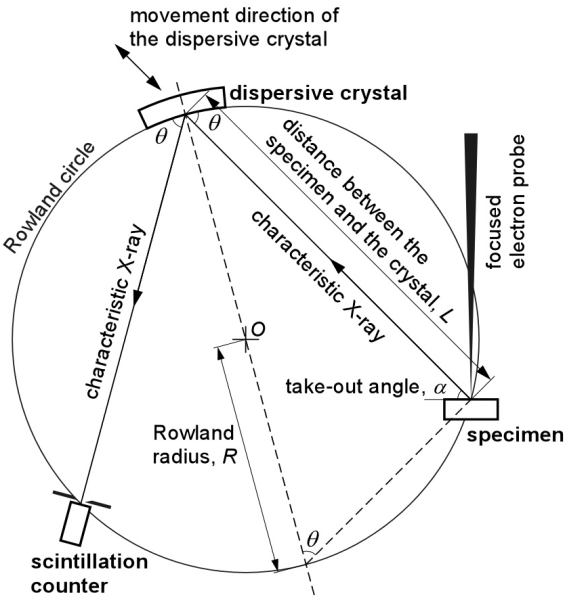

Fig. 2.5 Geometry of wavelength dispersive spectrometer.

Table 2.3 shows a list of representative dispersive crystals used in WDS-EPMA.

Table 2.3 A list of representative dispersive crystals used in WDS-EPMA.

Crystal designation	Crystal name	Miller indices, *h k l*	Interplaner spacing, *2d* / Å
CER	Lead Cerotate	(film)	133
STE	Lead Stearate	(film)	100.4
MYR	Lead Myristate	(film)	80.0
LDE1	Layered Dispersion Element 1	(multilayer)	60 ± 1
RAP	Rubidium Acid Phthalate	1 0 0	26.121
TAP	Thallium Acid Phthalate	1 0 0	25.757
PET	Pentaerythritol	0 0 2	8.742
LIF	Lithium Fluoride	2 0 0	4.0267

EDS directly detects the photon-energy and its intensity with a lithium-doped silicon semiconductor sensing device. An X-ray photon entered in the device excites the electrons in the device and generates a pulse signal. The pulse-height of the signal corresponds proportionately to the energy of the X-ray photon. Thus, the photon-energy spectrum of the X-ray can be obtained.

The difference in the dispersion method of the X-ray results in the difference in the performance between WDS and EDS. The energy resolution of WDS is higher more than 10 times than EDS. **Fig. 2.6** shows a comparison of X-ray spectrum of AlGaAs between WDS (TAP dispersive crystal) and EDS [2.18]. The conventional Si(Li) EDS cannot divide Ga Lα from Ga Lβ and As Lα from As Lβ, while WDS divides them clearly. The energy resolution is one of the fatal performance, especially when the characteristic X-rays of some elements in the specimen have very close photon-energies. Recently, a new EDS, which is called micro-calorimetry EDS and has a comparable energy resolution to WDS, has been invented [2.19]. It needs a low temperature of 0.1 K or lower,

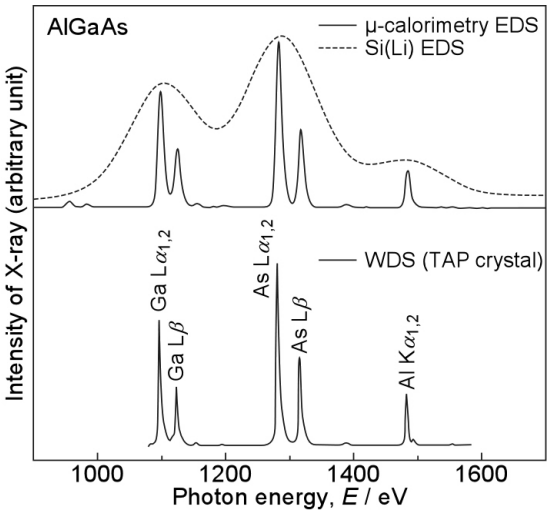

Fig. 2.6 X-ray spectrum of AlGaAs taken by WDS and EDS [2.18].

however, a further development is required for conventional use. On the other hand, WDS is not suitable for analysis of wide area with low magnification probe-scan and of rough surfaces such as fractured surfaces, due to its high sensitivity to the optical geometry shown in Fig. 2.5. EDS matches for such analyses. In addition, EDS requires very short time for qualitative element detection and low electron dose-rate compared to WDS.

B. Spatial Resolution of EPMA

The spatial resolution of EPMA is lower than that of secondary electron images or back-scattered electron images of scanning electron microscopes. The electrons irradiated to a substance displace inner-shell electrons of the constituent atoms to be in an excited state. These atoms immediately back to the basal state by filling the vacant electron-orbits with outer-shell electrons emitting the characteristic X-rays corresponding to the difference of the energy between the inner and outer electron orbits. On the other hand, the irradiated electrons are scattered, spreading in the substance and losing its energy. These energetic electrons continue to displace electrons in the substance until its energy is reduced below the critical energy for exciting the constituent atoms. **Fig. 2.7** shows a Monte Carlo simulation of 15 keV-electrons scattering in bulk Si_3N_4. The diameter of the area emitting the characteristic X-ray is predicted to be 2.2 μm. Even though the electron probe is focused on a considerably narrow area, the electrons scattered in the substance will spread the emitting area of characteristic X-rays.

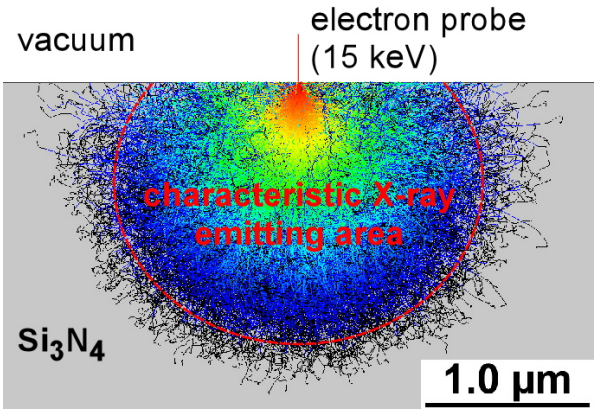

Fig. 2.7 Monte Carlo simulation of the track and energy-loss of 15 keV-electrons irradiated into bulk Si_3N_4.

C. Quantitative Composition Analysis and ZAF Correction

EPMA compares the intensity of the characteristic X-rays of the specimens with that of standard substances, whose composition is known, for the analysis of the composition of the

specimens. The intensity of the characteristic X-ray of an element, measured from the specimen, fundamentally corresponds proportionately to the mass fraction of the element. Therefore, the mass fraction of the element A (C_A) in the specimen is described as

$$\frac{C_A}{C_A^0} = \frac{I_A}{I_A^0} = K_A \ , \tag{2.120}$$

where $C_A^{\,0}$ and $I_A^{\,0}$ are the mass fraction and the intensity of the characteristic X-ray of the element A for the standard substance, I_A is the characteristic X-ray for the specimen, and K_A is the intensity ratio of the characteristic X-ray between the standard substance and the specimen. To use a pure substance as the standard makes the intensity ratio indicate directly the mass fraction of the element, *i.e.*, $C_A^{\,0} = 1$, $C_A = K_A$. Thus, pure substances are used as standards for the composition analysis with the EPMA. However, the actual composition of the specimen does not follow the equation (2.120). The following three effects, which affect the intensity of the characteristic X-ray, must be taken into account to obtain the actual composition of each element:

(i) the effect of atomic number (Ξ_Z)

The penetration depth and scatter behavior of the probe electrons depends on their incident energy, constituent elements of the specimen and their composition. Therefore, the efficiency of characteristic X-ray emission per one electron is different between the specimen and the standard substance. The correction factor for this effect is given by P. Dumcumb and S. J. B. Reed with the following formula;

$$\Xi_Z = \frac{R_0}{R_S}\frac{S_S}{S_0} \ , \tag{2.121}$$

where R and S are respectively the back-scattering factor and the stopping power. The subscripts 0 and S on the parameters indicate respectively the standard substance and the specimen. The value of R is given as a function of the atomic number and the over-voltage ratio (E_K / E_0), where E_0 is the kinetic energy of the incident electrons and E_K is the critical energy for exciting an atom [2.16]. The value of S is obtained with the following formula;

$$S = \frac{Z}{A}\ln\left(0.583\left(\frac{E_0 + E_K}{E_I}\right)\right) \ , \tag{2.122}$$

where Z, A, and E_I are respectively the average atomic mass of the specimen, the average

atomic number of the specimen, and the ionization energy of the element [2.16].

(ii) the effect of absorption (Ξ_A)

Not all of the characteristic X-ray generated in the specimen is emitted out of the surface, but a part of the X-ray is absorbed by the specimen. The absorption fraction varies with the constituent elements of the specimen and their composition. Thus, the absorption fraction of the characteristic X-ray becomes different between the specimen and the standard substance. The correction factor for this effect is given by J. Philibert as;

$$\Xi_A = \frac{f_0}{f_S} \ , \quad f = \frac{1+\frac{1.2A}{Z^2}}{\left(1+\frac{\chi}{\sigma}\right)\left\{1+\frac{1.2A}{Z^2}\left(1+\frac{\chi}{\sigma}\right)\right\}} \ , \quad \chi = \frac{\mu}{\rho}\mathrm{cosec}\,\alpha \ , \tag{2.123}$$

where f is the Philibert's absorption correction function, χ is the mass absorption parameter, σ is the Lenard's coefficient, μ is the linear absorption coefficient, ρ is the mass density, and α is the take-out angle of the characteristic X-ray. The Lenard's coefficient is a constant determined by the accelerating voltage of the electron probe, being 5900 for 15 keV electrons [2.16]. (μ / ρ) is a constant characteristic to the substance and called the mass absorption coefficient, which is independent on the state (solid, liquid, gas) of the substance [2.16].

(iii) the effect of fluorescence (Ξ_F)

The atoms in the specimen are excited to emit characteristic X-rays not only by the probe electrons, but also by the characteristic and continuous X-rays emitted by other elements in the specimen. Thus, the intensity of the fluorescence-induced characteristic X-ray of an element is different between the specimen and the standard substance. Considering an A-B binary specimen in which the characteristic X-ray originated from the B element excites the A atoms, the correction factor for this effect is given by S. J. B. Reed as;

$$\Xi_F = \frac{1}{1+I_F/I_D} \ , \quad \frac{I_F}{I_D} = C_B J_A D \frac{(\mu/\rho)_A^B}{(\mu/\rho)_S^B}\left(g(x)+g(y)\right) \ , \tag{2.124}$$

where I_F / I_D is the intensity ratio of the fluorescence-induced and electron-irradiation-induced characteristic X-rays, C_B is the mass fraction of B element in the specimen, J_A and D are the correction constants for fluorescence excitation, $(\mu/\rho)_A^B$ is the mass absorption coefficient of element A for the characteristic X-ray of the element B, $(\mu/\rho)_S^B$ is the average mass absorption coefficient of the specimen for the characteristic X-ray of the element B, and $g(x)$

and $g(y)$ are the correction parameters respectively related to the X-ray absorption and the probe-electron penetration. The value of J_A is determined by the A element, being 0.020, 0.102, 0.115, and 0.018 respectively for Si, Ti, V, and Nb [2.16]. The value of D is obtained from a graph, which relates D to the difference in the atomic number ($Z_B - Z_A$) and the accelerating voltage of the electron probe [2.16]. The correction parameters $g(x)$ and $g(y)$ are described as

$$g(\xi) = \frac{\ln(1+\xi)}{\xi} \quad , \quad x = \frac{(\mu/\rho)_S^A}{(\mu/\rho)_S^B} \operatorname{cosec}\alpha \quad , \quad y = \frac{4.5\times10^5}{E_0^{1.65} - E_{K(A)}^{1.65}} \frac{1}{(\mu/\rho)_S^B} \quad , \tag{2.125}$$

where ξ is replaced by x or y.

These three effects are put together and called the ZAF effect. The ZAF correction coefficient (Ξ) is described as

$$\Xi = \Xi_Z \Xi_A \Xi_F = \frac{f_0}{f_S}\left(\frac{R_0}{R_S}\frac{S_S}{S_0}\right)\frac{1}{1+I_F/I_D} \quad . \tag{2.126}$$

Thus, the mass fraction of the element A in the specimen is described as

$$C_A = K_A \Xi \, . \tag{2.127}$$

As shown in the last paragraph, the ZAF correction coefficient requires the composition value of each element, which is unknown, for the calculation of the average values of A, Z, and (μ / ρ) of the specimen, and the calculation of I_F / I_D. Thus, equation (2.120) is used for the first approximation of the composition. Then, regressive calculation of the ZAF correction coefficient is made until the composition of each element converges to a certain value.

References

[2.1] O. Kubaschewski, C.B. Alcock, P.J. Spencer: *Materials Thermochemistry*, 6th Edition, Pergamon Press, Oxford (England), 1993, pp. 1-63.

[2.2] *Metallurgical Physical Chemistry*, The Japan Institute of Metals, Sendai (Japan), 1988, pp. 23-114, in Japanese.

[2.3] Z. Morita: *Basis of Solution Thermodynamics*, Textbook for lecture of Materials Thermodynamics, private printing, in Japanese.

[2.4] O. Kubaschewski, C.B. Alcock, P.J. Spencer: *Materials Thermochemistry*, 6th Edition, Pergamon Press, Oxford (England), 1993, pp. 257-323.

[2.5] *Binary Alloy Phase Diagrams*, Thaddeus B. Massalski (editor-in-chief), American Society for Metals, Metals Park, Ohio (USA), 1986.

[2.6] *Handbook of Ternary Alloy Phase Diagrams*, P. Villars, A. Prince, and H. Okamoto (eds.), ASM International, Materials Park, Ohio (USA), 1995.

[2.7] *Phase Diagrams of Ternary Boron Nitride and Silicon Nitride Systems*, P. Rogl and J.C. Schuster (eds.), ASM International, Materials Park, Ohio (USA), 1992.

[2.8] *Phase Diagrams of Ternary Boron Nitride and Silicon Nitride Systems*, P. Rogl and J.C. Schuster (eds.), ASM International, Materials Park, Ohio (USA), 1992, pp. 205-207.

[2.9] *Binary Alloy Phase Diagrams*, Thaddeus B. Massalski (editor-in-chief), American Society for Metals, Metals Park, Ohio (USA), 1986, pp. 2060-2062.

[2.10] *Binary Alloy Phase Diagrams*, Thaddeus B. Massalski (editor-in-chief), American Society for Metals, Metals Park, Ohio (USA), 1986, pp. 1656-1659.

[2.11] T. Mizushina and F. Ogino: Transportation Phenomena, Sangyo Tosho, Tokyo (Japan), 1981, in Japanese.

[2.12] B.D. Cullity: *Elements of X-ray Diffraction*, Second Edition, Addison-Wesley, Massachusetts (USA), Translated by G. Matsumura, Agne, Tokyo (Japan), 1980, in Japanese.

[2.13] Y. Waseda and E. Matsubara: *Structure Analysis by X-ray –Determination of Atomic Arrangement–*, Uchida Rokakuho, Tokyo (Japan), 1998, in Japanese.

[2.14] *Powder Diffraction Files*, JCPDS–International Centre for Diffraction Data, Newtown Square, Pennsylvania (USA).

[2.15] *International Tables for Crystallography*, Volume A, Fourth edition, Th. Hahn (ed.), Kluwer, Dordrecht (The Netherlands), 1995.

[2.16] H. Soezima: *Electron-Beam Microanalysis*, Nikkan Kogyo Newspapers, Tokyo (Japan), 1987, in Japanese.

[2.17] *Electron Probe Microanalizer*, The Surface Science Society of Japan (ed.), Maruzen, Tokyo (Japan), 1998, in Japanese.

[2.18] Z. Horita: *Materia Japan*, 2000, Vol. 39, pp. 199, in Japanese.

[2.19] D.A. Wollman, K.D. Irvin, G.C. Hilton, L.L. Dulcie, D.E. Newbury and J.M. Martinis: *J. Microscopy*, 1997, Vol. 188, pp. 196-223.

Chapter 3 Experimental Procedure

This chapter describes the experimental procedure which is commonly employed in the present study. Processes of materials preparation, diffusion bonding facility and its operating conditions, analysis and test conditions are described in detail.

I. Materials and Their Preparation

A. Silicon Nitride

Si_3N_4 specimens were prepared from pressureless sintered columnar rods (manufactured by Kyocera Corporation with the product code SN-220), whose diameter and length measured respectively 6.0 mm and 40.0 mm. They contained a few mass percentages of alumina (Al_2O_3), yttria (Y_2O_3) and tungsten di-silicide (WSi_2) as the sintering agents.

The rods were cut to a length of 4.1 mm with a wet type diamond-composed grinding wheel. One side of the cut surfaces was flattened with the 220 mesh and 30 μm diamond-embedded grinding discs and polished with the 15 μm and 3.0 μm diamond-paste-spread polishing clothes. The roughness of the obtained surface was approximately 0.032 μm. This smoothed-side of the surfaces was applied to the diffusion bonding as the bonding surface. The other side of the surfaces was ground with the 220 mesh diamond-embedded grinding discs to make it flat and parallel to the bonding surface. Then, the specimens were cleaned using an ultrasonic bath with acetone and immediately dried with a cold blower.

B. Insert Foils of Active Metals

The foils of titanium, vanadium and niobium (purchased from The Nilaco Corporation) were used as the insert in the present study. The thickness and the nominal purity of the foils

used in the present study are listed in **Table 3.1**.

The foils of the metals were cut to square pieces of 6.5 mm each side, with a pair of metal-cutting scissors. Both sides of the metal foils were polished just before the bonding treatment with a 0.3 μm alumina-water-suspension spread polishing cloth, in order to remove oxide scales on their surfaces and to minimize the surface contamination. The roughness of the surface of the foils varied from 0.10 μm to 0.20 μm, depending on the material. The specimens were then cleaned using an ultrasonic bath with acetone and immediately dried with a cold blower.

Table 3.1 A list of the insert foils used in the present study.

Material	Thickness, w_0 / μm	Nominal purity, C_0 (%)
Titanium (Ti)	20	99.5
	50	99.5
	150	99.5
Vanadium (V)	25	99.9
Niobium (Nb)	25.4	99.9
	100	99.9

Some of the titanium specimens were pre-solved with nitrogen. The nitrogen solution treatment was implemented in the following procedure. The titanium specimens were prepared with the ordinary process described in the previous paragraph. The specimens were set in quartz capsules, inside which were shielded with alumina crucibles to avoid the reaction between titanium and quartz. The capsules were evacuated to a background pressure below 1×10^{-3} Pa and then filled with high-purity (99.999 %) nitrogen gas. Then, the capsules were sealed using a propane-oxygen flame torch. The sealed capsules were put into a conventional muffle furnace for heat treatment at 1173 K for 86.4 ks. The composition of nitrogen in the pre-treated titanium foils were controlled by changing the pressure of nitrogen filled in the capsule. The process is schematically illustrated on **Fig. 3.1**.

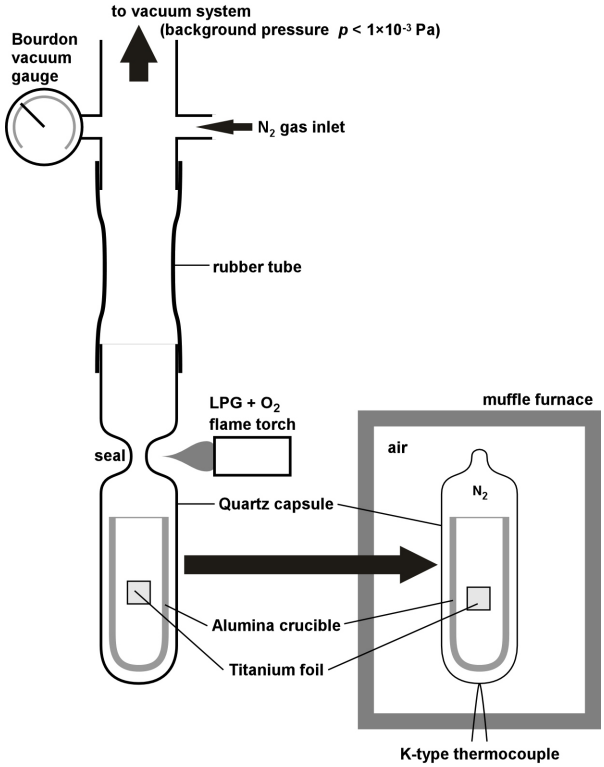

Fig. 3.1 Schematic illustration of the nitrogen pre-solution treatment process of titanium foils.

Some of the niobium specimens were

Table 3.2 Condition parameters for niobium deposition on silicon nitride.

Condition parameters	Substrate-cleaning	Deposition
Background vacuum pressure, p / Pa	1.7×10^{-5}	1.7×10^{-5}
Ar atmosphere, p_{Ar} / Pa	5.0	0.80
Frequency of output, f / MHz	13.56	13.56
Power output, P_F / W	210	410
Reflection, P_R / W	< 5	10
Operation time, t / s	300	4920

directly deposited on the bonding surface of the silicon nitride specimens by radio-frequency magnetron sputter deposition technique. The nominal purity of the niobium target (manufactured by Furuuchi Chemical) was 99.9 %. The silicon nitride substrates were cleaned by argon ion bombardment at first. Then, the deposition of niobium was implemented. The condition parameters for the deposition are listed on **Table 3.2**.

Single crystal specimens of niobium (purchased from The Nilaco Corporation) were also used in the present study. A columnar rod of niobium single crystal (12 mm in diameter and 50 mm in length), whose column axis is oriented to [*1 0 0*] direction of the crystal, was sliced to a thickness of 0.5 mm perpendicular to the column axis using a wire discharge cutting machine. The heat affected zone formed on both sides of the surface was first removed with a 800 mesh emery paper. Then, the thickness of the specimens was reduced to approximately 100 μm with 1000 mesh and 1500 mesh emery papers. Both sides of the specimens were polished with a 0.3 μm alumina-water-suspension spread polishing cloth. Finally, specimens were cleaned using an ultrasonic bath with acetone and immediately dried with a cold blower.

II. Diffusion Bonding Apparatus and Bonding Conditions

Two silicon nitride specimens and a metal foil were used for each bonding experiment. The metal foil was inserted between two Si_3N_4 specimens, as illustrated schematically in **Fig. 3.2**. Then, they were set in a furnace for the diffusion bonding treatment.

A. Diffusion Bonding Furnace

Fig 3.3 shows a schematic illustration of the diffusion bonding furnace used in the present study. It consisted of a water-cooled vacuum chamber, a pair of hydraulic pushing rods, an oil-diffusion evacuation pump system, a radio-frequency power source, an induction coil, a heating element made of graphite, a thermometer, a pair of extension rods and thermal insulation plates. The specimens were set between two extension rods made of silicon carbide. The furnace heated the specimen by infrared radiation of the graphite heating element, which was primarily heated by the induction coil conducting a high-frequency power of 400 kHz. The temperature of the specimen was monitored indirectly by measuring the temperature of the graphite heating element using a dual-wavelength (0.50 μm and 0.58 μm) alternated intensity-ratio computing type two-color pyrometer. The signal of the pyrometer was calibrated using the melting points of the following substances: silver (1235.0 K), copper (1356.6 K), Ni-22.5 mass%Nb eutectic alloy (1539 K), Ni-54 mass%Cr eutectic alloy (1618 K), nickel (1726 K) and cobalt (1768 K). The furnace could control the temperature of the specimen within the range between 1200 K and 1800 K.

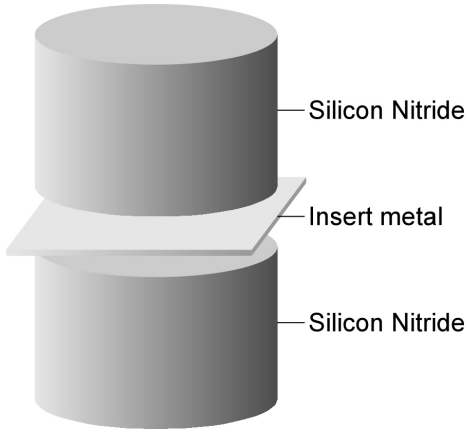

Fig. 3.2 Schematic illustration of a diffusion bonding specimen.

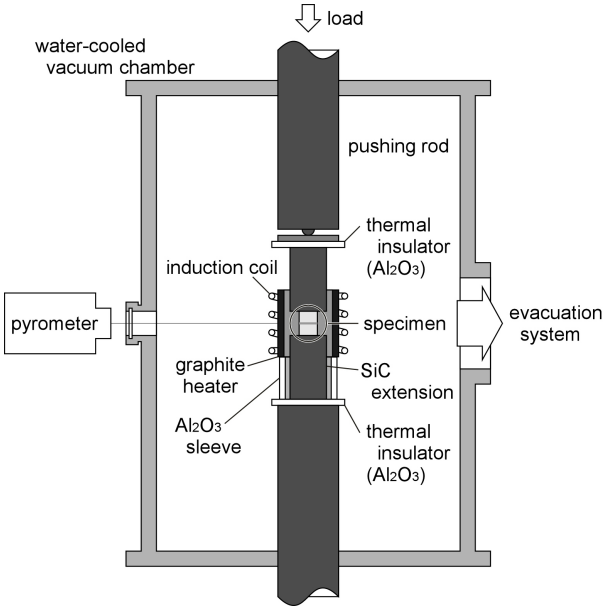

Fig. 3.3 Schematic illustration of the diffusion bonding furnace.

B. Bonding Conditions

After setting the bonding specimen in the chamber of the furnace, the chamber was evacuated down below 1×10^{-3} Pa. The specimen was heated up with the rate of 0.60 K s^{-1},

which was adequate for maintaining the vacuum in the chamber below 1×10^{-3} Pa. The time, at which the temperature of the specimen reached the programmed bonding temperature (T_0), was set as the initial state ($t = 0$). Reaching the programmed bonding temperature, a uniaxial pressure of 140 MPa, perpendicular to the bonding interface, was applied to the specimen with the pushing rods throughout the bonding treatment. The specimen has been held in this state for the programmed bonding time (t_0). The specimen was cooled down with the rate of –0.28 K s^{-1} until 1200 K, and the further cooling was made by furnace cooling for 3.6 ks without temperature control. This procedure is schematically summarized in **Fig. 3.4**.

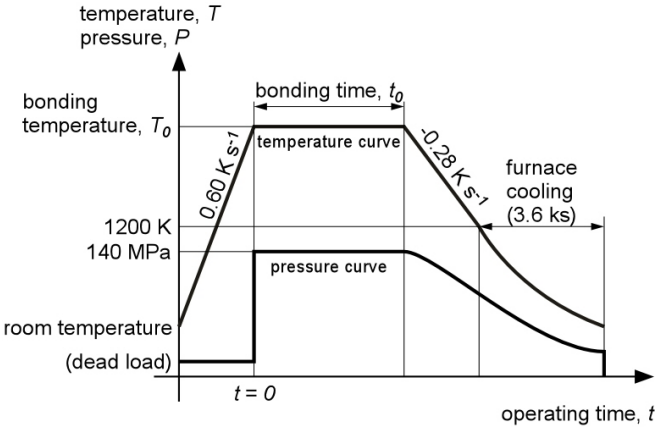

Fig. 3.4 Schematic illustration of the procedure of the bonding treatment.

Table 3.3 The range of the bonding conditions employed in the present study.

Material	Range of the bonding temperature, T / K	Range of the bonding time, t / ks
titanium	1373 ~ 1673	0.23 ~ 32.4
vanadium	1273 ~ 1673	0.2 ~ 360.0
niobium	1473 ~ 1773	0.9 ~ 90.0

The range of the bonding temperature and time for each insert metal employed in the present study are listed in **Table 3.3**.

III. Analysis of the Joints

A. Microstructure Analysis

The interfacial microstructures of the joints were analyzed with the combination of scanning electron microscopy (SEM), wavelength-dispersive electron probe microanalysis (WDS-EPMA) and X-ray diffractometry (XRD).

The specimen preparation for the SEM observation and the WDS analysis was done with the following procedure. Each joint was embedded in a columnar mold of epoxy resin (25 mm in diameter) to be the joint interface perpendicular to the basal plane of the mold. The

molds were cut to reveal the central cross-section of the joint interface (parallel to the basal plane of the molds) with a wet type diamond-composed grinding wheel. One side of the sectioned specimen was used for the SEM observation and the WDS analysis, while the other side of the specimen was taken out of the resin and applied to the XRD analysis. The cross-sectional specimens of the joint interfaces were flattened with the 220 mesh and 30 μm diamond-embedded grinding discs and polished with the 15 μm, 3.0 μm, and 0.25 μm diamond-paste-spread polishing clothes. Then, the specimens were cleaned using an ultrasonic bath with water and immediately dried with a cold blower. Finally, in order to avoid charging-up during the SEM observation and the WDS analysis, the surfaces of the specimens were thinly coated with carbon using a high-vacuum deposition apparatus in a vacuum of 1×10^{-3} Pa or below.

The SEM observation was implemented using 15 keV electrons. The back-scattered electron images of the interfacial microstructures were taken in order to reveal the compositional differences as the contrasts. The thickness or the sizes of the reaction phases appearing at the interfaces were measured from the micrographs.

The WDS analysis was implemented using 15 keV electrons with the probe current of 2.50×10^{-8} A. The characteristic X-rays and corresponding dispersive crystals used for the composition analysis of silicon, nitrogen, titanium, vanadium and niobium were respectively Si Kα (PET), N Kα (LDE1), Ti Kα (PET), V Kα (PET) and Nb Lα (PET). The standard materials used for the quantitative composition analysis of silicon, nitrogen, titanium, vanadium and niobium were respectively Si, Si_3N_4, Ti, V, and Nb. The ZAF correction was made automatically by the computer installed in the WDS apparatus.

Each specimen for the XRD measurement was cut at one side of the Si_3N_4 in the vicinity of the interface, parallel to the interface. The specimen was then ground down from the cut side of Si_3N_4 carefully in a uniform condition, *e.g.*, ten-stroke manual grinding using the 30 μm diamond embedded grinding disc, for each XRD measurement. This process was repetitively conducted until the XRD peaks corresponding to other phases than Si_3N_4 completely disappears. The position of each measurement was roughly estimated dividing the thickness of the insert foil, including the reaction phases, measured from the SEM micrograph. Every XRD measurement was implemented using the Cu Kα line (λ = 1.540562 Å) with the

monochrometer located on the path of the scattered X-ray. The power input to the X-ray tube was set to 1200 W (40 kV and 30 mA). The analysis of the XRD patterns was carried out manually using the databases [3.1, 3.2].

The results of the SEM, WDS-EPMA and XRD are finally put together to estimate the compatibility of the data and to determine the interfacial microstructures.

B. Fracture Strength Evaluation and Fracture Analysis

The strength of the joints was evaluated with the shear fracture test. **Fig. 3.5** shows a schematic illustration of the testing jig used in the present study. The jig consisted of three parts: a sleeve and two specimen holding parts. The shear plane was located between the specimen holding parts, which moved to the opposite direction of each other. The specimen was held by a bed made of hot die steel SKD-61 and supported with a pair of screws. The sleeve avoided the separation of the holding parts to the direction perpendicular to the shear plane.

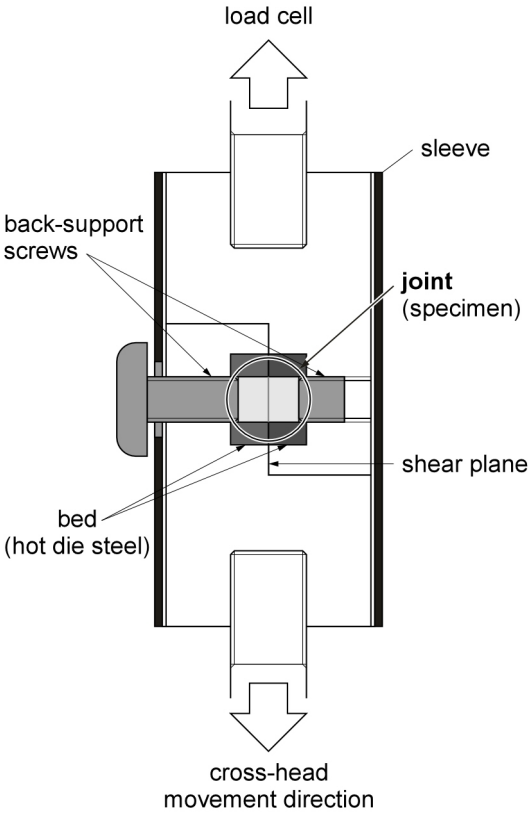

Fig. 3.5 Schematic illustration of the shear fracture testing jig for the joint specimens.

At first, the insert foil spilling out of the bond interface was removed with a dry 1500 mesh emery paper. Then, the specimen was set on one side of the holding jig. The position of the bond interface was adjusted to the shear plane of the jig. The other side of the jig was then set together and fixed in the sleeve. The jig was then installed in a tensile testing machine equipped with a 9.8 kN load-cell.

The test was implemented with a cross-head speed of 1.67×10^{-5} m s^{-1} at the ambient temperature and atmosphere. Five specimens at least were tested for each bonding condition.

Both sides of the fracture surfaces were analyzed with the combination of XRD, SEM and WDS. At first, the macroscopic fractographs of the surfaces were taken with a

conventional optical camera. Then, the XRD patterns of the fracture surfaces were taken. Finally, the surfaces were thinly coated with carbon using a high-vacuum deposition apparatus for SEM observation and WDS analysis. The conditions and settings of XRD, SEM and WDS were the same as that of the microstructure analysis.

References

[3.1] *Powder Diffraction Files*, JCPDS–International Centre for Diffraction Data (formerly the Joint Committee on Powder Diffraction Standards), Newtown Square, Pennsylvania (USA).

[3.2] P. Villars and L.D. Calvert: *Pearson's Handbook of Crystallographic Data for Intermetallic Phases*, American Society for Metals, Metals Park, Ohio (USA), 1985.

Chapter 4 Solid State Diffusion Bonding of Silicon Nitride using Titanium Foils

This chapter presents an effective way to control the interfacial reaction during solid state diffusion bonding of silicon nitride (Si_3N_4) using titanium foils. The interfacial structure and its growth kinetics were analyzed in detail with SEM, EPMA and XRD. The actual phase sequence of the joint interfaces bonded at temperatures between 1473 K and 1673 K is concluded to be Si_3N_4 / Ti_5Si_3(N) / α-Ti(N) + Ti_5Si_3(N), which is different from the phase sequence observed at room temperature after bonding. The joints are very weak due to the formation of a brittle Ti_5Si_3(N) layer at the interface. To suppress the growth of the Ti_5Si_3 layer, a nitrogen solution treatment of titanium foils prior to each bonding experiment is implemented. Although a perfect prevention of the Ti_5Si_3(N) layer formation is not achieved with this treatment, it is shown that the growth of the layer is effectively suppressed enough to improve the joint strength to a level three times higher than the case in which pure titanium is employed.

I. Introduction

For Si_3N_4 bonding, titanium plays an important role. That is to enhance adsorption and wetting between Si_3N_4 and metals. For this purpose, titanium is commonly used as an active additive of filler metals or brazes for ceramics bonding [4.1-4.5]. On the other hand, it is well known that an inappropriate bonding of Si_3N_4 with metals containing titanium causes the formation of brittle phases and the reduction of joint strength. Especially for solid state diffusion bonded Si_3N_4 joints using a pure titanium insert metal, it has been reported that they reveal very poor strength [4.6-4.8]. These reports suggest that controlling the interfacial

reaction and structure between Si_3N_4 and titanium in an appropriate state, in which the formation of such brittle phases is suppressed, is one of the most important techniques for successful bonding. Moreover, such a control technique for interfacial reactions will allow researchers to carry out more accurate residual stress analysis and life assessment of the joints, which is essential for practical structural design.

Although the importance of controlling the interfacial structure and reaction between Si_3N_4 and titanium is well recognized, a problem has to be overcome even to obtain a basic knowledge of the interfacial structure. This is the wavelength overlap of the characteristic X-rays for Ti Ll and N Kα. This problem makes it difficult to measure the composition of nitrogen quantitatively. Due to the difficulty of obtaining these essential data, the interpretation of the interfacial structure differs among the reports concerning the reaction between Si_3N_4 and titanium [4.6-4.15].

The present study aims to control the interfacial reaction during solid state diffusion bonding of Si_3N_4 using Ti foils. At first, the interfacial structure and its growth behavior are analyzed in detail. In the next step, the controlling factor of the reaction is extracted. Then finally, an example to control the reaction is presented.

II. Experimental Procedure

Si_3N_4 specimens were prepared from pressureless sintered columnar rods, whose diameter and length were 6.0 mm and 40.0 mm, respectively. They contained a few mass percentages of alumina (Al_2O_3), yttria (Y_2O_3) and tungsten di-silicide (WSi_2) as the sintering agents. The rods were cut to a length of 4.0 mm. Then, the surface to be bonded was polished with 3 μm diamond paste. The roughness of the obtained surface was about 0.032 μm. On the other hand, 99.5 % nominally pure titanium foils with three different thicknesses (20.0 μm, 50.0 μm and 150 μm) were used as the insert metal. Both sides of the titanium surfaces were polished with a 0.3 μm alumina suspension just before the bonding treatment in order to minimize the surface scale formation. The surface roughness of the foils was about 0.100 μm.

Two Si_3N_4 specimens and a titanium foil were used for each bonding experiment. They were first cleaned in an ultrasonic bath with acetone. Then, the titanium foil was inserted between two Si_3N_4 specimens, and they were set into an induction-heating vacuum furnace.

The bonding temperature and time were set at certain values between 1373 K and 1673 K and between 0.2 ks and 32.4 ks, respectively. The heating and cooling rates were set to 0.60 Ks^{-1} and 0.28 Ks^{-1}, respectively. The vacuum inside the furnace was kept below 1.3×10^{-3} Pa. A uniaxial pressure of 140 MPa, perpendicular to the bonding interface, was applied to the specimen throughout the bonding treatment.

The interfacial structure of the obtained joints was estimated by a combination of scanning electron microscopy (SEM), wavelength-dispersive electron probe microanalysis (WDS-EPMA) and X-ray diffractometry (XRD). The quantitative composition measurement by EPMA was implemented utilizing a ZAF correction program. Against the peak overlap problem of titanium and nitrogen, an additional correction was carried out. It is to remove the overlapping signal of the Ti Ll peak from the measured N Kα signal prior to the ZAF correction. The intensity of the Ti Ll peak, ($I_{\mathrm{Ti\,L}l}$) is derived using the following equation:

$$I_{\mathrm{Ti\,L}l} = \xi \times I_{\mathrm{Ti\,K}\alpha}\,, \tag{4.1}$$

where ξ is the empirically obtained intensity ratio between the Ti Kα peak and the Ti Ll peak, which is calibrated with some TiN with known compositions. Hence, the actual intensity of the N Kα peak ($I^{\mathrm{actual}}_{\mathrm{N\,K}\alpha}$) is expressed in the following formula:

$$I^{\mathrm{actual}}_{\mathrm{N\,K}\alpha} = I^{\mathrm{measured}}_{\mathrm{N\,K}\alpha} - I_{\mathrm{Ti\,L}l} = I^{\mathrm{measured}}_{\mathrm{N\,K}\alpha} - \xi \times I_{\mathrm{Ti\,K}\alpha}\,. \tag{4.2}$$

The deduced value of $I^{\mathrm{actual}}_{\mathrm{N\,K}\alpha}$ was used for the ZAF calculation (*cf.* Chapter 2-IV-*C*), instead of the measured intensity of the N Kα peak ($I^{\mathrm{measured}}_{\mathrm{N\,K}\alpha}$).

The joint strength was estimated by shear fracture testing. The fracture test was implemented with a cross-head speed of 1.67×10^{-5} m s^{-1} at ambient temperature and atmosphere. Seven samples were tested for each bonding condition.

III. Results and Discussion

A. Bondability

With some combinations of bonding temperature and time, solid state diffusion bonding experiment fails to obtain joints of Si_3N_4. The success and failure of the bonding experiment at each employed bonding condition are listed in **Table 4.1**. In the table, “S” means that the bonding at the condition succeeds, while “F” means that it fails. At bonding temperature of 1373 K, every bonding experiment turned out to be unsuccessful. However, at the bonding

temperature of 1473 K, the bonding is successful with a bonding time of 3.6 ks or longer. At the higher bonding temperatures of 1573 K and 1673 K, a very short bonding time of 0.23 ks is enough to obtain joints.

Table 4.1 Bondability at each employed combination of temperature and time.

Bonding time, t / ks	Bonding temperature, T / K			
	1373	1473	1573	1673
0.23	–	–	S	S
0.9	–	F	S	S
3.6	F	S	S	S
14.4	F	S	S	S
32.4	–	–	S	S

B. Interfacial Microstructure of Si_3N_4 / Ti Joints

The interfacial structures of the Si_3N_4 / Ti joints bonded at 1473 K, 1573 K and 1673 K were analyzed by means of SEM, EPMA and XRD. Since the same microstructure is formed

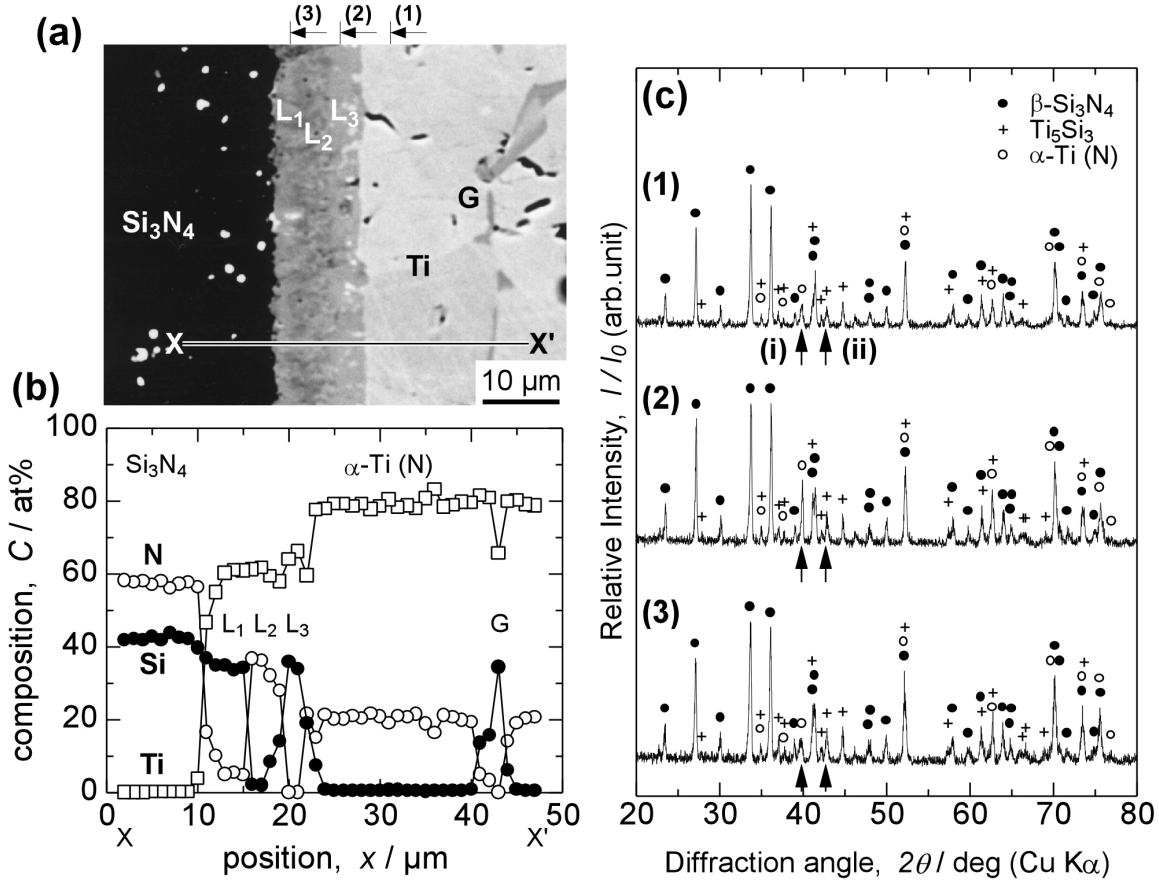

Fig. 4.1 Interfacial microstructure of a Si_3N_4 / Ti joint bonded at 1573 K for 3.6 ks using a 50 μm thick Ti foil. (a) SEM micrograph, (b) compositional distribution profile along X to X' depicted in the micrograph, (c) X-ray diffraction patterns from the positions (1), (2) and (3) depicted in the micrograph.

on both sides of titanium foil by reaction with Si_3N_4, one side of the interfaces is presented in the following figures. **Fig. 4.1** shows the interfacial microstructure of a Si_3N_4 / Ti joint bonded at 1573 K for 3.6 ks using a 50 μm thick titanium foil. **Fig. 4.1 (a)** is an SEM micrograph of the interface. The dark region on the left-hand side and the bright region on the right-hand side of Fig. 4.1 (a) correspond to Si_3N_4 and Ti, respectively. Two types of reaction products are observed in the micrograph. One is formed as a 11.5 μm thick layer between Si_3N_4 and Ti. The other is formed as grains (marked as "G") inside the Ti foil. The layered one consists of three regions, which are marked as "L_1", "L_2" and "L_3", respectively. The regions L_1 and L_3 have homogeneous contrasts. This means that these regions consist of one phase. On the other hand, the region L_2 presents a two-contrast mixture, which indicates that this region consists of two phases. The granular phase G is observed on the grain boundaries of the titanium. **Fig. 4.1 (b)** shows the elemental distribution profile along the line from X to X' in Fig. 4.1 (a). Three points are clearly noticed in this figure. The first is that the G, L_1 and L_3 phases consist of only titanium and silicon. The nitrogen content in these phases is very low. The composition of these phases presents the same ratio of Ti-35 at%Si. This fact indicates that these phases are the same. The second point noted is that the composition of the second phase in L_2 is Ti-38 at%N. The silicon content in this phase is very low. The third point is that nitrogen in the titanium matrix is homogeneously distributed with a composition of Ti-21 at%N. The silicon content in the titanium is very low. **Fig. 4.1 (c)** shows a series of XRD patterns which correspond to the positions (1), (2), and (3) depicted on the top of Fig. 4.1 (a). The specimens were cut at one side of the Si_3N_4 in the vicinity of their interfaces and polished carefully about 1 μm for each XRD measurement. Each reaction product and its arrangement were identified by the position of each XRD peak and the alteration of its relative intensity. All three patterns in Fig. 4.1 (c) are identified as superimpositions of Si_3N_4 [4.16], Ti_5Si_3 [4.17] and α-Ti(N) [4.18]. The appearance of all existing phases in every step of the XRD measurements is due to the difficulty of polishing flat and parallel to the interface. However, the alteration of the relative intensity appears clearly at the peaks at 39.88° and 42.82°, which are marked with arrows (i) and (ii), respectively. The peak (i) corresponds only to the 101 plane of α-Ti(N). Compared with pattern (1), this peak is intensified in pattern (2) and then it reduces its relative intensity in pattern (3). The peak (ii), on the other hand, corresponds only

to the 112 plane of Ti_5Si_3. This peak is intensified in pattern (2) and keeps its relative intensity in pattern (3). Taking into account the detection depth of the diffracted X-ray in the specimen, this result agrees well with the EPMA depicted in Fig. 4.1 (b). These results indicate that L_1, L_3 and G are all Ti_5Si_3 single phase and that L_2 is a mixture of Ti_5Si_3 and α-Ti(N). Therefore, the observed phase sequence is finally identified as Si_3N_4 / Ti_5Si_3 / Ti_5Si_3 + α-Ti(N) / Ti_5Si_3 / α-Ti(N) + Ti_5Si_3.

In the same way, the interfacial structure of the joints bonded at 1473 K and 1673 K was also analyzed. **Fig. 4.2** shows a SEM micrograph of a joint interface bonded at 1473 K for 3.6 ks using a 50 μm thick Ti foil, with the result of phase identification. Being similar to the interfacial structure formed at 1573 K, there are observed a 7.5 μm thick layer adjacent to Si_3N_4 and Ti_5Si_3 granules in α-Ti phase as the reaction products. The layered reaction product consists of two regions: the Ti_5Si_3 single phase region on the Si_3N_4 side and the Ti_5Si_3 + α-Ti(N) mixture phase region on the Ti side. Therefore, the phase sequence at 1473 K is described as Si_3N_4 / Ti_5Si_3 / Ti_5Si_3 + α-Ti(N) / α-Ti(N) + Ti_5Si_3. The single phase region of Ti_5Si_3 on the Ti side (L_3 in Fig. 4.1 (a)), is not observed in the joints bonded at 1473 K. **Fig. 4.3** shows a SEM micrograph of a joint interface bonded at 1673 K for 3.6 ks using a 150 μm thick Ti foil, with the result of phase identification. The thickness of the layered reaction product becomes to 19.0 μm under this bonding condition. The phase sequence at 1673 K is

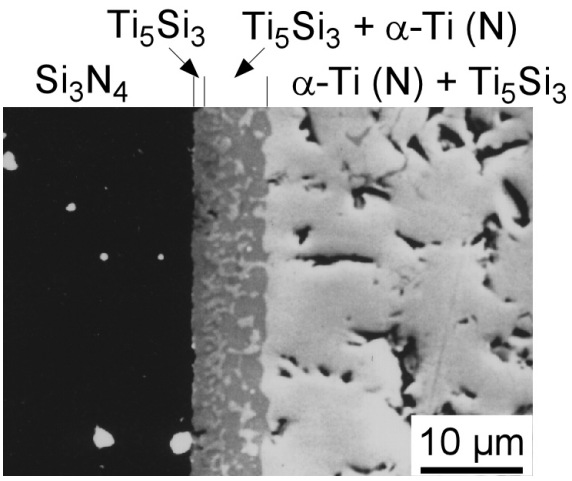

Fig. 4.2 Interfacial microstructure of a Si_3N_4 / Ti joint bonded at 1473 K for 3.6 ks using a 50 μm thick Ti foil.

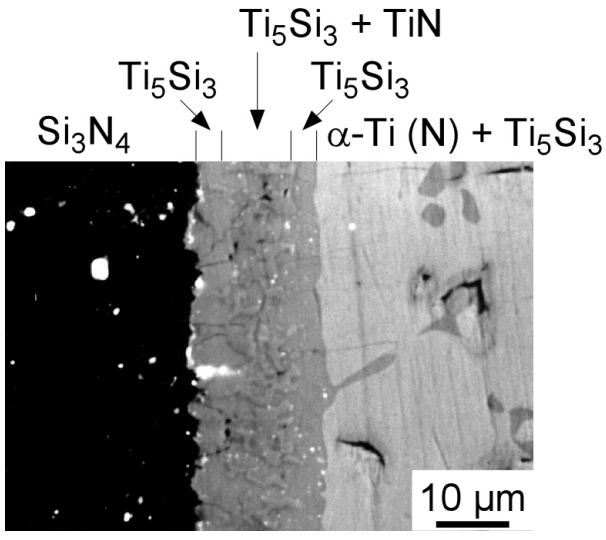

Fig. 4.3 Interfacial microstructure of a Si_3N_4 / Ti joint bonded at 1673 K for 3.6 ks using a 150 μm thick Ti foil.

described as Si_3N_4 / Ti_5Si_3 / Ti_5Si_3 + TiN / Ti_5Si_3 / α-Ti(N) + Ti_5Si_3. In the layered reaction product of the joints bonded at 1673 K, TiN appears instead of α-Ti(N), which is different from the joints bonded at 1573 K or below.

Figs. 4.1, 4.2 and 4.3 show interfacial microstructures at different bonding temperatures, but the same bonding time of 3.6 ks. Three points appear clear by comparing the morphology of the layered reaction product on the figures. The first point is that the layered reaction product is thicker at higher bonding temperatures. This result indicates that the growth rate of the layer depends on the bonding temperature. The growth kinetics of the layered reaction product will be discussed in detail in section *D*. The second point is that α-Ti(N) or TiN particles in the L_2 region grow larger at higher bonding temperatures and their number density is greater at lower bonding temperatures. This phenomenon can be explained by the temperature dependence of the mobility of nitrogen in $Ti_5Si_3(N)$. At higher bonding temperatures, since the mobility of nitrogen is higher, nitrogen atoms at locations farther from the particles can participate in the growth of the particles rather than precipitate as new nuclei of α-Ti(N) or TiN. Therefore, the particles appear larger with a lower number density at higher bonding temperatures. The third point is that the single phase region of Ti_5Si_3 adjacent to Si_3N_4 (L_1) appears in every bonding temperature. This common characteristic affects severely the strength of the joints, as described in section *C*.

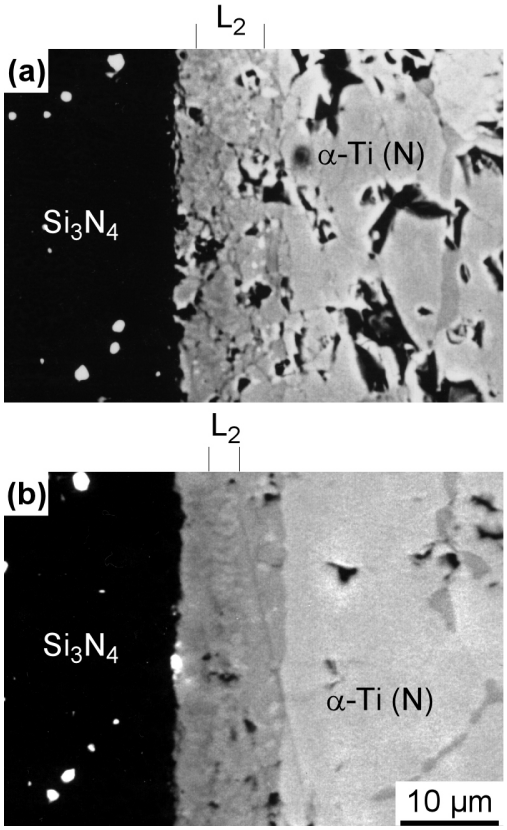

Fig. 4.4 Effect of the cooling rate on the interfacial microstructure of Si_3N_4 / Ti joints bonded at 1573 K for 3.6 ks using 50 μm thick Ti foils. (a) Cooled down with rate of 5.00 Ks^{-1}, (b) 0.07 Ks^{-1}.

It has to be taken into account that the analysis of the interfacial structures is carried out at room temperature. There can exist some phase transformation during cooling. In

those cases, the observed microstructures may not correspond to the actual structure at the elevated temperature. **Fig. 4.4** shows the effect of cooling rate on the interfacial structure. The bonding temperature and time were set as 1573 K and 3.6 ks, respectively. Only the cooling rate is different between Figs. 4.4 (a) and (b), which is 5.00 Ks^{-1} and 0.07 Ks^{-1}, respectively. By changing the cooling rate, no new phases are detected to appear. The difference in the microstructure appears only to the α-Ti(N) in the L_2 region. Two differences are recognized from this figure. One is the thickness of the L_2 region. It appears thicker in the rapidly cooled specimens than the slowly cooled ones. The other is the position of the L_2 region in the layered reaction product. The region is formed near the Si_3N_4 in the rapidly cooled specimens, while it is located at the center in the slowly cooled ones. On the other hand, the morphology of the Ti_5Si_3 in the titanium matrix appears to be independent of the cooling rate. These results indicate that the α-Ti(N) phase in the L_2 region is formed during the cooling process, while the Ti_5Si_3 in the titanium matrix exists stably at the elevated temperatures.

Indeed, it is hard to consider from the thermodynamical point of view that α-Ti(N) or TiN phases isolated inside Ti_5Si_3 exist stably at elevated temperatures, as observed. They are considered to have precipitated during cooling due to the decrease of nitrogen solubility in Ti_5Si_3. The nitrogen solubility in Ti_5Si_3 is reported as 11 at% at 1373 K [4.8] and 3 at% at 1273 K [4.19]. This means that a great solubility decrease of nitrogen in Ti_5Si_3 occurs during cooling. As a result, α-Ti(N) or TiN precipitates in the middle of the layered reaction product as the nitrogen-trapped region. Both sides of this region are considered as precipitation free zones of α-Ti(N) or TiN, from which nitrogen escapes forward to the titanium matrix or backward to the Si_3N_4. The formation mechanism of the precipitation free zones is considered as follows. Since diffusion of nitrogen from the Ti_5Si_3 layer toward Si_3N_4 or α-Ti during cooling is driven by the gradient of chemical potential of nitrogen, the composition of nitrogen in Ti_5Si_3(N) can decrease to a lower value than the solubility limit. In such regions, precipitation of α-Ti(N) or TiN will never occur. Furthermore, the driving force for precipitation in the Ti_5Si_3 layer is the instability (extra Gibbs free energy) of nitrogen-supersaturated Ti_5Si_3(N). In order to start precipitation, the extra Gibbs free energy needs to exceed the activation energy for α-Ti(N) or TiN formation. Therefore, there exist enough time for nitrogen to escape from Ti_5Si_3(N) and form L_1 and L_3 regions before the precipitation

starts. By rapid cooling, the time to escape is shorten. As the result, the precipitation free zones become thinner with a faster cooling rate, as shown in Fig. 4.4. On the other hand, the Ti_5Si_3 phase formed at grain boundaries of the α-Ti(N) matrix is considered to be stable even at elevated temperatures. This phase is also considered as a precipitate caused by the decrease of silicon solubility in titanium. In this case, however, the decrease of silicon solubility is not a result of the cooling, but of the phase transformation of the titanium matrix from β (cubic structure) to α (hexagonal structure), caused by the increase of nitrogen composition. The silicon solubility in β-Ti is reported as 5 at% at 1373 K [4.20]. However, dissolution of only 3.4 at% of nitrogen induces the phase transformation of the matrix to α-Ti [4.19] in which the silicon solubility is very low [4.8, 4.19]. This will result in the precipitation of Ti_5Si_3 (N) during the bonding process. Consequently, the actual phase sequence at temperatures between 1473 K and 1673 K is described as Si_3N_4 / Ti_5Si_3(N) / α-Ti(N) + Ti_5Si_3(N). It is very important information, for controlling the interfacial structure, that the layered reaction product is a single phase of Ti_5Si_3(N) at these temperatures. In the following text, the layered reaction product is named as the "Ti_5Si_3 layer".

Although the actual phase sequence is Si_3N_4 / Ti_5Si_3(N) / α-Ti(N) + Ti_5Si_3(N), the diffusion path cannot be directly drawn on the available Ti-Si-N ternary phase diagrams [4.8, 4.19]. In those diagrams, tie lines from Si_3N_4 are not connected to Ti_5Si_3(N) but to $TiSi_2$ and TiN. This is because the temperatures of those diagrams are lower than those employed in the present study. As Ti_5Si_3 can dissolve higher amount of nitrogen at higher temperatures, Ti_5Si_3(N) is

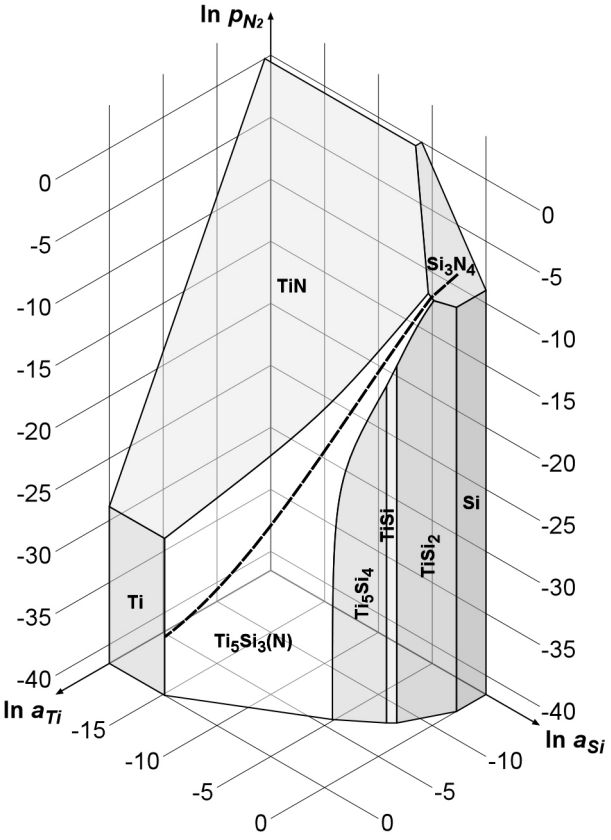

Fig. 4.5 Chemical potential diagram of Ti-Si-N ternary system at 1573 K. The dashed line depicts the diffusion path observed at the joint interfaces bonded at 1573 K.

considered to be in equilibrium with Si_3N_4 and TiN, rather than $TiSi_2$, at those higher temperatures. **Fig. 4.5** proposes a Ti-Si-N ternary chemical potential diagram at 1573 K. The diagram is drawn according to the thermodynamic data [4.19] and phase diagrams [4.8, 4.19, 4.20]. In this diagram, Ti_5Si_3 can coexist with Si_3N_4. The diffusion path observed in the present work is depicted on the diagram with a dashed line.

Some researchers have reported the formation of TiN adjacent to Si_3N_4 [4.6-4.8]. However, the interfacial structures presented in those papers indicate no existence of TiN. They have proved the existence of TiN by the existence of a gold-colored phase on the fractured surfaces of the joints. The gold-colored phase is also observed in the present work. However, it is not formed at the interface, but on the titanium metal corresponding to unbonded areas. Moreover, even if the TiN layer is assumed to be formed adjacent to Si_3N_4, the layer does not grow to an observable size with prolonged bonding treatment at 1673 K for 32.4 ks. Since it is difficult to consider that such a stable phase as TiN disappears from the interface during cooling, these results clearly suggest that this type of TiN is not formed at the areas where intimate contact of Si_3N_4 and titanium is achieved. It is considered that this type of TiN is formed by the reaction between titanium and nitrogen gas, which is generated by the spontaneous decomposition of Si_3N_4.

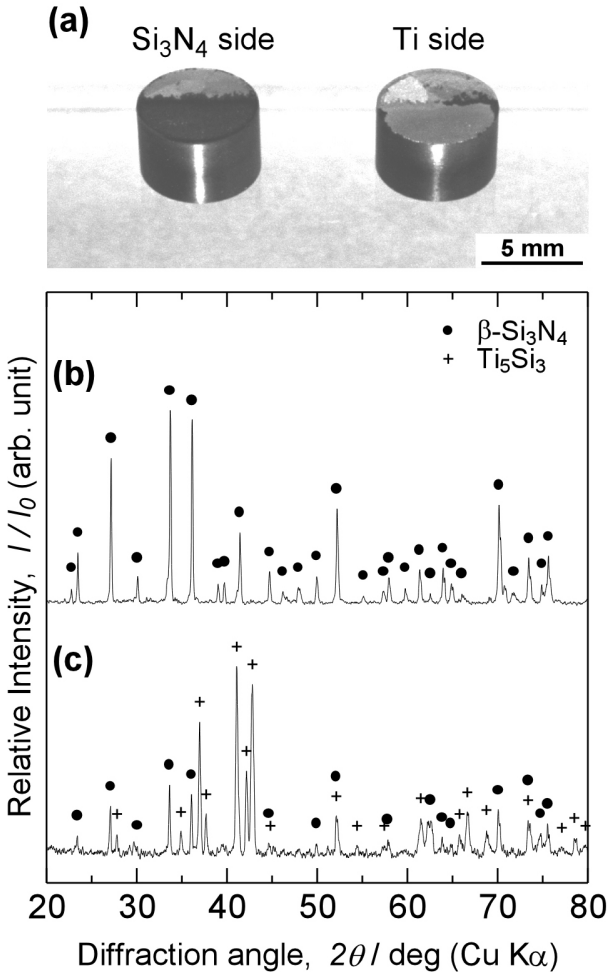

Fig. 4.6 Typical appearance of the fractured surfaces (a) and corresponding XRD patterns taken from the Si_3N_4-side (b) and the Ti-side (c) of a joint bonded at 1573 K for 3.6 ks using a 50 μm thick Ti foil.

C. Joint Strength and Fracture

In agreement with the reports by other researchers [4.6-4.8], the Si_3N_4 / Ti joints in the present study also possess very low

fracture strength at room temperature. A shear stress of 3.5 MPa is enough to fracture every joint bonded at 1573 K for 3.6 ks. **Fig. 4.6** shows a typical appearance of a fractured joint, which was bonded at 1573 K for 3.6 ks using a 50 μm thick Ti foil, and the corresponding XRD patterns taken from both sides of the fractured surfaces of the joint. The side on which the titanium foil is remaining is named the "Ti side", while the other side is named the "Si_3N_4 side" in the figure. Both sides of the fractured surfaces have a flat morphology, indicating that the fracture occurs only at the joint interface in a brittle mode. All of the peaks appearing on the XRD pattern taken from the Si_3N_4 side, shown in Fig. 4.6 (b), correspond to Si_3N_4. On the other hand, Ti_5Si_3 and Si_3N_4 are detected on the Ti side, as shown in Fig. 4.6 (c). However, Si_3N_4 exposed on the fractured surface is detected only at areas where the insert metal has been chipped off. No Si_3N_4 particles are detected on the Ti_5Si_3, which is the major phase on the fractured surface of the Ti side. Thus, the Si_3N_4 observed on the Ti side is considered as the Si_3N_4 on the counterpart of the joint. Based on this result, the fracture is determined to occur at the Si_3N_4 / Ti_5Si_3 interface.

The thermal expansion mismatches at the observed neighboring phase interfaces, Si_3N_4 / Ti_5Si_3, Ti_5Si_3 / TiN and Ti_5Si_3 / Ti have been reported as 7.8×10^{-6} K^{-1}, 1.6×10^{-6} K^{-1} and 0.5×10^{-6} K^{-1}, respectively [4.14]. This result indicates that the Si_3N_4 / Ti_5Si_3 interface yields a larger thermal residual stress than any other phase interface. On the other hand, Iseki *et al.* [4.21] have reported that the bending strength of Ti_5Si_3 is as weak as 70 MPa. Since it is very easy to predict that the fracture occurs within the phase, avoiding the formation of the Ti_5Si_3 phase is recommended, if possible [4.21]. These reports support the present result that the fracture occurs at the Si_3N_4 / Ti_5Si_3 interface.

Preventing the formation of the Ti_5Si_3 layer will be the most effective way to increase the joint strength of the present system. However, as Ti_5Si_3 is thermodynamically stable, it is difficult to achieve bonding without the formation of the Ti_5Si_3 layer. Indeed, the bonding experiment fails when the bonding condition is set to low temperatures and short times as shown in Table 4.1. As the second best, it is necessary to control the interfacial reaction and its resultant structure to suppress the growth of the Ti_5Si_3 layer and to form other phases rather than Ti_5Si_3 adjacent to Si_3N_4.

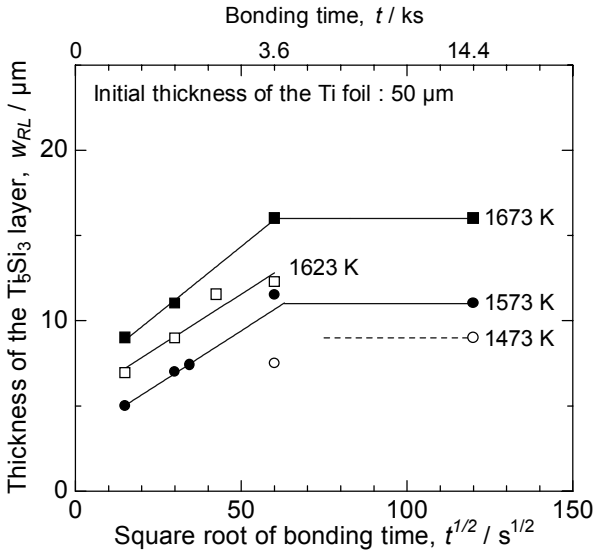

Fig. 4.7 Growth behavior of the Ti_5Si_3 layer in the case that 50 μm thick Ti foil is used.

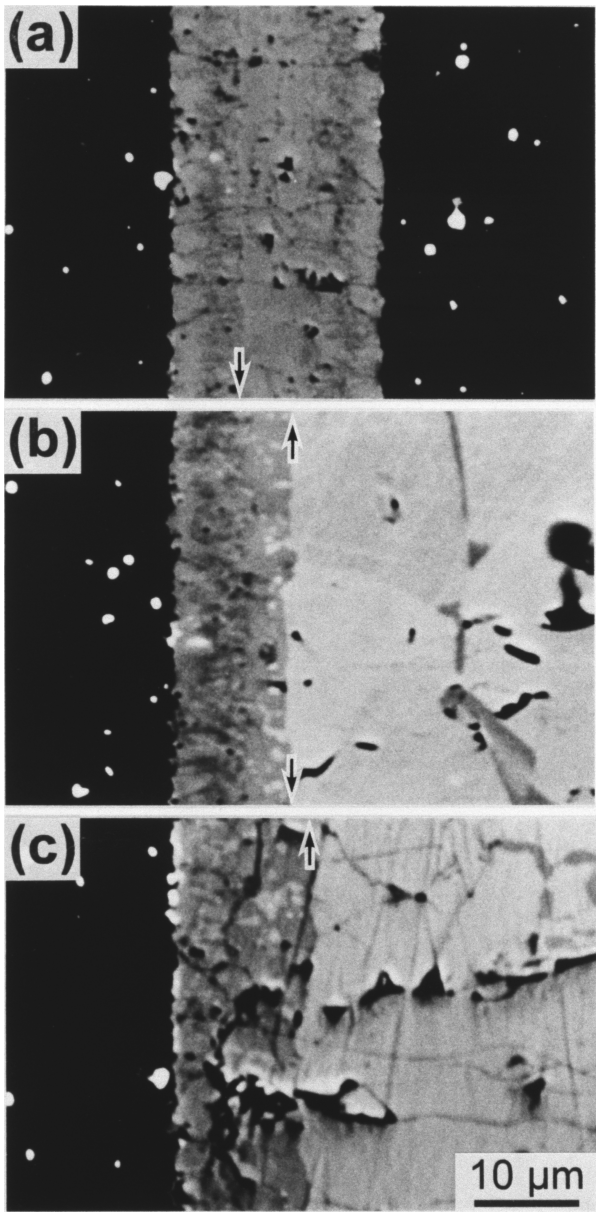

Fig. 4.8 Effect of the initial Ti foil thickness on the growth of the Ti_5Si_3 layer for the joints bonded at 1573 K for 3.6 ks. (a) Bonded using 20 μm thick Ti foil, (b) 50 μm, (c) 150 μm.

D. Growth Kinetics of the Ti_5Si_3 Layer

Fig. 4.7 shows the growth behavior of the Ti_5Si_3 layer in the case in which a 50 μm thick titanium foil is used. The thickness of the Ti_5Si_3 layer, w_{RL}, which was measured from the micrographs of the joint interfaces, is plotted as a function of the square root of the bonding time ($t^{1/2}$). The growth kinetics of the Ti_5Si_3 layer is clearly divided into two stages. In the earlier stage, the Ti_5Si_3 layer grows proportionately with the square root of the bonding time, which obeys the parabolic law. The growth behavior of the Ti_5Si_3 layer in this stage is expressed using an Arrhenius-type function as

$$w_{RL} = \sqrt{k_0 t \exp(-Q/RT)} \tag{4.3}$$

where k_0 is the pre-exponential factor for the growth rate of the Ti_5Si_3 layer, Q is the apparent activation energy for growth of the Ti_5Si_3 layer, R is the gas constant and T is the bonding

temperature. The values of k_0 and Q are calculated as 2.58×10^{-11} m^2s^{-1} and 97.9 kJ mol^{-1}, respectively. The growth rate is controlled by the diffusion of silicon through the Ti_5Si_3 layer, which will be discussed later in detail. In the latter stage, the Ti_5Si_3 layer stops growing.

The saturation of the growth at the latter stage is very interesting. It should be useful for the suppression of the growth of the Ti_5Si_3 layer. In order to find out the factor determining the thickness limit of the Ti_5Si_3 layer, the effect of the initial titanium foil thickness was then investigated.

Fig. 4.8 shows the dependence of the thickness of the Ti_5Si_3 layer on the initial titanium foil thickness. All the joints depicted in Fig. 4.8 are bonded in the same condition, at 1573 K for 3.6 ks. The difference among the joints is only the initial titanium foil thickness. It appears clearly that the Ti_5Si_3 layer grows thicker when the thicker titanium foil is used, regardless of the same bonding temperature and time. The thickness of the Ti_5Si_3 layer is measured as 7.0, 11.5 and 14.0 μm for 20, 50 and 150 μm thick titanium foils, respectively.

The bonding condition of 1573 K for 3.6 ks corresponds to a saturation of the growth of Ti_5Si_3 in the case of 50 μm thick titanium foils, as shown in Fig. 4.7. Since the growth rate is controlled by the self diffusion of silicon in the Ti_5Si_3 layer, the foil thickness of titanium has no effect on the growth rate. Therefore, the growth behavior shown in Fig. 4.8 implies that the growth of the Ti_5Si_3 layer saturates earlier when the thinner titanium foil is used. Namely, there exists a threshold for the growth saturation in the factor determining the thickness limit and thinner titanium foils reach the threshold faster. Taking into account that the amount of the constituents is conserved during the interfacial reaction, the nitrogen content in the α-Ti phase is extracted as the factor determining the growth saturation of the Ti_5Si_3 layer.

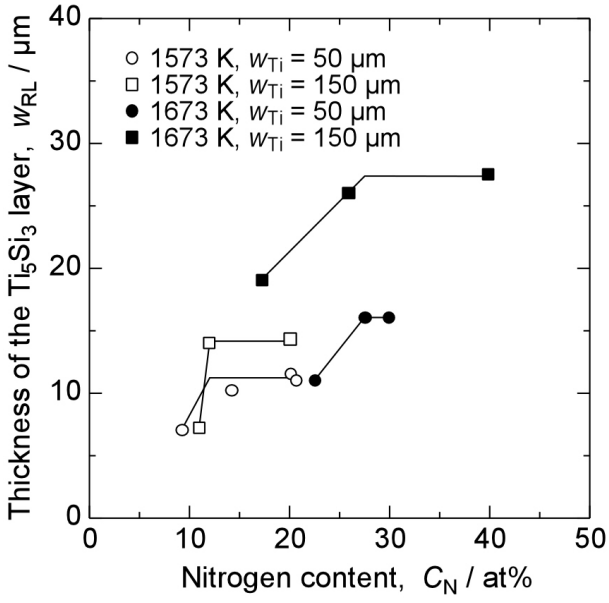

Fig. 4.9 Relation between the thickness of the Ti_5Si_3 layer and the nitrogen content in the remaining α-Ti phase.

Fig. 4.9 shows the relation between the thickness of the Ti_5Si_3 layer and the nitrogen

content in the α-Ti phase, C_N. Since the nitrogen in the α-Ti phase is homogeneously distributed as shown in Fig. 4.1 (b), the average value is taken as the representative value of C_N. One important point appears from this figure. The Ti_5Si_3 layer stops its growth when the nitrogen content in α-Ti reaches a certain value, C_N*, which is a function of the bonding temperature. For instance, the value of C_N* is about 12 and 28 at% for 1573 K and 1673 K, respectively.

In consequence, it is concluded that the factor determining the thickness limit is the nitrogen content in the α-Ti phase and that the threshold for the growth saturation is obtained as C_N*(T)*. Based on this conclusion, the phenomenon observed in Fig. 4.8 is explained as follows. The nitrogen content in Ti phase increases by the dissolution of nitrogen originated from the decomposition of Si_3N_4. On the other hand, the other element of Si_3N_4, silicon, reacts with Ti to form Ti_5Si_3. The amount of nitrogen dissolved in the α-Ti phase balances with the amount of silicon in the Ti_5Si_3 layer, with regard to the mass conservation law. The amount of silicon in the Ti_5Si_3 layer determines the thickness of the Ti_5Si_3 layer. Therefore, w_{RL} is kept thinner, as the thinner Ti foil requires a smaller amount of nitrogen to achieve C_N*.

The growth of the Ti_5Si_3 layer obeys the parabolic law in the early stage of growth. This result implies that the growth rate is controlled by diffusion of a constituent [4.22], either titanium or silicon. On the other hand, it was also described how the nitrogen content in the titanium-foil matrix affects the growth limit of the Ti_5Si_3 layer. Assuming that the growth front of the Ti_5Si_3 layer is located on the Si_3N_4 side, which means that the diffusion of titanium is controlling the growth rate, the growth saturation cannot be explained, because of the following two reasons. One is that the diffusion of titanium will not stop even after achieving C_N*, since the chemical potential gradient of titanium in the Ti_5Si_3 layer (between Si_3N_4 and α-Ti) is retained, as shown in Fig. 4.5. The other reason is that silicon and nitrogen are supplied from Si_3N_4 by its spontaneous decomposition. Therefore, no mechanism to stop the growth takes place. Assuming that the growth front of the Ti_5Si_3 layer is located on the α-Ti side, which means that the diffusion of silicon is controlling the growth rate, the growth saturation is explained by the prohibition of diffusion of silicon into α-Ti. Therefore, the growth front of the Ti_5Si_3 layer is located on the titanium side and the growth rate is controlled by the diffusion of silicon through the Ti_5Si_3 layer.

E. Effect of Nitrogen Pre-solution into Titanium Foil

Based on the results described in the previous sections, an increase of the nitrogen content in the Ti foils is expected to be effective in suppressing the growth of the Ti_5Si_3 layer. The mass conservation law, however, suggests that the amount of nitrogen atoms required for achieving C_N* balances with the amount of silicon in the Ti_5Si_3 layer. Therefore, a solution of nitrogen into the titanium foils prior to the bonding treatment will effectively help to achieve C_N* faster and suppress the growth of the Ti_5Si_3 layer. The nitrogen solution treatment was performed by heating the titanium foils encapsulated in quartz tubes with high-purity nitrogen gas at 1173 K for 86.4 ks. Two types of nitrogen presolved Ti foils which contained 14 or 24 at% of nitrogen were prepared by changing the pressure of the nitrogen gas. The Ti – N phase diagram [4.20] indicates that both of these compositions correspond to α-Ti(N) phase, and that both of the phases are stable throughout the range of the bonding temperatures employed in the present study.

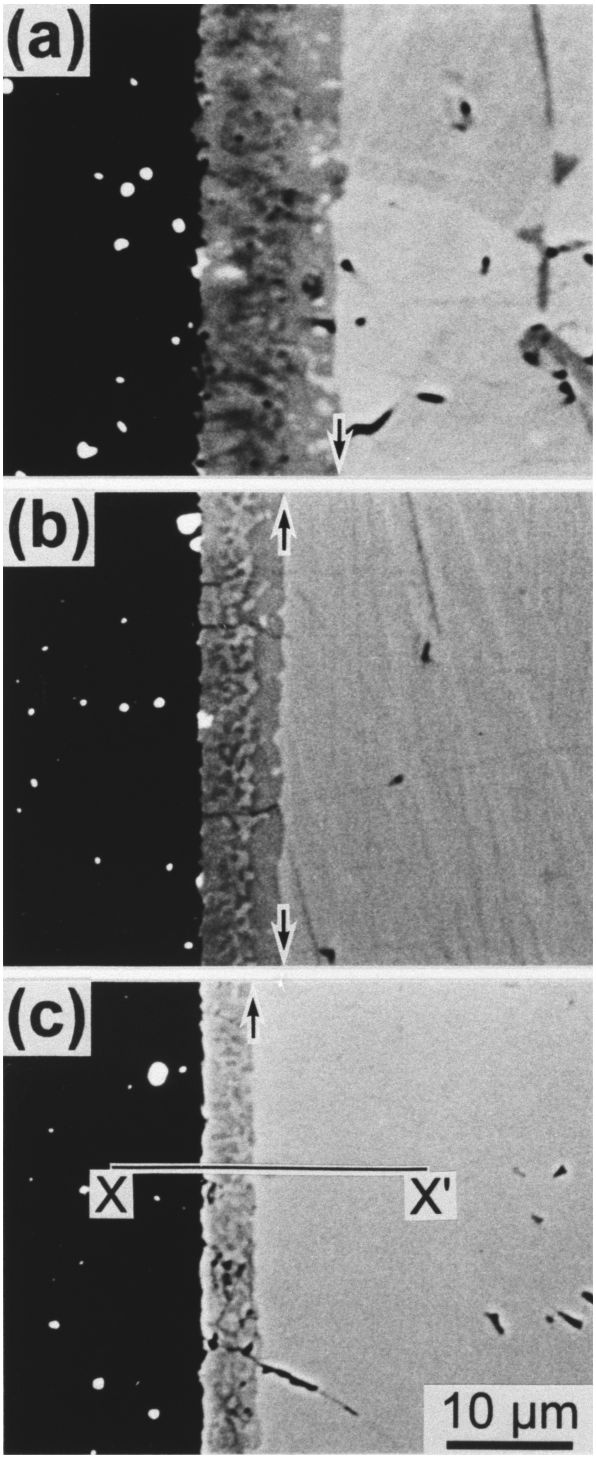

Fig. 4.10 Effect of nitrogen pre-solution on the growth of the Ti_5Si_3 layer for the joints bonded at 1573 K for 3.6 ks. (a) Bonded using pure-Ti, (b) Ti–14at%N, (c) Ti–24at%N.

Fig. 4.10 shows the effect of the nitrogen pre-solution on the growth of the Ti_5Si_3 layer. Fig. 4.10 (a), (b) and (c) depict the interfacial microstructures of Si_3N_4 /

pure-Ti, Si_3N_4 / Ti–14at%N and Si_3N_4 / Ti–24at%N joints, respectively. The bonding temperature, time and initial Ti foil thickness were set to 1573 K, 3.6 ks and 50 μm, respectively. It is obvious that the thickness of the Ti_5Si_3 layer becomes thinner when Ti foils with a higher content of nitrogen are used. The thickness of the Ti_5Si_3 layer for pure-Ti, Ti–14at%N and Ti–24at%N are 11.5 μm, 7.4 μm and 4.0 μm, respectively. This result demonstrates that a sufficient amount of nitrogen solved in the titanium foils suppresses the growth of the Ti_5Si_3 layer effectively. Moreover, the formation of granular Ti_5Si_3 on the Ti grain boundaries is completely prevented when the bonding is performed using nitrogen presolved Ti foil. The phenomenon is also observed in the case of Ti–14at%N, indicating that the diffusion of silicon into α-Ti phase is inhibited even with the use of Ti–14at%N. Attention should also be paid to the microstructure of the Ti_5Si_3 layer. The Ti_5Si_3 layer of the Si_3N_4 / Ti–24at%N joints cannot be divided into three regions like that of the Si_3N_4 / pure Ti joints. **Fig. 4.11** shows the elemental distribution profile through X to X' in Fig. 4.10 (c). The profile also shows a diffuse distribution. The EPMA-XRD combined analysis of the interface indicates that the layer consists of Ti_5Si_3 and TiN. Thus, the phase sequence at the joint interface is Si_3N_4 / Ti_5Si_3 + TiN / α-Ti(N). The most important point regarding this interfacial microstructure is that the single-phase region of Ti_5Si_3 is not formed adjacent to Si_3N_4.

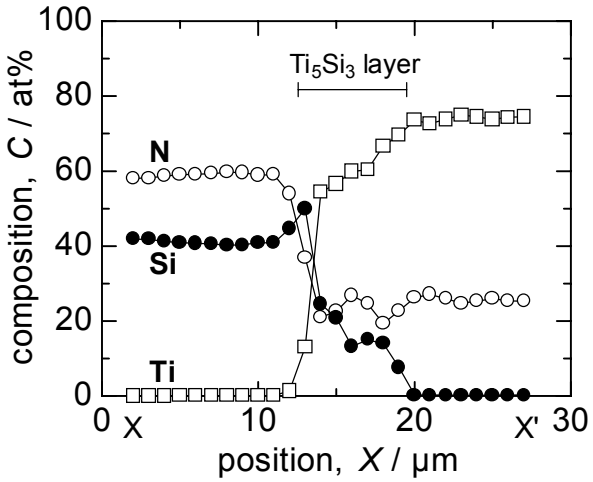

Fig. 4.11 Compositional distribution profile of a Si_3N_4 / Ti–24at%N joint interface bonded at 1573 K for 3.6 ks along X to X' depicted in Fig. 10 (c).

The joints of Si_3N_4 / Ti–24at%N (50 μm thick) bonded at 1573 K for 3.6 ks endure 10.6 MPa of shear stress. The fracture strength is improved to a greater than three times higher value than that of the joints using pure Ti. **Fig. 4.12** shows a pair of XRD patterns which are taken from the Si_3N_4 and the Ti sides of the fractured surfaces of a Si_3N_4 / Ti–24at%N joint. The XRD pattern taken from the Si_3N_4 side corresponds to Si_3N_4 and TiN. On the other hand, the XRD pattern taken from the Ti side corresponds to Ti_5Si_3, TiN and Si_3N_4. Based on this

result and the EPMA of the fractured surfaces, the fracture is determined to occur at the Si_3N_4 / Ti_5Si_3 and TiN / Ti_5Si_3 interfaces. The result of fractography clearly shows that the TiN formed adjacent to Si_3N_4 is bonded to Si_3N_4 with higher strength than is Ti_5Si_3 to Si_3N_4 and TiN.

As shown in Fig. 4.9, C_N* is 12 at% for the bonding temperature of 1573 K. Therefore, both Ti–14at%N and Ti–24at%N foils exceed C_N* even at the initial state. The results shown in Figs. 4.10, 4.11 and 4.12 evince the efficiency of the presolution treatment of nitrogen concerning C_N* for the growth suppression of the Ti_5Si_3 layer, the partial formation of TiN adjacent to Si_3N_4 and the increase of the joint strength.

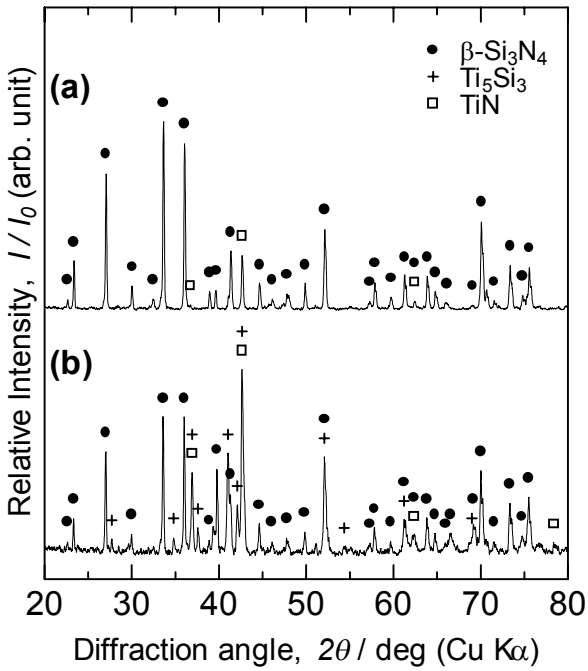

Fig. 4.12 XRD patterns taken from the Si_3N_4 side (a) and the Ti side (b) of the fractured surfaces of a Si_3N_4 / Ti–24at%N joint.

However, the strength is not still enough for practical use. Even the bonding using a Ti–24at%N foil is not able to prevent the formation of the Ti_5Si_3 layer adjacent to Si_3N_4. This can be explained based on the chemical potential diagram shown in Fig. 4.5. The presolution treatment of nitrogen for titanium foils corresponds to the artificial increase of the chemical potential of nitrogen in titanium. The increase of the chemical potential of nitrogen in titanium effectively shifts the diffusion path to go through the TiN / Ti_5Si_3(N) equilibrium line. However, to prevent the formation of the Ti_5Si_3(N) layer, the diffusion path must go across the Si_3N_4 / TiN equilibrium line. It corresponds to a shift of the diffusion path to the side of a little higher chemical potential of nitrogen. The Ti–N phase diagram [4.20] indicates that the composition of Ti–24at%N is near the edge of α-Ti / TiN equilibrium. Moreover, the chemical potential diagram shown in Fig. 4.5 indicates that the chemical potential of nitrogen at Ti / TiN equilibrium is very low, compared with that at Si_3N_4 / Ti_5Si_3(N) equilibrium. In order to guide the diffusion path to go across the Si_3N_4 / TiN equilibrium, TiN with a

considerably high chemical potential of nitrogen is required to come in contact with Si_3N_4 from the initial state of bonding. However, as is well known, TiN is hard. It means that the plastic deformation of TiN, which is required for achievement of the intimate contact between Si_3N_4 and TiN, is difficult.

However, it does not mean that the formation of a TiN layer adjacent to Si_3N_4 is impossible. For example, Nomura *et al.* [4.5] have reported an *in-situ* observation of the reaction behavior between Si_3N_4 and an active braze of Ag-Cu-Ti alloy by transmission electron microscopy. They observed clearly the formation of TiN as a layer adjacent to Si_3N_4. Comparing the results of the present study with theirs, it can be interpreted that the reduction of the chemical potential of titanium by dilution with some appropriate elements in refractory metals is a possible way to form a TiN layer adjacent to Si_3N_4.

IV. Summary

Si_3N_4 is bonded to titanium foils containing different amounts of nitrogen as solute by solid state diffusion bonding. The interfaces of the joints were analyzed by means of SEM, EPMA and XRD. The strength of the joints was estimated by a shear fracture test. The following points are clarified.

1) The interfacial phase sequence of Si_3N_4 / pure-Ti joint bonded at each employed temperature is identified as follows:

   at 1473 K: Si_3N_4 / Ti_5Si_3 / Ti_5Si_3 + α-Ti(N) / α-Ti(N) + Ti_5Si_3,

   at 1573 K: Si_3N_4 / Ti_5Si_3 / Ti_5Si_3 + α-Ti(N) / Ti_5Si_3 / α-Ti(N) + Ti_5Si_3,

   at 1673 K: Si_3N_4 / Ti_5Si_3/ Ti_5Si_3 + TiN / Ti_5Si_3 / α-Ti(N) + Ti_5Si_3.

   However, the actual phase sequence at those bonding temperatures is described as;

   Si_3N_4 / Ti_5Si_3(N) / α-Ti (N) + Ti_5Si_3(N).

2) The strength of the Si_3N_4 / pure Ti joint bonded at 1573 K for 3.6 ks is 3.5 MPa. The fracture occurs at the Si_3N_4 / Ti_5Si_3 interface.

3) The Ti_5Si_3 layer grows according to the parabolic law until the nitrogen content in the remaining α-Ti phase reaches the value of C_N*, which is a function of the bonding temperature. After achievement of C_N*, the growth of the Ti_5Si_3 layer stops.

4) The use of nitrogen presolved Ti foil effectively suppresses the growth of the Ti_5Si_3

layer. The phase adjacent to Si_3N_4 changes from a Ti_5Si_3 single phase to a Ti_5Si_3 + TiN mixed phase. The formation of granular Ti_5Si_3 on Ti grain boundaries is completely prevented.

5) Joints of Si_3N_4 / Ti - 24at% N have a fracture strength of 10.6 MPa, which is three times higher than that of Si_3N_4 / pure Ti joints bonded under the same condition. The fracture path is changed to Si_3N_4 / Ti_5Si_3 and TiN / Ti_5Si_3 interfaces.

References

[4.1] Y. Iino and N. Taguchi: *J. Mater. Sci. Lett.*, 1988, Vol. 7, pp. 981-982.

[4.2] G. Ceccone, M.G. Nicholas, S.D. Peteves, A.P. Tomsia, B.J. Dalgleish and A.M. Glaeser: *Acta Mater.*, 1996, Vol. 44, pp. 657-667.

[4.3] L. Eposito, A. Bellosi and G. Celotti: *Acta Mater.*, 1997, Vol. 45, pp. 5087-5097.

[4.4] G. Elssner and G. Petzow: *ISIJ Int.*, 1990, Vol. 30, pp. 1011-1032.

[4.5] M. Nomura, C. Iwamoto and S.-I. Tanaka: *Acta Mater.*, 1999, Vol. 47, pp. 407-413.

[4.6] K. Suganuma, T. Okamoto, Y. Miyamoto, M. Shimada and M. Koizumi: *Mater. Sci. Technol.*, 1986, Vol. 2, pp. 1156-1161.

[4.7] S. Morozumi, K. Hamaguchi, M. Iwasaki, M. Kikuchi and Y. Minonishi: *J. Japan Inst. Metals*, 1990, Vol. 54, pp. 1392-1400, in Japanese.

[4.8] M. Paulasto, J.K. Kivilahti and F.J.J. van Loo: *J. Appl. Phys.*, 1995, Vol. 77, pp. 4412-4416.

[4.9] J. Lemus and R.A.L. Drew: *British Ceram. Trans.*, 2000, Vol. 99, pp. 200-205

[4.10] I. Gotman and E.Y. Gutmanas: *J. Mater Sci. Lett.*, 1990, Vol. 9, pp. 813-815.

[4.11] P. Lamparter, S. Steeb and A. Gukelberger: *High Temperatures – High Pressures*, 1971, Vol. 3, pp. 727-740.

[4.12] A.E. Morgan, E.K. Broadbent and D.K. Sadana: *Appl. Phys. Lett.*, 1986, Vol. 49, pp. 1236-1238.

[4.13] J.C. Barbour, A.E.T. Kuiper, M.F.C. Willemsen and A.H. Reader: *Appl. Phys. Lett.*, 1987, Vol. 50, pp. 953-955.

[4.14] J.C. Schuster, F. Weitzer, J. Bauer and H. Nowotny: *Mater. Sci. Eng. A*, 1988, Vol. A105/106, pp. 201-206.

[4.15] T. Shimoo, K. Okamura and S. Adachi: *J. Mater. Sci.*, 1997, Vol. 32, pp. 3031-3036.

[4.16] Powder Diffraction File, JCPDS-ICDD, 33-1160.

[4.17] Powder Diffraction File, JCPDS-ICDD, 29-1362.

[4.18] Powder Diffraction File, JCPDS-ICDD, 41-1352.

[4.19] *Phase Diagrams of Ternary Boron Nitride and Silicon Nitride Systems*, P. Rogl and J.C. Schuster (Eds.), ASM International, Materials Park, Ohio (USA), 1992, pp. 198-202.

[4.20] *Binary Alloy Phase Diagrams*, T.B. Massalski (Editor-in-Chief), ASM International, Materials Park, OH, 1986, pp. 2054-2057.

[4.21] T. Iseki, T. Yano and Y.S. Chung: *J. Ceram. Soc. Jpn.*, 1989, Vol. 97, pp. 710-714, in Japanese.

[4.22] Y. Nakao, K. Nishimoto and K. Saida: *ISIJ Int.*, 1991, Vol. 30, pp. 1142-1150.

Chapter 5 Solid State Diffusion Bonding of Silicon Nitride using Vanadium Foils

This chapter describes the relation between the interfacial microstructure and the fracture strength of the joints of Si_3N_4 and vanadium (V) formed by solid state diffusion bonding. At first, the interfacial microstructure and its evolution process were analyzed in detail. The phase sequence at the interface changes with the bonding time showing five typical stages. In the first stage, a V_3Si layer and V_2N grains are formed. The V_2N grains contacts with the V_3Si layer at 1473 K and lower temperatures, while the contact is prohibited at 1498 K and higher temperatures. The Si_3N_4 / V_3Si interface is metastable. In the second stage, a $V_5Si_3N_{1-X}$ layer appears. In the third stage, V is annihilated. In the fourth stage, the V_3Si layer is annihilated and VN grains are formed. In the fifth stage, V_2N is annihilated. This evolution process of the interfacial microstructure agrees well with the proposed chemical potential diagram, except the metastable state of the interface. The increase and decrease behavior in the thickness of each reaction product interact with each other. The behavior of the V_3Si layer is affected not only by the formation and growth of the $V_5Si_3N_{1-X}$ layer but also by the formation of a V(Si) zone at the V_3Si / V interface. The formation of the $V_5Si_3N_{1-X}$ layer starts when the spatial gradient of the chemical potential of vanadium in the V_3Si layer decreases to a certain value. The fracture strength of the joints changes depending on the bonding temperature and time. The higher bonding temperature leads to the higher maximum fracture strength. The maximum strength at each bonding temperature is achieved when the thickness of the V_3Si layer is 2.0 μm. The prolonged bonding time gradually reduces the fracture strength down to 42 MPa.

I. Introduction

Vanadium and its alloys have become the leading candidate material for first-wall and blanket structures for fusion generators [5.1-5.4]. They exhibit low radio-activation characteristics retaining high strength and fracture toughness at high working-temperatures [5.3]. However, those vanadium structures require ceramic insulator coating on their surfaces in order to reduce the magneto-hydrodynamic pressure drop of liquid lithium coolant [5.1-5.6]. Among ceramic materials, silicon nitride (Si_3N_4) will be one of the best selection for the coating purpose [5.7]. Si_3N_4 provides a low density of 3.2×10^3 kg m^{-3} retaining high strength and creep resistance at high temperatures, favorable electrical insulation and thermal shock resistance [5.7, 5.8]. Furthermore, Si_3N_4 exhibits high resistance against radiation damage with low radio-activation characteristics of the constituent elements [5.3, 5.7, 5.9]. However, to obtain sound joints of Si_3N_4 and metallic materials, which endure the high temperatures at which Si_3N_4 exhibits its merits, is still difficult.

Vanadium is known as one of the chemically active additive elements for brazing Si_3N_4 [5.10-5.12]. This implies that vanadium enhances adsorption and wetting between Si_3N_4 and metals. However, braze materials which consist mainly of silver, copper or nickel are not preferred because those elements are severely radio-activated. Thus, direct bonding of Si_3N_4 and vanadium is required. Unfortunately, very few reports concern the direct diffusion bonding of Si_3N_4 and vanadium [5.13-5.16]. Since vanadium is a chemically active element, chemical reactions with Si_3N_4 are expected to occur. Those reports have predicted the production of vanadium silicides and nitrides, showing different analysis results of the interfacial microstructure among them. This implies that the detailed interfacial microstructure of the Si_3N_4 / vanadium joints is still unclear. Furthermore, the evolution process of the interfacial microstructure at elevated temperatures has never been reported. Such basic knowledge on the interfacial microstructure and its formation mechanism is necessary in order to control the microstructure and the performance of the joints precisely.

The present study aims to describe in detail the interfacial microstructure and its evolution process at elevated temperatures during direct solid state diffusion bonding of Si_3N_4 and vanadium at first. Then, the proper state of the interfacial microstructure is extracted on the basis of the relation between the microstructure and the fracture strength.

II. Experimental Procedure

Si_3N_4 specimens were prepared from pressureless sintered columnar rods, whose diameter and length were 6.0 mm and 40.0 mm, respectively. They contained a few mass percent of alumina (Al_2O_3), yttria (Y_2O_3) and tungsten di-silicide (WSi_2) as the sintering agents. The rods were cut to a length of 4.0 mm. Their surfaces to be joined were polished with 3 μm diamond paste. The roughness of the obtained surface was about 0.032 μm. On the other hand, the specimens of vanadium were 25 μm-thick foils with nominal purity of 99.9 %. Both sides of the vanadium foils were polished with 0.3 μm alumina suspension just before the bonding treatment in order to remove oxide scales on their surfaces. The surface roughness of the foils was about 0.13 μm.

After cleaning with an ultrasonic acetone bath, a vanadium foil was inserted between two Si_3N_4 specimens. They were set into an induction-heating vacuum furnace, applying uniaxial pressure of 140 MPa perpendicular to the bonding interfaces. The vacuum inside the furnace was kept below 1×10^{-3} Pa. The bonding temperature and time were ranging from 1273 K and 1673 K and from 0.3 ks to 360 ks, respectively.

The interfacial structure of the joints was analyzed by combination of scanning electron microscopy (SEM), wavelength-dispersive electron probe microanalysis (EPMA) and X-ray diffractometry (XRD). The quantitative composition measurement by EPMA was implemented utilizing ZAF correction program.

The strength of the joints was estimated by shear fracture test. The fracture test was implemented with cross-head speed of 1.67×10^{-5} m s^{-1} at ambient temperature and atmosphere. Five samples at least were tested for each bonding condition. The fractured surfaces were also analyzed by SEM, EPMA and XRD.

III. Results and Discussion

A. Bondability

With some combinations of bonding temperature and time, solid state diffusion bonding experiment fails to obtain joints of Si_3N_4. The bondability at each employed bonding condition are listed in **Table 5.1**, in which "S" means that the bonding at the condition succeeds, while "F" means that it fails. In order to obtain sound joints of Si_3N_4 using

vanadium insert, the bonding time of 32.4 ks, 3.6 ks, and 1.8 ks or longer is required for bonding at 1273 K, 1373 K, and 1473 K, respectively. At the bonding temperatures of 1573 K and above, very short bonding time of 0.2 ks is enough to obtain sound joints. This result indicates that longer time is required for bonding at lower temperatures. Thus, the formation kinetics of the interfacial microstructure has been investigated in relation with the bonding temperature and time.

Table 5.1 Bondability at each employed combination of temperature and time.

Bonding time, t / ks	Bonding temperature, T / K				
	1273	1373	1473	1573	1673
0.2				S	S
0.3			F	S	S
0.9	F	F	F	S	S
1.8	F	F	S	S	S
3.6	F	S	S	S	S
14.4	F	S	S	S	S
32.4	S	S	S	S	S
43.2			S		
57.6			S		
90.0			S		
360.0			S		

B. Interfacial Microstructure of Si_3N_4 / V Joints

The interfacial microstructures of Si_3N_4 / V joints bonded at low temperatures of 1273 K, 1373 K and 1473 K appear different from those at high temperatures of 1573 K and 1673 K. The interfacial microstructures at 1473 K and 1673 K are described in the following, which represent the structures at low- and high-temperature bonding conditions, respectively.

Fig. 5.1 shows the interfacial microstructure of a joint bonded at 1473 K for 3.6 ks. Fig. 5.1 (a) is an SEM micrograph of the interface. The dark regions on the left- and the right-side-end of the micrograph are Si_3N_4. The bright region on the center is vanadium. Defects such as voids and cracks are scarcely observed at the interface. Two types of reaction products are observed between Si_3N_4 and vanadium. One is formed as a 1.87 μm-thick layer, on which "L" is marked, between Si_3N_4 and vanadium. The boundary between Si_3N_4 and the L-phase is remaining smooth. The other reaction product is formed as grains, on which "G" is marked, in contact with the vanadium and the layered reaction product. Fig. 5.1 (b) shows the elemental distribution profile along the line from X to Y depicted in Fig. 5.1(a). The L-phase consists of approximately 80 at% V and 20 at% Si with very low content of nitrogen. Referring to the V-Si binary phase diagram [5.17], the composition corresponds to V_3Si. On the other hand, the G-phase consists of approximately 74 at% V and 26 at% N with very low content of silicon.

The V-N binary phase diagram [5.18] suggests that the composition corresponds to V_2N. Fig. 5.1 (c) shows a series of X-ray diffraction patterns which correspond to the positions (1), (2) and (3) depicted on the top of Fig. 5.1 (a). The specimen was cut at one side of the Si_3N_4 in the vicinity of its interface and ground down carefully about 1 μm for each XRD measurement. Each reaction product and its arrangement were identified by the position of each X-ray diffraction peak and the alteration of its relative intensity. All three patterns in Fig. 5.1 (c) are identified as superimposition of Si_3N_4 [5.19], V_3Si [5.20], V_2N [5.21] and V [5.22]. The appearance of all existing phases in every XRD pattern is due to the detection depth of the diffracted X-ray and the experimental error in polishing flat and parallel to the interface. However, the alteration of the relative intensity appears clearly to the peaks at 42.83° and 66.13°, which are marked with arrows (i) and (ii), respectively. The peak (i) corresponds only

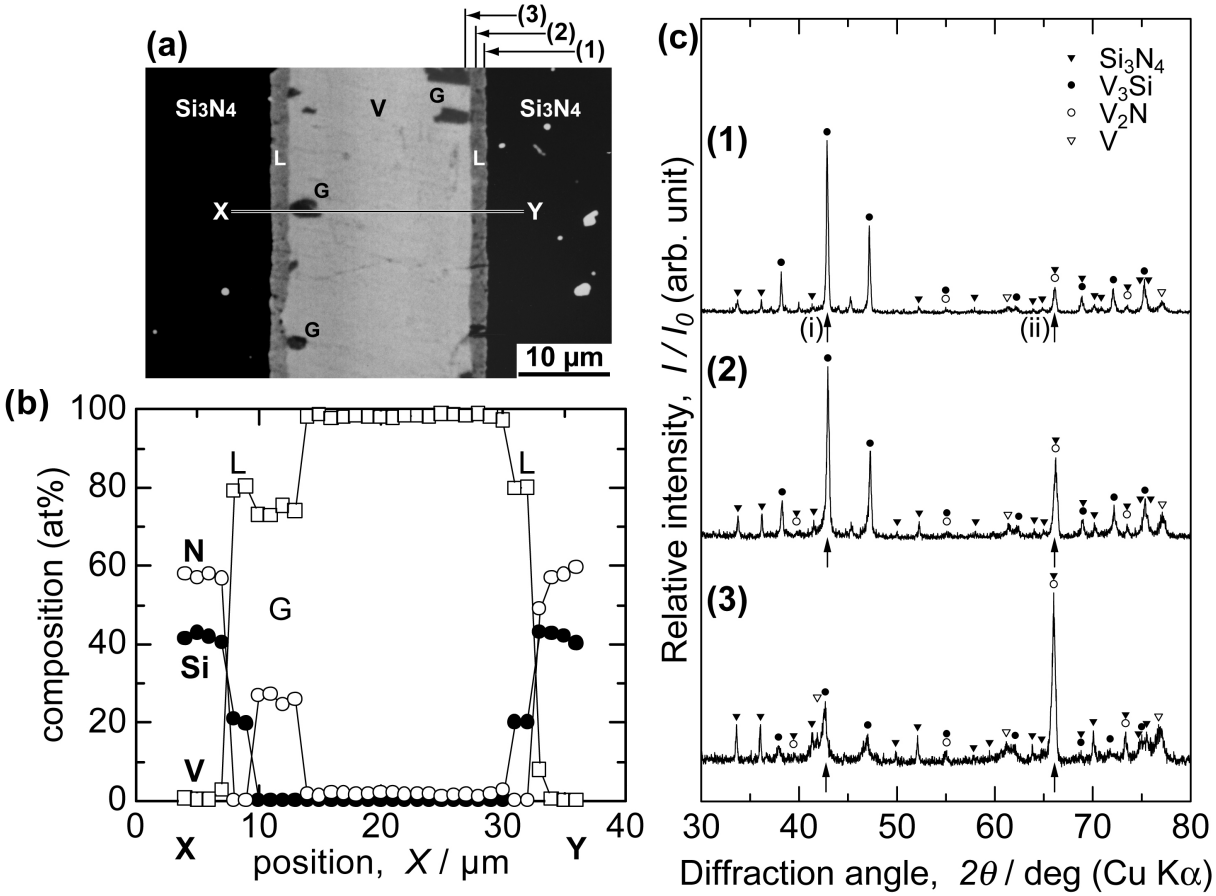

Fig. 5.1 Interfacial microstructure of the Si_3N_4 / V joint bonded at 1473 K for 3.6 ks. (a) SEM micrograph, (b) composition profile along the line from X to Y depicted in the micrograph, (c) X-ray diffraction patterns from the positions (1), (2) and (3) depicted on the top of the micrograph.

to the 210 plane of V_3Si. Compared with pattern (1), this peak keeps its intensity in pattern (2) and then it is significantly weakened in pattern (3). The peak (ii), on the other hand, corresponds to the 300 plane of V_2N. The relative intensity of the 300 peak of V_2N does not fit the standard diffraction pattern [5.21] indicating that the 100 plane of V_2N is oriented parallel to the joint interface. Although there is no peak which solely corresponds to V_2N, this orientation of V_2N clearly suggests its existence at the interface by the peak (ii). This peak is intensified in pattern (2) and is more intensified in pattern (3). This result agrees well with the EPMA analysis result depicted in Fig. 5.1 (b). Combining the results of SEM, EPMA and XRD, the L-phase and the G-phase are identified as V_3Si and V_2N, respectively. Therefore, the apparent phase sequence is finally identified as Si_3N_4 / V_3Si / V+V_2N / V.

The interfacial structure of the joints bonded in other conditions of bonding time were also analyzed in the same method. **Fig. 5.2** shows a series of SEM micrographs, which reveal four typical stages of interfacial microstructures bonded at 1473 K for different bonding time, with the result of phase identification. The bonding times for

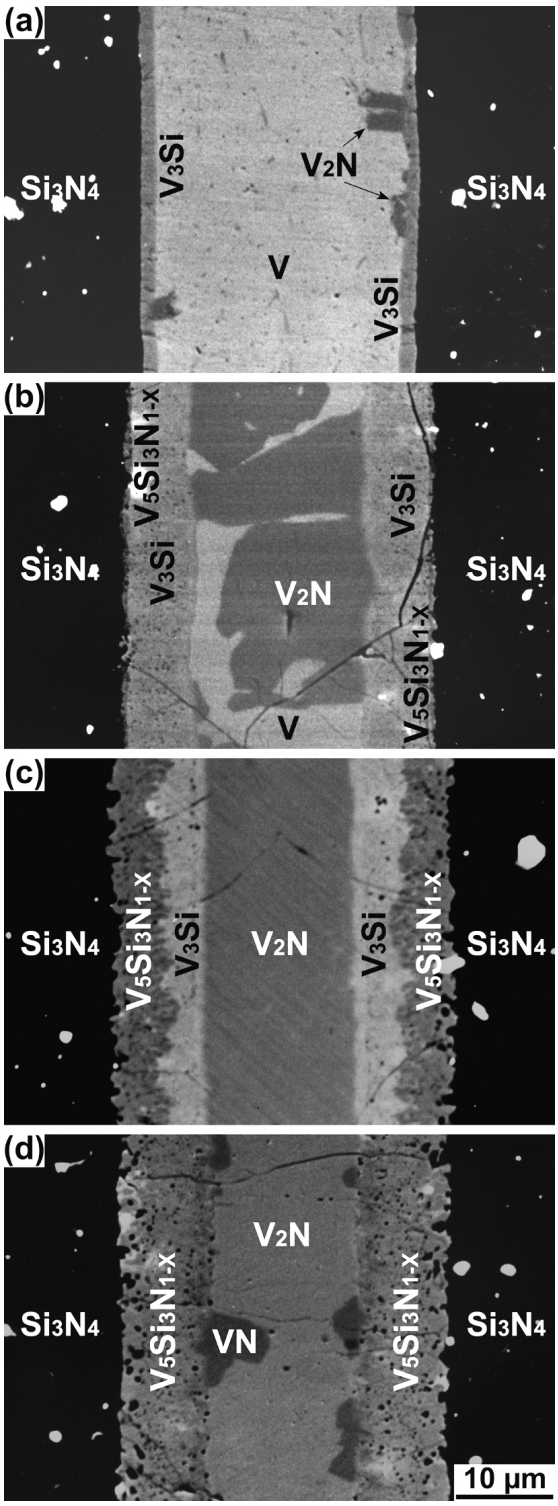

Fig. 5.2 Four representative stages of the interfacial structure bonded at 1473 K. The bonding time for each joint is (a) 3.6 ks, (b) 57.6 ks, (c) 90.0 ks and (d) 360.0 ks, respectively.

the joints depicted in Figs. 5.2 (a), (b), (c) and (d) are 3.6 ks, 57.6 ks, 90.0 ks and 360.0 ks, respectively. In the first stage shown in Fig. 5.2 (a), a layer of V_3Si adjacent to Si_3N_4 and grains of V_2N in contact with V_3Si and V are formed. In the second stage shown in Fig. 5.2 (b), $V_5Si_3N_{1-X}$ [5.14, 5.23, 5.24] is formed as a layer between Si_3N_4 and V_3Si. The Si_3N_4 / $V_5Si_3N_{1-X}$ interface becomes rough. The V_2N grains grow and contact with grains which has grown from the opposite side of the foil. Thus, the phase sequence observed at this stage is described as Si_3N_4 / $V_5Si_3N_{1-X}$ / V_3Si / V+V_2N. In the third stage shown in Fig. 5.2 (c), the V phase is annihilated. The central part of the foil is replaced with V_2N, which has become a layer. The $V_5Si_3N_{1-X}$ layer grows depredating the V_3Si layer. As the result, the thickness of the V_3Si layer decreases. The $V_5Si_3N_{1-X}$ layer contains large amount of voids, which appear with round-shaped dark contrast in the micrographs. Especially, large-sized voids are concentrated in the vicinity of the Si_3N_4 / $V_5Si_3N_{1-X}$ interface. These voids are considered to be N_2 gas phase, which is generated by the decrease of nitrogen solubility in the $V_5Si_3N_{1-X}$ during cooling. Thus, the phase sequence observed at this stage is described as Si_3N_4 / $V_5Si_3N_{1-X}$ / V_3Si / V_2N. In the fourth stage shown in Fig. 5.2 (d), the V_3Si layer is annihilated. Thus, the $V_5Si_3N_{1-X}$ layer contacts with the V_2N layer. At the $V_5Si_3N_{1-X}$ / V_2N interface, VN is newly formed as grains. The phase sequence observed at this stage is described as Si_3N_4 / $V_5Si_3N_{1-X}$ / V_2N + VN / V_2N.

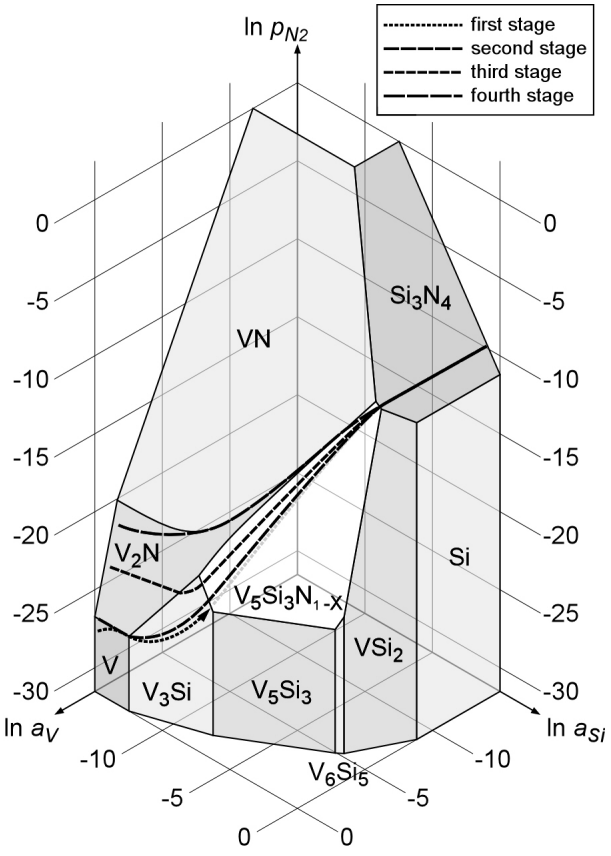

Fig. 5.3 Chemical potential diagram of V-Si-N ternary system at 1473 K. The four types of dashed lines depict the phase sequences observed at four different stages of the joint interfaces shown in Fig. 5.2.

The phase sequence observed at each stage of interfacial structure is verified with available V-Si-N ternary phase diagram [5.25]. Although the phase diagram presents only two isothermal sections at 1273 K and 1773 K, most of the observed phase

sequences are consistent with the isothermal section at 1273 K except in the following two points. One is the Si_3N_4 / V_3Si interface, which is observed at the first stage of the evolution in the interfacial microstructure. The interface requires a $V_5Si_3N_{1-X}$ layer to exist between Si_3N_4 and V_3Si, which is achieved at the second stage, to equilibrate thermodynamically. Therefore, the Si_3N_4 / V_3Si interface is considered to be in a metastable state, which is observed only at early stage of interfacial reaction. The other point is the $V_5Si_3N_{1-X}$ / VN interface, which is observed at interfaces in the fourth stage. The thermodynamic state of the $V_5Si_3N_{1-X}$ / VN interface was investigated by chemical state of the constituent elements in each phase, which is calculated standing on the thermodynamic data [5.25] and phase diagrams [5.17, 5.18, 5.25]. **Fig. 5.3** proposes the V-Si-N ternary chemical potential diagram at 1473 K. In the chemical potential diagram, $V_5Si_3N_{1-X}$ is allowed to coexist with VN. This result agrees well with another V-Si-N ternary phase diagram presented by Andruszkiewicz and Horyń [5.24]. The phase sequences observed in Fig. 5.2, except the metastable first stage, are compatibly explained with the dashed lines drawn on Fig. 5.3.

The interfacial microstructure formed at 1573 K and higher temperatures appears different in early stages of the evolution in the interfacial microstructure from that formed at low-temperatures. **Fig. 5.4** shows a series of SEM micrographs, which reveal five typical stages of interfacial microstructures bonded at 1673 K for different bonding time, with the result of phase identification. The bonding times for the joints depicted in Figs. 5.4 (a), (b), (c), (d) and (e) are 0.9 ks, 1.8 ks, 3.6 ks, 14.4 ks and 32.4 ks, respectively. In the first stage shown in Fig. 5.4 (a), a layer of V_3Si adjacent to Si_3N_4 and grains of V_2N inside the V are formed. The difference from the microstructure formed at low-temperatures is that the V_2N grains are prohibited to contact with the V_3Si layer. Thus, the phase sequence observed at this stage is described as Si_3N_4 / V_3Si / V / V+V_2N. The mechanism to prohibit the V_2N grains from contacting the V_3Si layer is discussed in the next paragraph. In the second stage shown in Fig. 5.4 (b), a layer of $V_5Si_3N_{1-X}$ is formed between Si_3N_4 and V_3Si. The V_2N grains grow larger still evading contact with the V_3Si layer. The phase sequence observed at this stage is described as Si_3N_4 / $V_5Si_3N_{1-X}$ / V_3Si / V / V+V_2N. In the third stage shown in Fig. 5.4 (c), the V is annihilated. The V_2N becomes a layer and finally contacts with the V_3Si layer. At this and the later stages, the interfacial microstructure becomes the same to each corresponding

stage at low-temperatures as shown in Figs. 5.2 (c) and (d). The phase sequence observed at the third and the fourth stages are described as Si_3N_4 / $V_5Si_3N_{1-X}$ / V_3Si / V_2N and Si_3N_4 / $V_5Si_3N_{1-X}$ / V_2N + VN / V_2N, respectively. In the fifth stage shown in Fig. 5.4 (e), the V_2N layer is annihilated. Therefore, only $V_5Si_3N_{1-X}$ and VN remain chemically stable at the final stage. The phase sequence observed at this stage is described as Si_3N_4 / $V_5Si_3N_{1-X}$ / VN.

The V_2N grains are prohibited to contact with the V_3Si layer at early stages of high bonding temperatures. The mechanism is investigated from the nature of the vanadium lying adjacent to the V_3Si layer. **Fig. 5.5** shows the detailed composition profile of silicon across the interface bonded at 1673 K for 0.3 ks in comparison with that bonded at 1473 K, 1.8 ks. Both bonding conditions form the V_3Si layer of the same thickness adjacent to Si_3N_4, which corresponds to the first stage of the evolution in the interfacial microstructure. A 0.8 μm thick zone in the vanadium adjacent to the V_3Si layer containing approximately 4 at% of silicon is detected in the joint bonded at 1673 K. The diffusion zone of silicon in the vanadium, which is named as the V(Si) zone in the following, is not formed at low-temperature

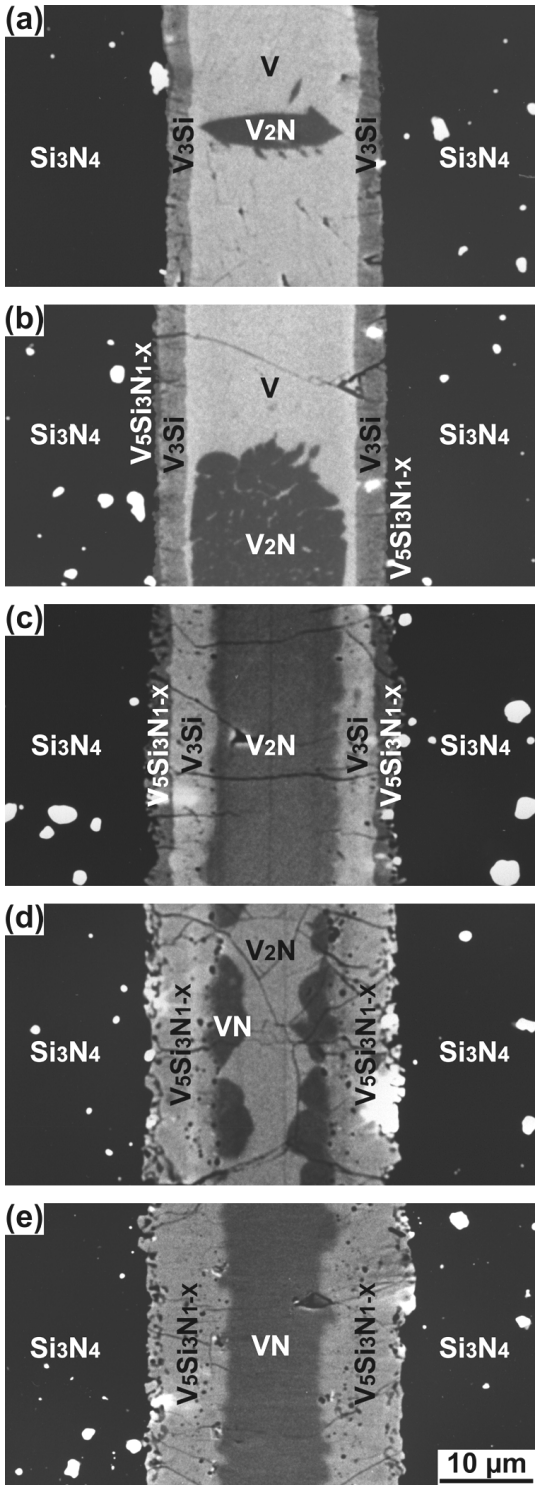

Fig. 5.4 Five representative stages of the interfacial structure bonded at 1673 K. The bonding time for each joint is (a) 0.9 ks, (b) 1.8 ks, (c) 3.6 ks, (d) 14.4 ks and (e) 32.4 ks, respectively.

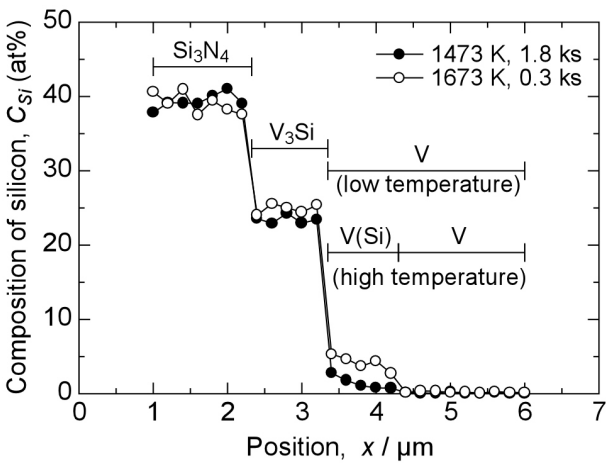

Fig. 5.5 Comparison of the composition profile of silicon across the interface of the joints bonded at 1673 K for 0.3 ks and at 1473 K for 1.8 ks.

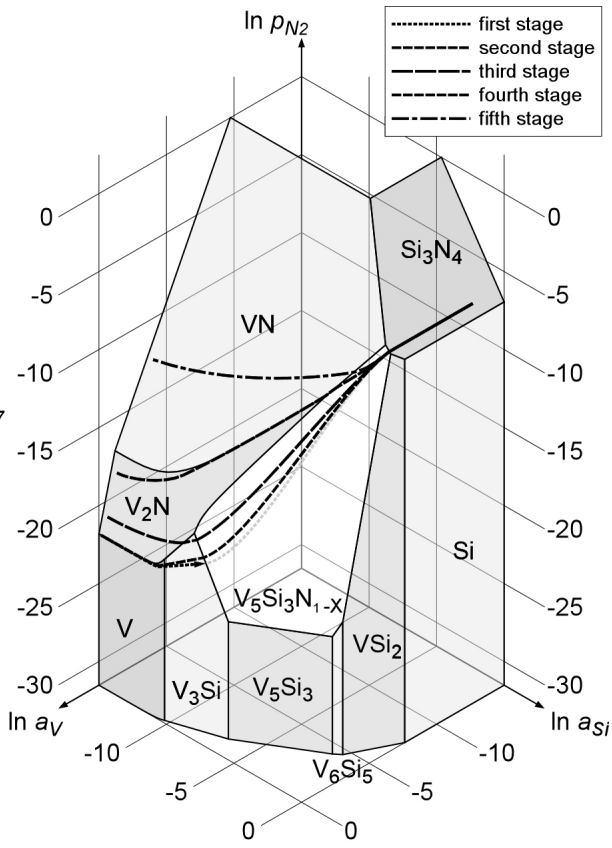

Fig. 5.6 Chemical potential diagram of V-Si-N ternary system at 1673 K. The five types of dashed lines depict the phase sequences observed at five different stages of the joint interfaces shown in Fig. 5.4.

conditions, but only at high-temperature conditions. The composition of V-4 at%Si corresponds to the solubility limit of silicon in vanadium at 1673 K [5.17]. The V-Si-N ternary phase diagram [5.24] suggests that the vanadium saturated with silicon scarcely dissolves nitrogen and that V_2N cannot coexist with such highly silicon-dissolved vanadium. Therefore, V_2N is formed inside the vanadium in which silicon is not dissolved. In other words, the V(Si) zone prohibits the V_2N grains to contact with the V_3Si layer. Therefore, the phase sequence observed at the first and the second stage at 1673 K should be corrected as Si_3N_4 / V_3Si / V(Si) / V+V_2N and Si_3N_4 / $V_5Si_3N_{1-X}$ / V_3Si / V(Si) / V+V_2N, respectively. This result implies that the interfacial energy of the V_3Si / V is reduced by the formation of the V(Si) zone to a level lower than that of the V_3Si / V_2N. **Fig. 5.6** shows the V-Si-N ternary chemical potential diagram at 1673 K. The phase sequences observed in Fig. 5.4, except the metastable first stage, are consistent with the dashed lines drawn on Fig. 5.6.

Schuster *et al*. [5.14] has described the phase sequence of the Si_3N_4 / V system at 1273 K

to be Si_3N_4 / V_2N / V_3Si ($V_5Si_3N_{1-X}$) / V, which is completely different from the present result. Their prediction stands on the assumption that the interfacial reaction proceeds by the diffusion of silicon from Si_3N_4 to the metal to form metal silicide followed by the reaction of the metal with the free nitrogen to binary metal nitrides on the Si_3N_4 side. Although the V(Si) zone is observed at high-temperatures, the present result at the earliest stage of interfacial reaction showing a V_3Si layer adjacent to Si_3N_4 strongly suggests that the growth of the silicide layers is controlled by diffusion of vanadium instead of silicon through the silicide layers, as depicted on Figs. 5.2 and 5.6 with arrows on the phase sequences of the first stages. This conclusion is also derived from the morphology of the V_3Si / V + V_2N interface which is observed in early stages of low-temperature bonding condition. The V_3Si layer has two different interfaces on the metal side. One is the interface with the V and the other is that with the V_2N grains. Although two different phases contact with the V_3Si layer, the thickness of the layer does not appear different by the difference of the contacting phases. Furthermore, the V_3Si layer grows without embedding V_2N grains at their original positions. This fact indicates that the growth front of the V_3Si layer is not located on the metal side but on the Si_3N_4 side of the layer. It is important to understand the growth front correctly, because it determines the element dominating the reaction behavior at the interface.

C. Growth Behavior of the Reaction Products

In every bonding condition employed in the present study, no other phases than V_3Si, $V_5Si_3N_{1-X}$, V_2N and VN are formed at the interfaces. V_3Si and $V_5Si_3N_{1-X}$ appear as layers from the early stage of their formation, while V_2N and VN appear as grains at their rudiment and then grow to form a layer. In order to estimate the amount of formed grains of V_2N and VN, a representative size of each phase (w_i) was defined as

$$w_i = A_i / 2\,l\,, \tag{5.1}$$

where A_i is the observed total area of each phase and l is the observed length of the interface. This parameter keeps compatibility with the thickness, the size parameter when each phase achieves the formation of its layer.

The increase and decrease behavior in the thickness or size of each reaction product interacts with each other. **Fig. 5.7** shows the growth behavior of each reaction product at 1473

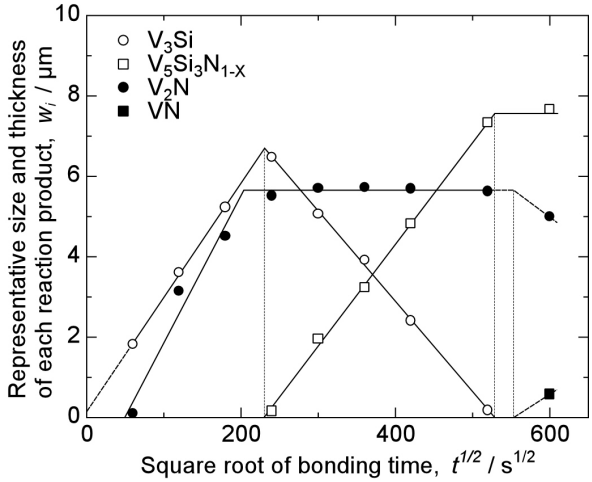

Fig. 5.7 Growth behavior of each reaction product at 1473 K.

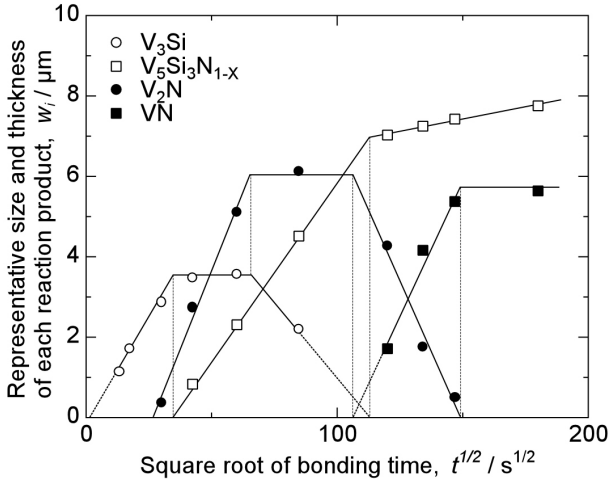

Fig. 5.8 Growth behavior of each reaction product at 1673 K.

K. The representing size and the thickness of each reaction product are plotted as a function of the square root of bonding time ($t^{1/2}$). It is clearly shown that V_3Si, V_2N and $V_5Si_3N_{1-X}$ grow proportionately with the square root of bonding time, obeying the parabolic law, in its initial stage of growth. Only V_3Si appears without showing any latency period. The thickness of the V_3Si layer increases until the $V_5Si_3N_{1-X}$ layer is formed. The formation and growth of the $V_5Si_3N_{1-X}$ layer forces the V_3Si layer annihilate. The growth rate of the $V_5Si_3N_{1-X}$ layer is retained until it comes into contact with the V_2N by the annihilation of the V_3Si layer. Then, the growth is slowed down. The V_2N grains grow until the grains grown from both sides of the foil contact to each other. It keeps its representative size of 5.65 μm until the VN grains are formed. The VN grows reducing the thickness of the V_2N layer. **Fig. 5.8** shows the growth behavior of each reaction product at 1673 K. It is clearly noticed that every reaction product grows obeying the parabolic law in its initial stage of growth also at this temperature. The V_3Si layer increases its thickness until the $V_5Si_3N_{1-X}$ layer is formed. In contrast with the behavior at low-temperatures, the layer does not decrease its thickness by the formation of the $V_5Si_3N_{1-X}$ layer, but keeps its thickness of 3.55 μm until the V_3Si layer contacts with the V_2N layer. The formation of the V_3Si / V_2N interface, which indicates the annihilation of the V phase, also stops the parabolic growth of the V_2N. The V_2N layer maintains its thickness of 6.04 μm until the VN grains are formed. The annihilation of the V_3Si layer results in the suppression of the growth of the $V_5Si_3N_{1-X}$ layer. On the other hand, the annihilation of the

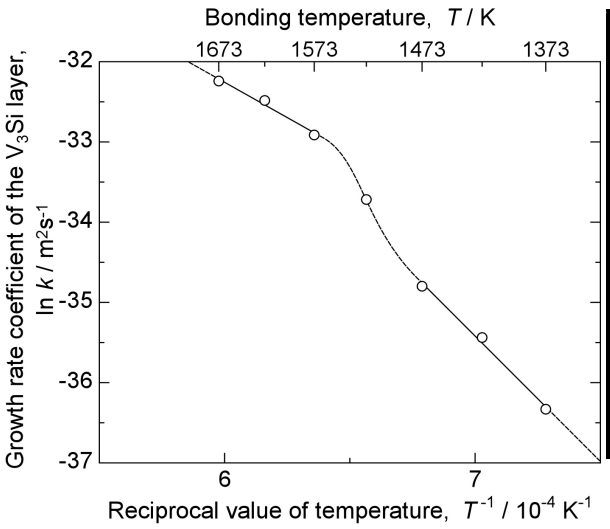

Fig. 5.9 Arrhenius plot of the growth rate coefficient of the V_3Si layer.

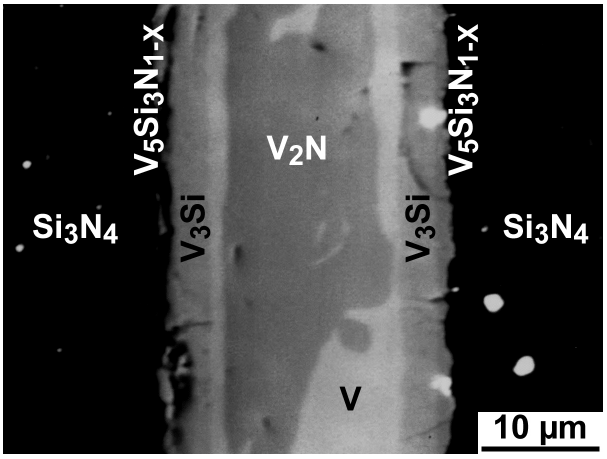

Fig. 5.10 Interfacial microstructure of a Si_3N_4 / V joint bonded at 1498 K for 3.6 ks.

V_2N layer stops the growth of the VN. The interaction of the growth behavior of each reaction product is summarized as follows: the V_3Si layer stops its parabolic growth when the $V_5Si_3N_{1-X}$ layer is formed. The reduction in its thickness starts when it contacts to the V_2N. The $V_5Si_3N_{1-X}$ layer slows down its growth by contacting to the V_2N, which corresponds to the annihilation of the V_3Si layer. The V_2N stops its parabolic growth when the contacting to the V_3Si layer and the contacting of the grains grown from both sides each other are both achieved. The reduction in its representative size starts by the formation of the VN grains. The VN stops its parabolic growth when the V_2N is annihilated.

The change in the thickness of the V_3Si layer is observed to be sensitively affected by the behavior of the V_2N phase. As discussed in the last section, whether the V_2N contacts with the V_3Si layer is determined by the formation of a thin V(Si) zone at the V_3Si / V interface. Since silicon can diffuse into vanadium from the beginning of the bonding treatment at high-temperature conditions, the V(Si) zone can affect the growth behavior of the V_3Si layer even in its initial stage of parabolic growth. **Fig. 5.9** shows the dependence of the growth rate coefficient of the V_3Si layer (k) on the bonding temperature regarding the Arrhenius-type function

$$\ln k = \ln k_0 - Q / RT, \tag{5.2}$$

where k_0 is the pre-exponential factor for the growth rate of the V_3Si layer, Q is the apparent activation energy for the growth of the V_3Si layer, R is the gas constant and T is the bonding

temperature. The dependence of the growth rate on the bonding temperature for the low-temperature bonding condition appears with different line from that for the high-temperature bonding condition revealing a transition-temperature range between 1473 K and 1573 K. The interfacial microstructure of the joints bonded at temperatures in this transition-temperature range shows that the V_2N grains are formed off the V_3Si layer even at 1498 K (**Fig. 5.10**). This result indicates that the V(Si) zone starts its formation at the onset temperature of the transition observed in Fig. 5.9. The values of k_0 and Q for the low- and the high-temperature bonding condition calculated from Fig. 5.9 are listed in **Table 5.2**. The activation energy for the growth of the V_3Si layer at high-temperature bonding condition appears lower than that at low-temperature bonding condition. This result suggests that the formation of the V(Si) zone adjacent to V_3Si reduces the activation energy of the growth of the V_3Si layer. As discussed in the previous section, the growth of the V_3Si layer is controlled by the diffusion of vanadium through the layer, and the V(Si) zone reduces the interfacial energy of the V_3Si / V phase boundary to a level lower than that of the V_3Si / V_2N. These results support the consideration that the V(Si) zone improves the diffusion of vanadium in the V_3Si layer by reducing the activation energy for dissolution of vanadium into V_3Si. Therefore, the apparent activation energy for the growth of the V_3Si layer corresponds to that for the dissolution of vanadium into the V_3Si layer.

Table 5.2 A list of the pre-exponential factor for the growth rate and the apparent activation energy for the growth of the V_3Si layer at each temperature range.

Temperature range, T / K	Pre-exponential factor for the growth rate, k_0 / m^2s^{-1}	Apparent activation energy for the growth, Q / kJ mol^{-1}
1373 - 1473	1.30×10^{-6}	260
1573 - 1673	3.66×10^{-10}	146

Figs. 5.7 and 5.8 indicate that the V_3Si layer grows up to 6.70 μm before the $V_5Si_3N_{1-X}$ layer is formed at the bonding temperature of 1473 K, while it does up to 3.55 μm at 1673 K. This result indicates that the Si_3N_4 / V_3Si interface is more stable at lower temperatures. Since the Si_3N_4 / V_3Si interface is thermodynamically metastable, sufficient amount of vanadium is supplied to the interface to form V_3Si adjacent to Si_3N_4 in the first stage of interfacial reaction. Therefore, the formation of the $V_5Si_3N_{1-X}$ layer starts when the diffusion flux of vanadium in the V_3Si layer is reduced below a certain level by increasing the thickness of the V_3Si layer.

The diffusion flux of vanadium through the V_3Si layer (J_V) is determined regarding to the Fick's first law:

$$J_V = -D_V (\partial C_V / \partial x) , \tag{5.3}$$

where D_V and $\partial C_V/\partial x$ are the diffusion coefficient of vanadium through V_3Si and the spatial composition gradient of vanadium in the V_3Si layer, respectively. As shown in Fig. 5.1(b), however, the composition of vanadium in the V_3Si layer is almost uniform. Thus, the diffusion cannot be driven by the composition gradient. Since the diffusion of an element is caused by the gradient of the chemical potential, to replace the composition (C_V) with the activity of vanadium (a_V) will explain the diffusion more correctly. Thus, the equation (5.3) can be modified as

$$J_V = -D_V \frac{\partial a_V}{\partial x} = -D_V \frac{\partial \exp(\mu_V / RT)}{\partial x} = -\frac{D_V}{RT} \exp\left(\frac{\mu_V}{RT}\right) \frac{\partial \mu_V}{\partial x} \tag{5.4}$$

in the isothermal condition, where μ_V is the chemical potential of vanadium. The equation (5.4) indicates that the diffusion flux depends proportionately on the spatial gradient of the chemical potential of vanadium ($\partial \mu_V/\partial x$). The value of $\partial \mu_V/\partial x$ was roughly estimated by dividing the difference in the chemical potential of vanadium at the Si_3N_4 / V_3Si and the V_3Si / V+V_2N interfaces ($\Delta \mu_V$) with the observed critical thickness of the V_3Si layer for the formation of the $V_5Si_3N_{1-X}$ layer (w_{V3Si}*). The calculation of $\Delta \mu_V / w_{V3Si}$* for the bonding temperatures of 1473 K and 1673 K deduces -3.36×10^9 and -3.31×10^9 J mol^{-1} m^{-1}, respectively. Both values appears almost the same. This result suggests that the $V_5Si_3N_{1-X}$ layer is formed to establish the local equilibrium at the interface with Si_3N_4 when the spatial gradient of the chemical potential of vanadium in the V_3Si layer decreases to a value below -3.3×10^9 J mol^{-1} m^{-1}, being

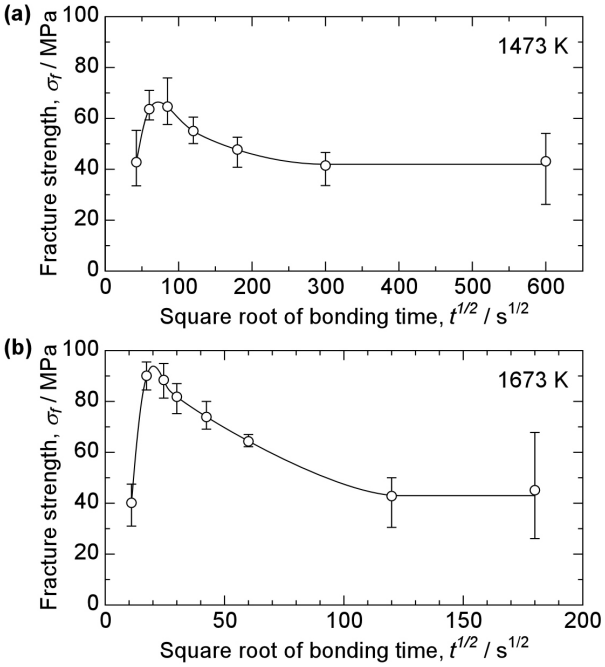

Fig. 5.11 Dependence of the fracture strength of the Si_3N_4 / V joints on the bonding time. (a) bonded at 1473 K, (b) at 1673 K.

independent on the bonding temperature, by increasing the thickness of the V_3Si layer.

D. Joint Strength and Fracture

The fracture strength of the joints changes depending on the bonding time. **Figs. 5.11** (a) and (b) depict the dependence of the fracture strength on the bonding time for the joints bonded at 1473 K and 1673 K, respectively. The fracture strength of the joints bonded at 1473 K is improved until the bonding time of 5.2 ks, at which the maximum average-strength of 67 MPa is obtained. Referring to Fig. 5.7, the bonding condition of 1473 K for 5.2 ks corresponds to the formation of a 2.0 μm-thick V_3Si layer adjacent to Si_3N_4. The prolonged bonding time over 5.2 ks gradually reduces the fracture strength down to 42 MPa. The fracture strength of the joints bonded at 1673 K is increased until the bonding time of 0.4 ks, at which the maximum average-strength of 94 MPa is obtained. The bonding condition of 1673 K for 0.4 ks corresponds to the formation of a 2.0 μm-thick V_3Si layer adjacent to Si_3N_4. The prolonged bonding time over 0.4 ks gradually reduces the fracture strength down to 43 MPa and significantly expands the scatter in the data.

Fig. 5.12 shows a pair of SEM micrographs and corresponding XRD patterns taken from both sides of the fracture surfaces of a joint bonded at 1473 K for 3.6 ks, at which the strong joint of 64 MPa was obtained. Both fracture surfaces appear flat, indicating that the fracture occurs at the interface

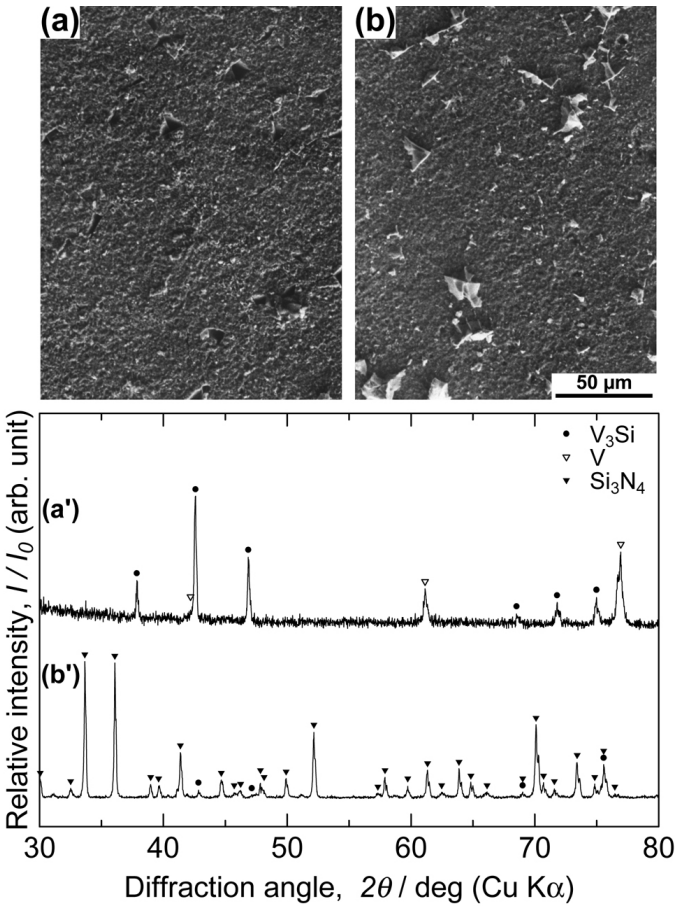

Fig. 5.12 SEM micrographs and corresponding XRD patterns taken from both sides of the fracture surfaces of a joint bonded at 1473 K for 3.6 ks. (a) and (a') were taken from the V side, (b) and (b') from the Si_3N_4 side.

in a brittle mode. The side on which the vanadium foil is remaining is named the "V side", while the other side is named as the "Si_3N_4 side". On the V-side surface (Fig. 5.12 (a)), only V_3Si is detected, on which pits are dispersed. The XRD pattern taken from the V side (Fig. 5.12 (a')), in which only V_3Si and V are detected, agrees with this analysis result. Corresponding to the pits on the V-side surface, sharp-edged particles of V_3Si are observed on the Si_3N_4-side surface (Fig. 5.12 (b)). In agreement with the EPMA, the XRD pattern taken from the Si_3N_4 side (Fig. 5.12 (b')) indicates that Si_3N_4 and small amount of V_3Si exists on the surface. Based on these results, the fracture is determined to occur mainly at the Si_3N_4 / V_3Si interface and partly inside the V_3Si layer. **Fig. 5.13** shows a pair of XRD patterns taken from a joint bonded at 1473 K for 360.0 ks, at which the joint strength is reduced to 43 MPa. The XRD pattern taken from the V side (Fig. 5.13 (a)) indicates the existence of Si_3N_4 and $V_5Si_3N_{1-X}$ on the surface. However, Si_3N_4 is observed only at the areas where the insert foil has been chipped off. Thus, the peaks of Si_3N_4 in the pattern are originated from the counterpart of the joint. On the other hand, Si_3N_4 and $V_5Si_3N_{1-X}$ are detected in the XRD pattern taken from the Si_3N_4 side (Fig. 5.13 (b)). Therefore, the fracture is determined to occur at the $V_5Si_3N_{1-X}$ in the vicinity of the Si_3N_4 / $V_5Si_3N_{1-X}$ interface. The analysis of the fractured surfaces of the joints bonded at 1673 K results in the same conclusion as that of 1473 K: the high-strength joints are fractured at the Si_3N_4 / V_3Si interface and the joints bonded with the prolonged bonding time are fractured at the $V_5Si_3N_{1-X}$ in the vicinity of the Si_3N_4 / $V_5Si_3N_{1-X}$ interface.

The maximum fracture strength is achieved when the thickness of the V_3Si layer is 2.0 μm. Ito *et al.* [5.15], also, have reported the formation of a 2 μm-thick V_3Si layer adjacent to Si_3N_4 at the optimum bonding condition. **Fig. 5.14** shows the relation between the average fracture strength and the thickness of the V_3Si layer. In every bonding temperature between 1373 K and

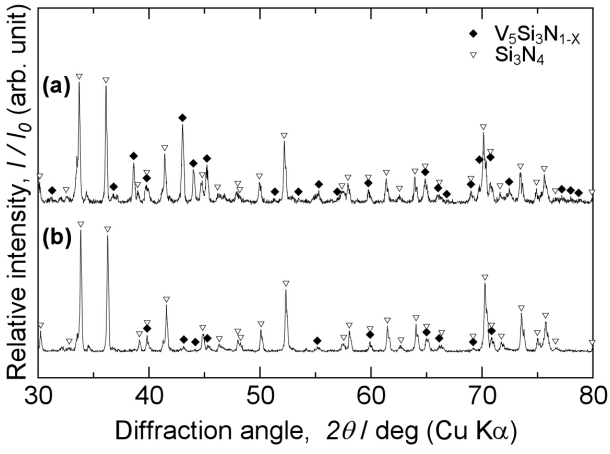

Fig. 5.13 XRD patterns taken from both sides of the fracture surfaces of a joint bonded at 1473 K for 360.0 ks. (a) the V side, (b) the Si_3N_4 side.

1673 K, the maximum fracture strength is obtained when the thickness of the V_3Si layer is 2.0 μm, regardless of the bonding temperature. In addition, the higher bonding temperature leads to the higher maximum fracture strength. The improvement and deterioration behavior of the fracture strength without the formation of the $V_5Si_3N_{1-X}$ layer is considered to be the competition process of the following two factors. One is the improvement in the fracture strength, explained by the chemical-bond formation process in atomic scale at the Si_3N_4 / V contact area and by the plastic deformation of the vanadium foil to expand the contact area. Since the yield strength of vanadium is lower at higher temperatures, the fraction of contact area in atomic scale becomes larger at higher temperatures to increase the maximum fracture strength. The other factor is the deterioration of the fracture strength, explained by the magnitude of the thermal residual stress as a function of the thickness of the V_3Si layer, especially that concentrated at the edge of the bond interface. Although the mismatch of the thermal expansion coefficient for the Si_3N_4 / V_3Si interface is reported [5.14], the yield strength and the elastic modulus of V_3Si as functions of the temperature are not found in the literature, which are necessary for the estimation of the magnitude of the thermal residual stress.

The $V_5Si_3N_{1-X}$ layer is formed at the interface of the joints bonded with the prolonged bonding time. The average fracture strength of such joints converges to a value of approximately 42 MPa, being insensitive to the bonding temperature. The fracture of such joints occurs at the Si_3N_4 / $V_5Si_3N_{1-X}$ interface, which corresponds to the position where the segregation of large-sized voids is observed as shown in Figs. 5.2 and 5.4. Therefore, the fracture is considered to occur by crack propagation connecting these voids. Since the voids are the N_2 gas formed during cooling, the fracture property of the joints at this state of interfacial microstructure is sensitive to the behavior of nitrogen. For

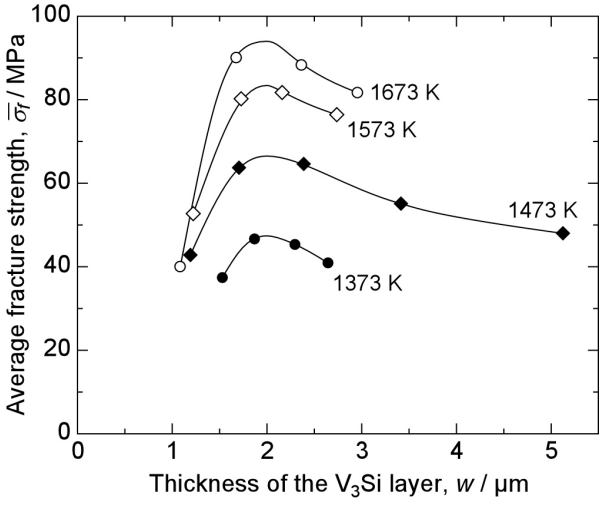

Fig. 5.14 Relation between the average fracture strength and the thickness of the V_3Si layer.

example, regarding to Figs. 5.7, 5.8 and 5.11, the scatter of the fracture strength expands when the $V_5Si_3N_{1-X}$ contacts with the V_2N. This change in the microstructure will affect the formation and segregation behavior of the voids.

The results described in this section indicates that the formation of the 2.0 μm-thick V_3Si layer adjacent to Si_3N_4 is required to obtain the maximum average strength of the Si_3N_4 / V joints. In addition, higher bonding temperature leads to the higher maximum strength. However, the Si_3N_4 / V_3Si interface is a metastable state. The V_3Si layer is allowed to grow up to 3.55 μm at the bonding temperature of 1673 K, as described in Fig. 5.8, and will be lesser at higher temperatures. Therefore, the bonding temperatures which does not allow the V_3Si layer to grow thicker than 2.0 μm is considered to be inadequate.

IV. Summary

Si_3N_4 was bonded to vanadium foils by solid state diffusion bonding. The interfacial microstructure and reaction kinetics were analyzed in detail by means of SEM, EPMA and XRD. The strength of the joints was estimated by a shear fracture test. The following points were clarified.

1) The interfacial phase sequence of the Si_3N_4 / V joints bonded at 1473 K and below changes revealing four stages of transition as follows: (i) Si_3N_4 / V_3Si / V+V_2N / V, (ii) Si_3N_4 / $V_5Si_3N_{1-X}$ / V_3Si / V+V_2N, (iii) Si_3N_4 / $V_5Si_3N_{1-X}$ / V_3Si / V_2N, and (iv) Si_3N_4 / $V_5Si_3N_{1-X}$ / V_2N + VN / V_2N. At the bonding temperatures of 1498 K and higher, the V_2N grains are prohibited to contact with the V_3Si layer by the V(Si) zone. At these temperatures, five stages of transition in the interfacial phase sequence are observed as follows: (i) Si_3N_4 / V_3Si / V(Si) / V+V_2N, (ii) Si_3N_4 / $V_5Si_3N_{1-X}$ / V_3Si / V(Si) / V+V_2N, (iii) Si_3N_4 / $V_5Si_3N_{1-X}$ / V_3Si / V_2N, (iv) Si_3N_4 / $V_5Si_3N_{1-X}$ / V_2N + VN / V_2N, and (v) Si_3N_4 / $V_5Si_3N_{1-X}$ / VN. The Si_3N_4 / V_3Si interface observed in the first stage is metastable. These phase sequences except the metastable interface are successfully expressed on the proposed chemical potential diagram.
2) The growth front of the V_3Si layer is located on the Si_3N_4 side, indicating that the diffusion of vanadium through the V_3Si layer dominates the growth of the layer.
3) The increase and decrease behavior in the thickness of each reaction product interacts

with each other. Every reaction product grows obeying the parabolic law in its initial stage of growth. The pre-exponential growth constant and the activation energy for the growth of the V_3Si layer appear different between the high- and low-temperature bonding conditions. The formation of the $V_5Si_3N_{1-X}$ layer starts when the spatial gradient of the chemical potential of vanadium in the V_3Si layer decreases to a value below -3.3×10^9 J mol^{-1} m^{-1} by the growth of the V_3Si layer.

4) The maximum fracture strength is achieved when the thickness of the V_3Si layer is 2.0 μm. The higher bonding temperature leads to the higher maximum fracture strength. The fracture of the joints bonded at this condition occurs in a brittle mode mainly at the Si_3N_4 / V_3Si interface and partly inside the V_3Si layer. The prolonged bonding time gradually reduces the fracture strength down to 42 MPa. The joints are fractured at the $V_5Si_3N_{1-X}$ in the vicinity of the Si_3N_4 / $V_5Si_3N_{1-X}$ interface by crack propagation connecting the voids.

References

[5.1] R.F. Mattas and M.C. Billone: *J. Nucl. Mater.*, 1996, Vol. 233-237, pp. 72-81.

[5.2] D.L. Smith, M.C. Billone, S. Majumdar, R.F. Mattas and D.-K. Sze: *J. Nucl. Mater.*, 1998, Vol. 258-263, pp. 65-73.

[5.3] D.L. Smith, M.C. Billone and K. Natesan: *Int. J. Refractory Met. & Hard Mater.*, 2000, Vol. 18, pp. 213-224.

[5.4] D.L. Smith, J.-H. Park, I. Lyublinski, V. Evtikhin, A. Perujo, H. Glassbrenner, T. Terai and S. Zinkle: *Fusion Eng. and Design*, 2002, Vol. 61-62, pp. 629-641.

[5.5] Y. Nemoto, K. Ueda, M. Satou, A. Hasegawa and K. Abe: *J. Nucl. Mater.*, 1998, Vol. 258-263, pp. 1517-1522.

[5.6] R. Yasuda, M. Satou, A. Hasegawa and K. Abe: *J. Nucl. Mater.*, 1998, Vol. 258-263, pp. 1528-1532.

[5.7] F.W. Clinard, Jr., G.F. Hurley and R.W. Klaffky: *Res Mechanica*, 1983, Vol. 8, pp. 207-234.

[5.8] F. L. Riley: *ENCYCLOPEDIA OF MATERIALS SCIENCE AND ENGINEERING*, M. B. Bever (Editor-in-Chief), Pergamon Press, 1986, Vol. 6, pp. 4412-4415.

[5.9] H. Mori, T. Sakata, H. Yasuda and M. Maeda: *J. Vac. Sci. Tech. B*, 1994, Vol. 12, pp.

2376-2379.

[5.10] Y. Nakao, K. Nishimoto and K. Saida: *Trans. Jpn. Weld. Soc.*, 1989, Vol. 20, pp. 66-76.

[5.11] Y. Morizono, T. Nakata, M. Nishida and A. Chiba: *J. Ceram. Soc. Jpn.*, 1995, Vol. 103, pp. 810-815, in Japanese.

[5.12] S.D. Peteves, M. Paulasto, G. Ceccone and V. Stamos: *Acta Mater.*, 1998, Vol. 46, pp. 2407-2414.

[5.13] P. Lamparter, S. Steeb and A. Gukelberger: *High Temperatures – High Pressures*, 1971, Vol. 3, pp. 727-740.

[5.14] J. C. Schuster, F. Weitzer, J. Bauer and H. Nowotny: *Mater. Sci. Eng.*, 1988, Vol. A105/106, pp. 201-206.

[5.15] Y. Ito, K. Kitamura and M. Kanno: *J. Mater. Sci.*, 1993, Vol. 28, pp. 5014-5018.

[5.16] I. Gotman and E.Y. Gutmanas: *Acta Metall. Mater.*, 1992, Vol. 40, Suppl., pp. S121-S131.

[5.17] *Binary Alloy Phase Diagrams*, T.B. Massalski (Editor-in-Chief), ASM International, 1986, pp. 2060-2062.

[5.18] *Binary Alloy Phase Diagrams*, T.B. Massalski (Editor-in-Chief), ASM International, 1986, pp. 1656-1659.

[5.19] *Powder Diffraction File*, JCPDS–ICDD, 33-1160.

[5.20] *Powder Diffraction File*, JCPDS–ICDD, 19-1405.

[5.21] *Powder Diffraction File*, JCPDS–ICDD, 32-1413.

[5.22] *Powder Diffraction File*, JCPDS–ICDD, 22-1058.

[5.23] *Powder Diffraction File*, JCPDS–ICDD, 40-956.

[5.24] R. Andruszkiewicz and R. Horyń: *J. Less-Common Met.*, 1986, Vol. 124, pp. 205-210.

[5.25] *Phase Diagrams of Ternary Boron Nitride and Silicon Nitride Systems*, P. Rogl and J.C. Schuster (Eds.), ASM International, Materials Park, Ohio (USA), 1992, pp. 205-207.

Chapter 6 Solid State Diffusion Bonding of Silicon Nitride using Niobium Foils

This chapter presents a way to control the interfacial microstructure of the solid state diffusion bonded joints of silicon nitride (Si_3N_4) using niobium foils. The interfacial microstructure and its evolution behavior were analyzed with an SEM, EPMA and XRD. The interfacial phase sequence is Si_3N_4 / $Nb_5Si_3N_{1-X}$ / Nb_5Si_3 / Nb_2N + Nb / Nb. The phase sequence does not change within the bonding temperature and time ranging from 1573 K to 1773 K and from 0.9 ks and 32.4 ks, respectively. The reaction products grow monotonously obeying the parabolic law. The maximum fracture strength of 131 MPa was obtained with the joints bonded at 1573 K for 14.4 ks. The fracture occurs at the Si_3N_4 / $Nb_5Si_3N_{1-X}$ interface in a brittle mode. To improve the joint strength, the effect of initial grain size of the niobium insert was investigated. The interfacial microstructure of the joints bonded using fine-grained films appears with the phase sequence of Si_3N_4 / $Nb_5Si_3N_{1-X}$ / Nb_5Si_3 / Nb_2N / Nb+Nb_2N, which is different from those bonded using ordinary polycrystalline foils or single-crystal foils. The joints bonded using deposited films of niobium retain high fracture-strength of 100 MPa even after a prolonged bonding treatment of 57.6 ks at 1673 K.

I. Introduction

In the previous chapters 4 and 5, the evolution behavior of the interfacial microstructure of solid state diffusion bonded silicon nitride using titanium and vanadium foils in relation with the joint strength, and a way to control the microstructure regarding to the chemical potential diagrams to reveal the highest performance of the joints with these insert metals have been described. The joints of Si_3N_4 using titanium inserts are, however, weak even in

their optimum state of the microstructure. The deterioration of the joint strength occurs by the formation of brittle Ti_5Si_3 layer adjacent to Si_3N_4. On the other hand, the joints using vanadium inserts perform a good strength at their optimum state of the interfacial microstructure. Since the optimum state is metastable, however, the change in the interfacial microstructure during the operation of the joint-components will deteriorate the strength. To increase and stabilize the joint strength in a higher level, the insert metal should be noble enough to avoid the formation of brittle phases. In addition, a sufficient reactivity with nitrogen to prevent the N_2-void formation is also required.

Niobium is one of the most useful refractory materials, which melting point is high (2741 K) and thermal expansion coefficient is low (7.07×10^{-6} K^{-1}). In addition, niobium is known as an active element for ceramics brazing [6.1-6.3]. Especially, it forms a strong bond with alumina (Al_2O_3) with a minimized thermal residual stress and without formation of any reaction product. Because of these excellent features of Al_2O_3 / Nb joints, the interface has been intensively investigated by many researchers [6.4-6.13]. On the other hand, Al_2O_3 is commonly used as one of the sintering agents for Si_3N_4. Thus, these properties of niobium are expected to be adequate to form a strong bond also with silicon nitride. However, there are very few reports dealing with the bonding of Si_3N_4 with niobium [6.14, 6.15].

The purpose of the present study is to clarify the interfacial interaction between silicon nitride and niobium, focusing on the following two points: the behavior of the microstructural evolution at the interface during solid state diffusion bonding and the relation between the interfacial microstructure and the joint strength. Based on the results of them, a way to control the interfacial structure is proposed.

II. Experimental Procedure

Si_3N_4 specimens were prepared from pressureless sintered columnar rods, which diameter and length were 6.0 mm and 40.0 mm, respectively. They contained a few mass percentages of alumina (Al_2O_3), yttria (Y_2O_3) and tungsten di-silicide (WSi_2) as the sintering agents. The rods were cut to a length of 4.0 mm. Their surface to be bonded was polished with 3 μm diamond paste. Roughness of the obtained surface was about 0.032 μm. On the other hand, 99.5 % nominally-pure niobium foils with two different thickness, 25.4 μm and

100 μm, were used as the insert metal. Both sides of the niobium surfaces were polished with 0.3 μm alumina suspension just before the bonding treatment in order to minimize the surface scale formation. The surface roughness of the foils was about 0.100 μm.

Two Si_3N_4 specimens and a niobium foil were used for each bonding experiment. They were first cleaned in an ultrasonic bath with acetone. Then, the niobium foil was inserted between two Si_3N_4 specimens and they were set into an induction-heating vacuum furnace. The bonding temperature and time were ranging from 1473 K to 1773 K and from 0.9 ks to 32.4 ks, respectively. The heating and cooling rate were set to 0.60 Ks^{-1} and 0.28 Ks^{-1}, respectively. The vacuum inside the furnace was kept below 1.3×10^{-3} Pa. Uniaxial pressure of 140 MPa, perpendicular to the bonding interface, was applied to the specimen throughout the bonding treatment.

The interfacial microstructure of the joints was analyzed by the combination of scanning electron microscopy (SEM), wavelength-dispersive electron probe microanalysis (WDS-EPMA) and X-ray diffractometry (XRD). The quantitative composition measurement by EPMA was implemented utilizing ZAF correction program. The joint strength was estimated by shear fracture testing. Fracture test was implemented with cross-head speed of 1.67×10^{-5} m s^{-1} at ambient temperature and atmosphere. Seven samples were tested for each bonding condition. The fracture surfaces were analyzed with the SEM, WDS-EPMA and XRD.

III. Results and Discussion

A. Bondability

With some combinations of bonding temperature and time, solid state diffusion bonding experiment fails to obtain joints of Si_3N_4. The bondability at each employed bonding condition is listed on **Table 6.1**. In the table, "S" means that the bonding at the condition succeeds, while "F" means that it fails. At bonding temperature of 1473 K,

Table 6.1 Bondability at each employed combination of temperature and time.

Bonding time, *t* / ks	Bonding temperature, *T* / K			
	1473	1573	1673	1773
0.9		F	S	
3.6	F	S	S	S
14.4	F	S	S	S
32.4	F	S	S	S
57.6			S	
90.0			S	

every bonding experiment turned out to be unsuccessful. However, at bonding temperature of 1573 K, the bonding is succeeded with bonding time of 3.6 ks or longer. At the higher bonding temperature of 1673 K and 1773 K, the bonding time of 0.9 ks is enough to obtain joints. This result agrees well with that reported by Suganuma *et al.* [6.14], which has shown that the Si_3N_4 / Nb couples cannot be bonded below 1573 K under the bonding pressure and time of 100 MPa and 1.8 ks, respectively.

B. Interfacial Microstructure of Si_3N_4 / Nb Joints

Fig. 6.1 shows the interfacial microstructure of a joint bonded at 1673 K for 14.4 ks. Fig. 6.1(a) is an SEM micrograph of the interface. The dark regions on the left- and the right-side-end of the micrograph are Si_3N_4. The bright-contrasted region on the center is niobium. Two

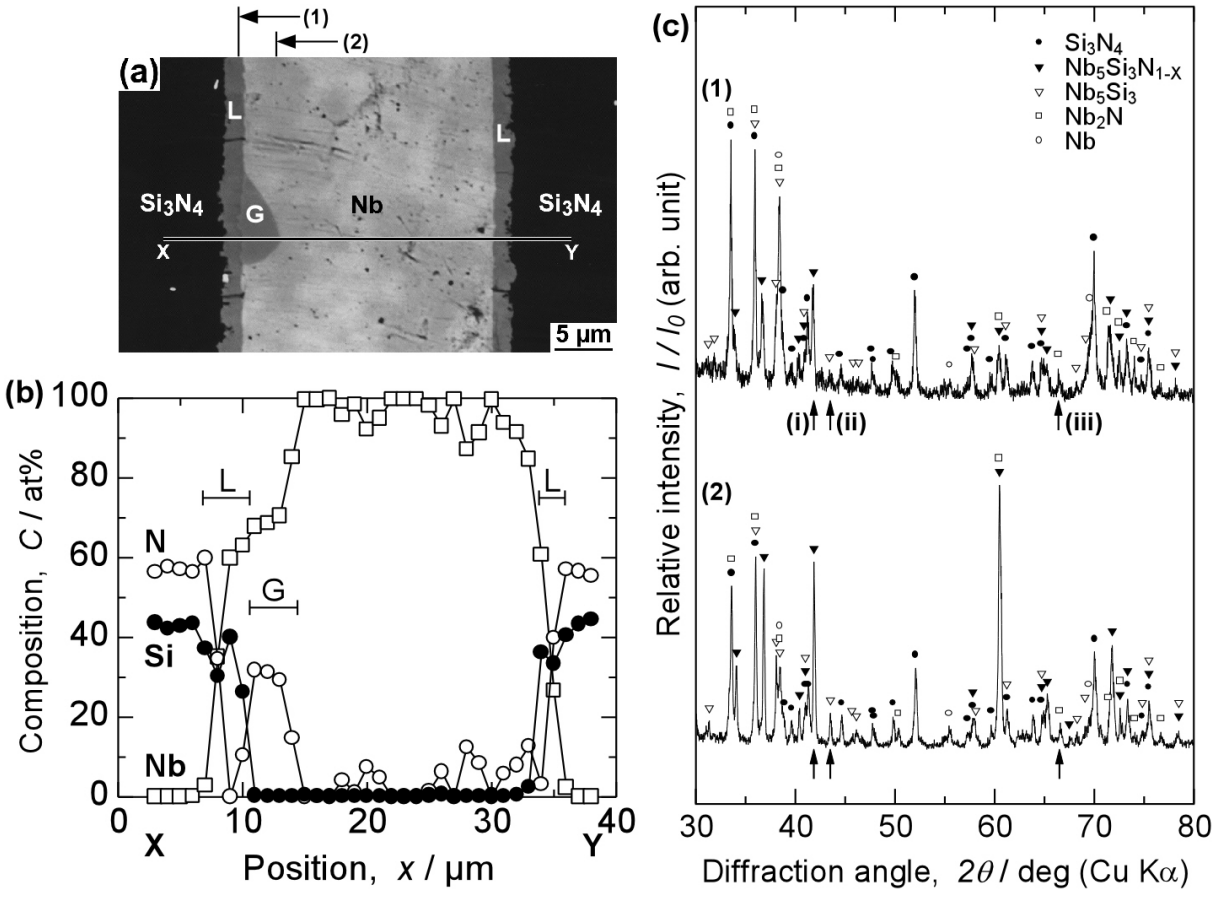

Fig. 6.1 Interfacial microstructure of a Si_3N_4 / Nb joint bonded at 1673 K for 14.4 ks. (a) SEM micrograph, (b) composition profile along the line from X to Y depicted in the micrograph, (c) XRD patterns from the positions (1) and (2) depicted on the top of the micrograph.

types of reaction products are observed between Si_3N_4 and niobium. One is formed as a 2.2 μm-thick layer adjacent to Si_3N_4, on which "L" is marked. The boundary between Si_3N_4 and the L-phase becomes rough and waving, by the occurring interfacial reaction. The other reaction product is formed as grains, on which "G" is marked, in contact with niobium and the layered reaction product. Fig. 6.1(b) shows the elemental distribution profile along the line from X to Y in Fig. 6.1(a). In the niobium matrix, the content of silicon and nitrogen are both very low. The G-phase consists of 68 at% of niobium and 32 at% of nitrogen, where the content of silicon is very low. The L-phase consists of 61 at% of niobium, 34 at% of silicon and 5 at % of nitrogen. In the Si_3N_4 region, no diffusion of niobium is observed. Fig. 6.1(c) shows two typical XRD patterns taken from the positions corresponding to (1) and (2) depicted on the top of Fig. 6.1(a). The specimen was cut at one side of the Si_3N_4 vicinity of the interface and ground down about 1 μm for each XRD measurement. Each reaction product and its arrangement were identified by the positions of diffraction peaks and the alteration of their relative intensities. Both XRD patterns in Fig. 6.1(c) are identified as superimposition of Si_3N_4 [6.16], $Nb_5Si_3N_{1-X}$ [6.17], Nb_5Si_3 [6.18], Nb_2N [6.19] and Nb [6.20]. The appearance of all existing phases in every XRD pattern is due to the detection depth of the diffracted X-ray and the experimental error in grinding flat and parallel to the interface. However, the alteration of the relative intensity appears clearly to the peaks at 41.84°, 43.48° and 66.48°, which are marked with arrows (i), (ii) and (iii), respectively. The peaks (i) and (ii) correspond solely to the 112 plane of $Nb_5Si_3N_{1-X}$ and the 310 plane of Nb_5Si_3, respectively. These peaks appear relatively weak in pattern (1), while their intensity is significantly increased in pattern (2). On the other hand, the peak (iii) corresponds only to 103 plane of Nb_2N. This peak appears relatively strong in pattern (1), while its intensity is decreased in pattern (2). These results indicate that the G phase is Nb_2N and that the L-phase consists of $Nb_5Si_3N_{1-X}$ and Nb_5Si_3. However, the individual phases of $Nb_5Si_3N_{1-X}$ and Nb_5Si_3 cannot be separately recognized in the micrograph (Fig. 6.1(a)).

As shown in Fig. 6.1, the Si_3N_4 side of the L-phase coexists with Si_3N_4, while the Nb side of the L-phase coexists with Nb and Nb_2N. Based on this difference in the coexisting phases, the microstructure in the L-phase can be supposed from the thermodynamic approach. **Fig. 6.2** proposes the Nb-Si-N ternary chemical potential diagram at 1673 K, which is drawn

regarding the available thermodynamic data [6.21, 6.22] and phase diagrams [6.22-6.24]. The chemical potential diagram indicates that $Nb_5Si_3N_{1-X}$ cannot coexist with Nb + Nb_2N, while Nb_5Si_3 cannot coexist with Si_3N_4 in the equilibrium state. Therefore, the Si_3N_4 side of the L phase should be a single phase of $Nb_5Si_3N_{1-X}$ and the Nb + Nb_2N side of the L-phase should be a single phase of Nb_5Si_3. Thus, the phase sequence at the joint interface can be identified as Si_3N_4 / $Nb_5Si_3N_{1-X}$ / Nb_5Si_3 / Nb_2N + Nb / Nb, being consistent with the chemical potential diagram as depicted with a dashed line on Fig. 6.2.

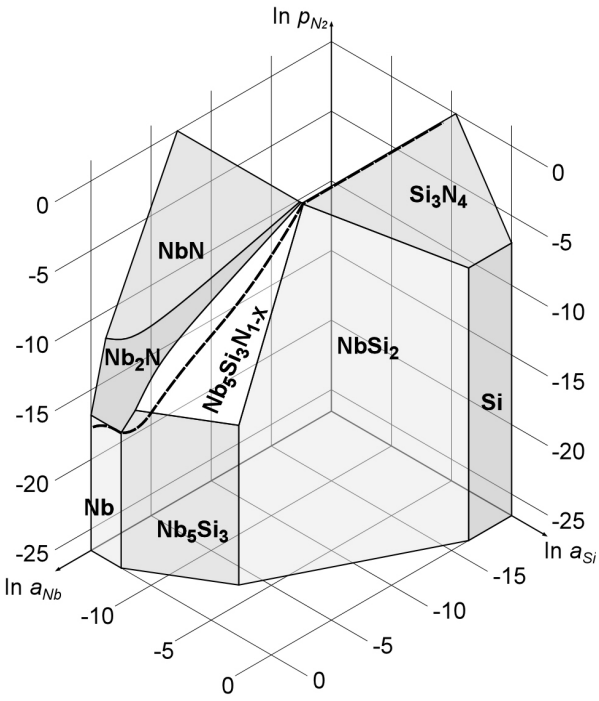

Fig. 6.2 Chemical potential diagram of Nb-Si-N ternary system at 1673 K. The dashed line depicts the phase sequence observed at the joint interfaces bonded at 1673 K.

However, two problems still remain. One is that the thickness of $Nb_5Si_3N_{1-X}$ and Nb_5Si_3 cannot be measured individually. In addition, the phase diagram indicates that $Nb_5Si_3N_{1-X}$ is not stable at 1273 K or lower temperatures [6.22], *i.e.*, $Nb_5Si_3N_{1-X}$ will transform to Nb_5Si_3 during cooling down from the bonding temperature. Therefore, even if $Nb_5Si_3N_{1-X}$ and Nb_5Si_3 could be observed individually, the observed thickness at the ambient temperature will not represent the actual size of them at the bonding temperature. The other problem is the possibility of the microstructure inside the L-phase to be a mixture of $Nb_5Si_3N_{1-X}$ and Nb_5Si_3. In this case, the precise description of the phase sequence becomes as Si_3N_4 / $Nb_5Si_3N_{1-X}$ / $Nb_5Si_3N_{1-X}$ + Nb_5Si_3/ Nb_5Si_3 / Nb_2N + Nb / Nb. To determine the actual microstructure in the layer at elevated temperatures is very difficult, also due to the transformation of $Nb_5Si_3N_{1-X}$ to Nb_5Si_3. Although these two problems remain, the L-phase is treated as the "$Nb_5Si_3N_{1-X}$ / Nb_5Si_3 layer" in the following of this chapter, which is simple but consistent with the chemical potential diagram.

The morphology of the Nb_5Si_3 / Nb_2N + Nb interface indicates that the growth front of

the $Nb_5Si_3N_{1-X}$ / Nb_5Si_3 layer is located on the Si_3N_4 side of the layer. Assuming that the $Nb_5Si_3N_{1-X}$ / Nb_5Si_3 layer grow toward the niobium side of the layer, the layer must grow embedding Nb_2N grains at the nucleated positions of them. However, the actual Nb_5Si_3 / Nb_2N + Nb interface appears almost flat, indicating that the layer grows without embedding Nb_2N grains. Thus, the assumption is wrong. The growth front of the layer being located on the Si_3N_4 side indicates that the growth of the layer is controlled by diffusion of niobium instead of silicon through the layer.

The interfacial microstructures of the joints bonded in other bonding temperature and time were analyzed with the same method. **Fig. 6.3** shows the evolution in the interfacial microstructure of the joints bonded at 1673 K. The bonding time of the joints shown in Figs. 6.3(a), (b) and (c) are 3.6 ks, 14.4 ks and 32.4 ks, respectively. No other reaction products than the $Nb_5Si_3N_{1-X}$ / Nb_5Si_3 layer and the Nb_2N grains are detected at the interfaces. The thickness of the layer and the size of grains increase monotonously by increasing the bonding time. **Fig. 6.4** shows a series of the interfacial microstructures bonded at different bonding temperature and the same bonding time of 14.4 ks. The bonding temperature of the joints shown in Figs. 6.4(a), (b) and (c) are 1573 K, 1673 K and 1773 K, respectively. No other reaction products than the $Nb_5Si_3N_{1-X}$ / Nb_5Si_3 layer and the Nb_2N grains are formed in the range of the bonding

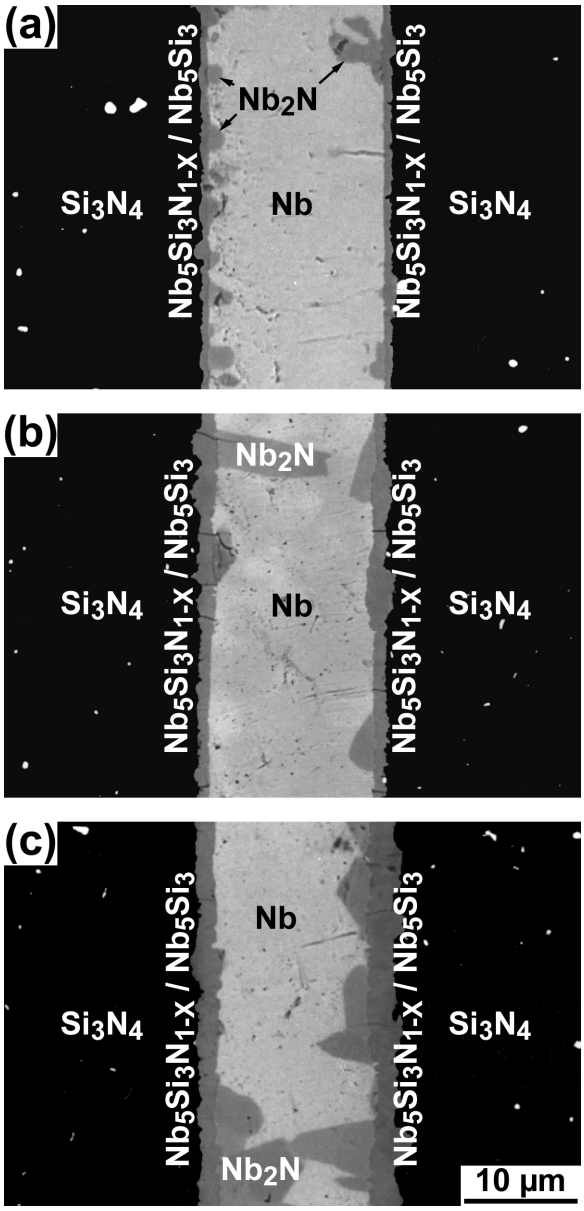

Fig. 6.3 Interfacial microstructure of the joints bonded at 1673 K for three different bonding time. (a) 3.6 ks, (b) 14.4 ks, (c) 32.4 ks.

temperature between 1573 K and 1773 K. The thickness of the layer and the size of grains appear thicker and larger at higher bonding temperature, indicating that the growth rate of the reaction products is higher at higher bonding temperature. At the joint interface bonded at 1773 K for 14.4 ks (Fig. 6.4(c)), the Nb_2N grains grown from both sides have contacted to each other. Even at this interface, the reaction products formed at the interface are only the $Nb_5Si_3N_{1-X}$ / Nb_5Si_3 layer and the Nb_2N grains. Thus, the interfacial phase sequence is unchanged in the range of the bonding temperature and time from 1573 K to 1773 K and from 3.6 ks to 32.4 ks, respectively.

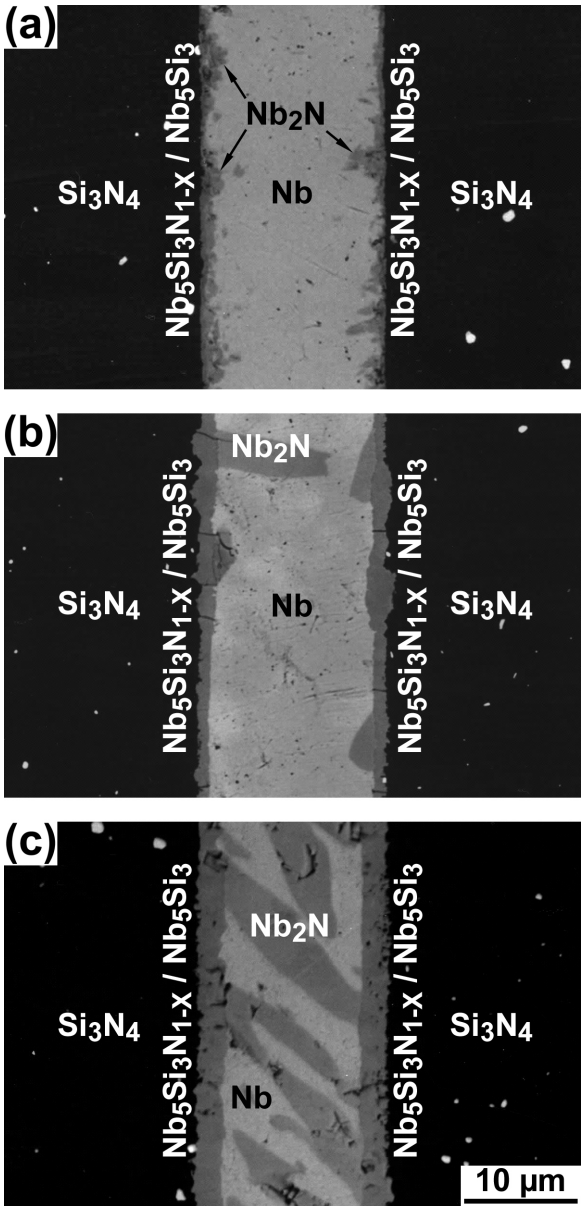

Fig. 6.4 Interfacial microstructure of the joints bonded at three different bonding temperatures for 14.4 ks. (a) 1573 K, (b) 1673 K, (c) 1773 K.

Suganuma *et al.* have reported that a thin layer of Nb_5Si_3 is formed adjacent to Si_3N_4 by diffusion bonding [6.14]. They mentioned that also Nb_2N exists at the interface according to the results of XRD analysis, though Nb_2N could not be observed by SEM. In the present study, the Nb_2N grains was successfully observed at the interfaces. The Nb_2N grains show a uniform direction of their growth (Fig. 6.4(c)), indicating that their growth proceed on the habit plane of the Nb matrix. On the other hand, they could not find the $Nb_5Si_3N_{1-X}$ phase at the interface. The lack of the $Nb_5Si_3N_{1-X}$ phase at the interface can be caused by the slow cooling from the bonding temperature, which allows the transformation of $Nb_5Si_3N_{1-X}$ to Nb_5Si_3. Therefore, their results agree with that of the present study.

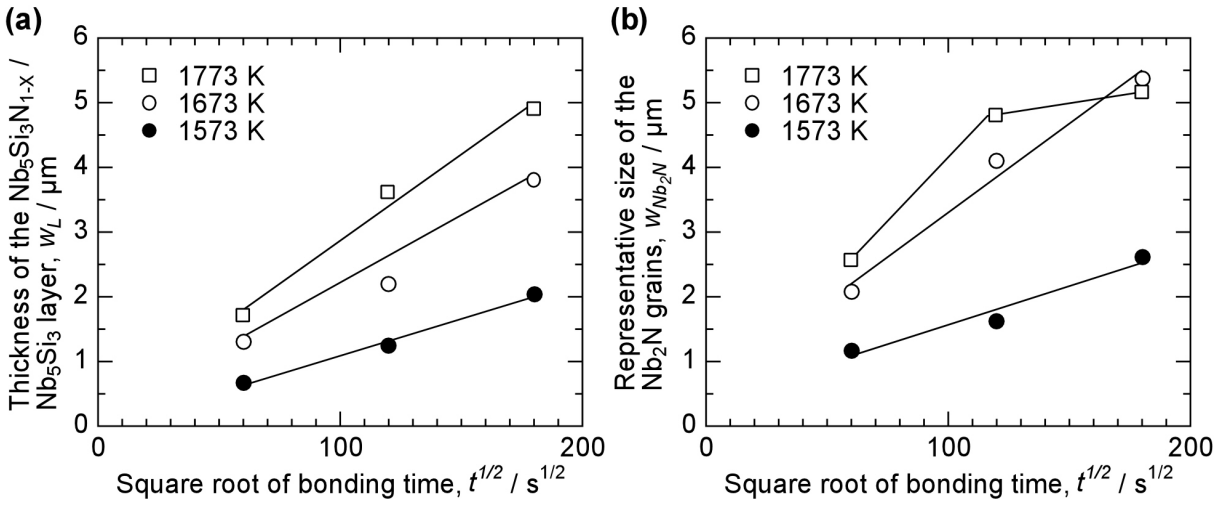

Fig. 6.5 Growth behavior of each reaction product as a function of the bonding temperature and time. (a) the $Nb_5Si_3N_{1-X}$ / Nb_5Si_3 layer, (b) the Nb_2N grains.

Schuster *et al.* have described the interfacial phase sequence of the Si_3N_4 / Nb joints to be Si_3N_4 / Nb_2N / Nb_5Si_3 / Nb at 1273 K [6.25], which is different from the present results. The difference is caused by the method of experiment. Since their study has been implemented by powder reaction experiments, the reaction behavior they observed is dominated by the solid-gas interaction, *i.e.*, the spontaneous decomposition of Si_3N_4 and the reaction of niobium with N_2 gas and silicon. Thus, the phase sequence can be differently observed in powder reaction and in bulk diffusion couples.

C. Growth Behavior of the Reaction Products

Fig. 6.5 shows the growth behavior of the reaction products. Since the individual thickness of $Nb_5Si_3N_{1-X}$ and Nb_5Si_3 cannot be obtained, the total thickness of the $Nb_5Si_3N_{1-X}$ / Nb_5Si_3 layer (w_L) were considered. On the other hand, the amount of Nb_2N grains formed at the interface was estimated using a representative size (w_{Nb2N}) defined as

$$w_{Nb2N} = A_{Nb2N} / 2\,l\,, \tag{6.1}$$

where A_{Nb2N} is the observed total area of each phase and l is the observed length of the interface measuring 89 μm. Fig. 6.5(a) shows the growth behavior of the $Nb_5Si_3N_{1-X}$ / Nb_5Si_3 layer. The layer grows proportionately with the square root of the bonding time, obeying the parabolic law. In addition, the growth rate of the layer is higher at higher bonding temperature. Fig. 6.5(b) shows the growth behavior of the Nb_2N grains. Nb_2N grains grow also obeying the

parabolic law. However, the representative size of the Nb_2N grains formed by bonding at 1773 K for 32.4 ks appears considerably smaller than expected from the parabolic growth. As shown in Fig. 6.4(c), the Nb_2N grains grown from both sides of the niobium foil contacts to each other by bonding at 1773 K for 14.4 ks. Consequently, the Nb_2N grains need to grow to the direction perpendicular to the habit plane, which is slower than the growth on the plane. As the result, the growth of Nb_2N is suppressed. This fact implies that the nucleation frequency of Nb_2N is very low. The number density of the Nb_2N grains does not increase by increasing the bonding temperature and time, as shown in Figs. 6.3 and 6.4. Therefore, the increase in the representative size is resulted by the growth of each Nb_2N grain.

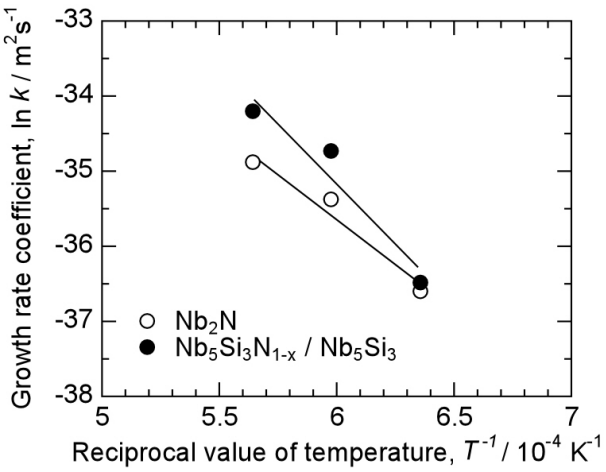

Fig. 6.6 Arrhenius plot of the growth rate coefficient of each reaction product.

Fig. 6.6 shows the temperature dependence of the growth rate of the $Nb_5Si_3N_{1-X}$ / Nb_5Si_3 layer and the Nb_2N grains in the primary stage, in which the Nb_2N grains have not contacted to those grown from the opposite side of the foil, regarding the Arrhenius-type function;

$$\ln k_i = \ln k_{0\,i} - Q_i / RT\,, \tag{6.2}$$

where $k_{0\,i}$ is the pre-exponential factor for the growth rate of each reaction product, Q_i is the apparent activation energy for the growth of each reaction product, R is the gas constant and T is the bonding temperature. Both reaction products change their growth rate proportionately to the reciprocal value of the bonding temperature, indicating that the values of k_{0i} and Q_i are constant. The derived values of k_{0i} and Q_i for each reaction product are listed in **Table 6.2**, in comparison with those reported in the literature. The growth parameters (k_{0i} and Q_i) of the Nb_2N grains have not been found in the literature so far. On the other hand, the apparent activation energy for the growth of the $Nb_5Si_3N_{1-X}$ / Nb_5Si_3 layer obtained in the present study are considerably smaller than those found in the literature.

The growth of the $Nb_5Si_3N_{1-X}$ / Nb_5Si_3 layer is controlled by the diffusion of niobium through the layer. The diffusion is sensitively affected by the existing phases in the layer and

Table 6.2 A list of the pre-exponential factor for the growth rate and the apparent activation energy for the growth of each reaction product.

Reaction products (i)	Pre-exponential factor for the growth rate, $k_{0\,i}$ / m^2s^{-1}	Apparent activation energy for the growth, Q_i / kJ mol^{-1}
Present study (Si_3N_4 / Nb)		
$Nb_5Si_3N_{1-X}$ / Nb_5Si_3 layer	6.1×10^{-10}	2.0×10^{2}
Nb_2N grains	1.2×10^{-7}	2.7×10^{2}
Works in the literature (Si_3N_4 / Nb diffusion couple) Nb_5Si_3 + $NbSi_2$ [6.26]	1×10^{3}	590
(Si_3N_4 / Nb powder reaction) Nb_5Si_3 [6.21]	–	507
(Si_3N_4 / Cu-1%Nb braze) Nb_3Si + NbN [6.2]	–	539

the chemical state of niobium at both sides of the layer. Moreover, the phases constituting the layer varies with the purity of the materials (including the sintering agents), experimental methods and conditions as shown in Table 6.2. Therefore, to clarify the factor dominating the apparent activation energy for the growth of the silicide layer requires extended experiments concerning these parameters. However, the growth parameters of the $Nb_5Si_3N_{1-X}$ / Nb_5Si_3 layer obtained in the present study is considered to be relevant, due to their reproducibility.

D. Joint Strength and Fracture

The fracture strength of the joints changes depending on the bonding temperature and time. **Fig. 6.7** shows the change of the fracture strength of the joints bonded at 1573 K and 1673 K as a function of the square root of the bonding time. At both bonding temperatures, the fracture strength of the joints increases and then decreases by increasing the bonding time, revealing the condition to obtain the maximum strength of the joints. The maximum strength of 131 MPa was obtained with the joints bonded at

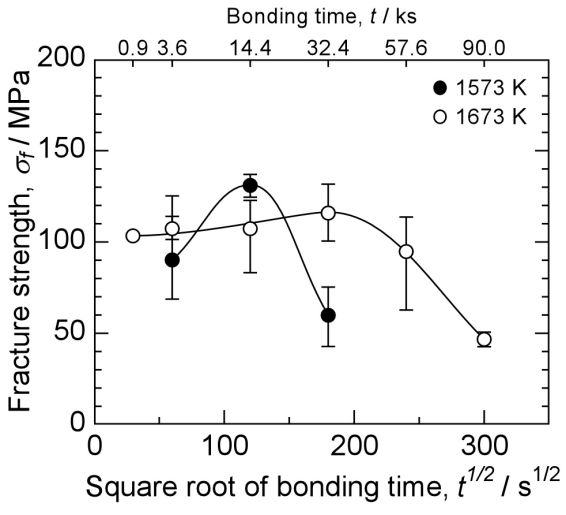

Fig. 6.7 Dependence of the fracture strength of the Si_3N_4 / Nb joints on the bonding temperature and time.

1573 K for 14.4 ks. However, the strength changes sensitively with the bonding time. Therefore, the bonding at this temperature requires a precise control of the bonding time to obtain a strong joint. On the other hand, the maximum strength of the joints bonded at 1673 K was 116 MPa, which was obtained with the bonding time of 32.4 ks. The strength changes mildly by the bonding time at this bonding temperature. In addition, the joints bonded at 1673 K with a short bonding time of 0.9 ks already perform a good strength of 103 MPa, which is higher than the maximum strength of the joints bonded using titanium or vanadium foils.

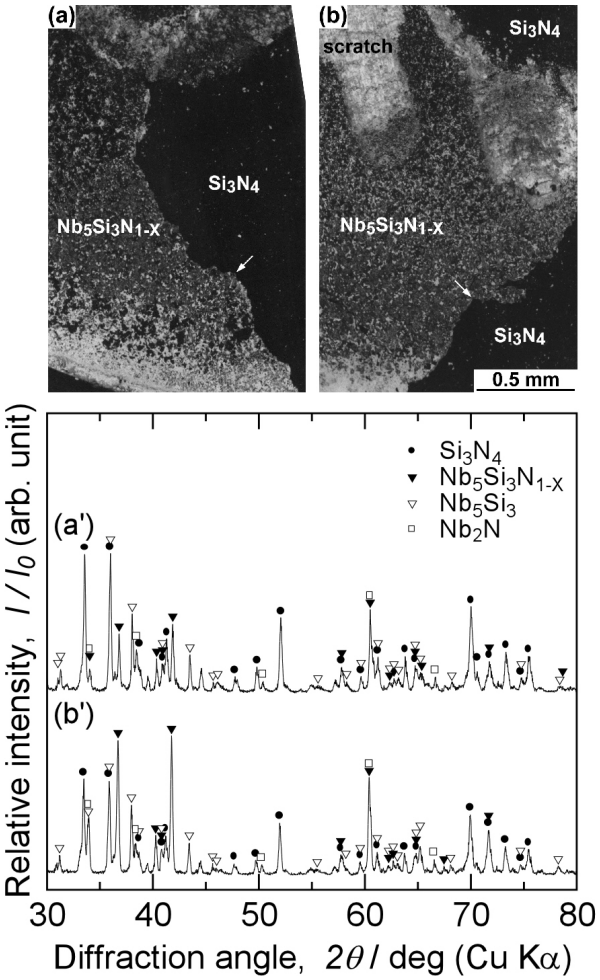

Fig. 6.8 SEM micrographs and corresponding XRD patterns taken from both sides of the fracture surfaces of a joint bonded at 1673 K for 32.4 ks.

Fig. 6.8 shows a pair of SEM micrographs (a and b) and corresponding XRD patterns (a' and b', respectively) taken from both sides of the fracture surfaces of a joint bonded at 1673 K for 32.4 ks. The arrows on the micrographs indicate the corresponding positions of the fracture surfaces. On both sides of the fracture surfaces, Si_3N_4 and $Nb_5Si_3N_{1-X}$ are observed as the major existing phases. The regions with dark contrast on the micrographs are Si_3N_4. The regions with gray contrast are $Nb_5Si_3N_{1-X}$. The surfaces of $Nb_5Si_3N_{1-X}$ appear rough. The shape of the Si_3N_4 regions on one side of the fractured surfaces fits with the shape of the $Nb_5Si_3N_{1-X}$ regions on the other side of the fractured surfaces. This result clearly indicates that the fracture of the joint occurs at the Si_3N_4 / $Nb_5Si_3N_{1-X}$ interface in a brittle mode. Moreover, the fracture surfaces showing the $Nb_5Si_3N_{1-X}$ regions directly connected to the Si_3N_4 regions indicate that the fracture of the foil and the reaction products proceed almost perpendicular to

the foil. The fracture of the foils is considered to occur to connect the front lines of the cracks propagating at the Si_3N_4 / $Nb_5Si_3N_{1-X}$ interfaces on both sides of the joint. The XRD patterns indicate that Si_3N_4, $Nb_5Si_3N_{1-X}$, Nb_5Si_3 and Nb_2N exist at both fracture surfaces. However, the appearance of Nb_5Si_3 and Nb_2N is due to the scratching of the fracture surfaces, which is inevitable with shear fracture testing and appears on the upper part of Fig. 6.8(b), and to the size of the reaction products thinner and smaller than the penetration depth of the X-ray. Based on these results, the fracture path is determined as the Si_3N_4 / $Nb_5Si_3N_{1-X}$ interface.

The common characteristics in the growth behavior of the interfacial microstructure of the joints and the change of the fracture strength are hardly found. Comparing Figs. 6.5 and 6.7, the change of the strength of the joints seems to be independent on the thickness of the $Nb_5Si_3N_{1-X}$ / Nb_5Si_3 layer. In addition, the fracture path of the joints does not change by bonding temperature and time. This result implies that the joint strength is dominated by the bond strength at the Si_3N_4 / $Nb_5Si_3N_{1-X}$ interface instead of the thickness of the $Nb_5Si_3N_{1-X}$ / Nb_5Si_3 layer. Since the deterioration factors of the interfacial bond strength are the thermal residual stress and the distribution of the bond defects such as voids and cracks, a technology to design the interfacial microstructure which reduces or relieves the residual stress (*e.g.* by modifying the phase sequence to change the phase adjacent to Si_3N_4) and prevents the formation of defects (*e.g.* by enhancing the Nb_2N formation) is required for the improvement of the strength of the joints.

E. Effect of Initial Grain Size of Niobium Insert

The solid state diffusion bonded Si_3N_4 joints using niobium foils perform higher fracture strength than those bonded using titanium or vanadium. Although the change of the strength of the joints appears independent on the thickness of the $Nb_5Si_3N_{1-X}$ / Nb_5Si_3 layer, a method to modify the interfacial microstructure in order to improve the strength was considered. The interfacial microstructure of Si_3N_4 / Nb joints and its evolution behavior shows a similarity with that of Si_3N_4 / V joints bonded at 1473 K and below, except one point. The Si_3N_4 / V joints form a metastable Si_3N_4 / V_3Si interface in the early stage of the interfacial reaction, which performs the highest strength in the system. Thus, the interfacial microstructure and the joint strength can be changed by controlling the reaction rate. Based on the result that the

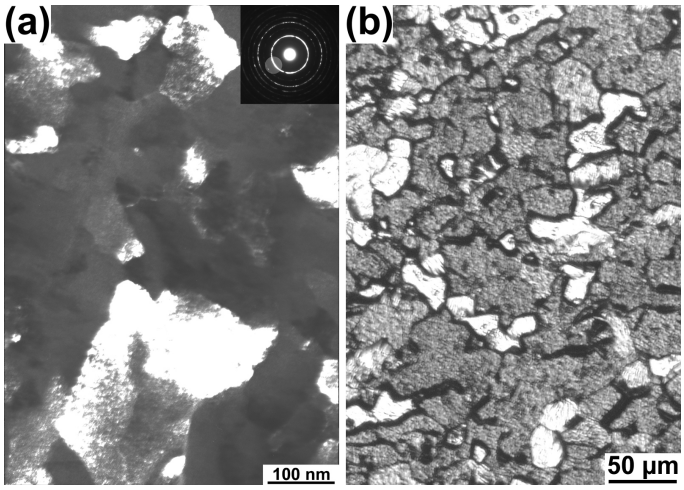

Fig. 6.9 Grain size of (a) deposited films and (b) ordinary polycrystalline foils of niobium.

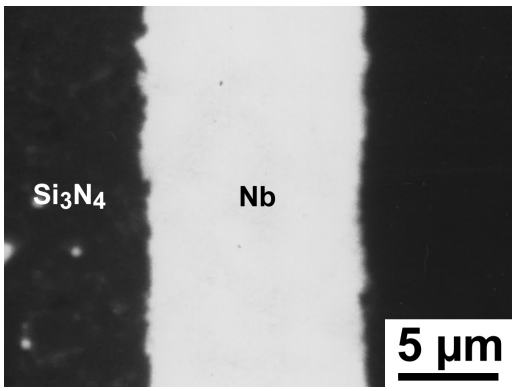

Fig. 6.10 Initial state of radio-frequency magnetron sputter deposited niobium foil.

growth of the $Nb_5Si_3N_{1-X}$ / Nb_5Si_3 layer is dominated by the diffusion of niobium, the reaction rate can be modified by controlling the diffusion of niobium in the layer. Since the diffusion through grain boundaries is faster than that through grain body, the effect of the initial grain size (*i.e.*, the density of the grain boundary) of the niobium foils on the interfacial reaction behavior was investigated. For this purpose, diffusion bonding of Si_3N_4 using single-crystal foils of niobium with its foil normal being 100 plane and niobium films directly deposited on the bonding surface of Si_3N_4 by radio-frequency magnetron sputter deposition technique was implemented.

The average grain size of each type of niobium foils was measured at first. **Fig. 6.9** shows a dark field TEM image of the deposited film using 110 and 200 reflections of niobium, in comparison with an OM image of the ordinary foils. The grain sizes of ordinary foils and deposited films measured 46 μm and 86 nm, respectively. The deposited niobium films had a significantly fine-grained structure. In addition, no reaction products were formed at the interface during deposition, as shown in **Fig. 6.10**. The thickness of the deposited film measured 11.0 μm.

Fig. 6.11 shows the interfacial microstructures of the joints bonded at 1673 K for 14.4 ks using a single-crystal foil, an ordinary foil and the deposited film with their analysis results. $Nb_5Si_3N_{1-X}$, Nb_5Si_3 and Nb_2N are detected in every joints as the interfacial reaction products. This result indicates that no metastable interfaces are formed by changing the initial grain size

of the niobium foils. However, the interfacial microstructures of the joints appear different by changing the grain size of the niobium foils in two points. The first point is that the $Nb_5Si_3N_{1-X}$ / Nb_5Si_3 layer formed by bonding treatment of 1673 K, 14.4 ks using the single crystal foils, the ordinary foils and the deposited films grow to 2.3 μm, 2.2 μm and 2.6 μm, respectively. This result indicates that the growth rates of the layer for the single crystal foils and the ordinary foils are almost the same, while that for the deposited film is slightly higher. The second point is that the Nb_2N grains formed at the interface of the deposited films appear with different morphology from those of the single-crystal foils and the ordinary foils. The Nb_2N grains are formed in contact with Nb_5Si_3 and Nb, and grow on the habit plane of the Nb matrix, when the single-crystal foils or the ordinary foils are used. On the other hand, the Nb_2N are formed as a layer between Nb_5Si_3 and Nb and as grains inside the Nb, when the deposited films are used. The phase sequence of this interface is described as Si_3N_4 / $Nb_5Si_3N_{1-X}$ / Nb_5Si_3 / Nb_2N / Nb+Nb_2N. In addition, the grains of Nb_2N appear in equiaxial shape with almost uniform diameter of 2.7 μm. This result indicates that the growth of the Nb_2N grains are restricted within the grains of the Nb matrix.

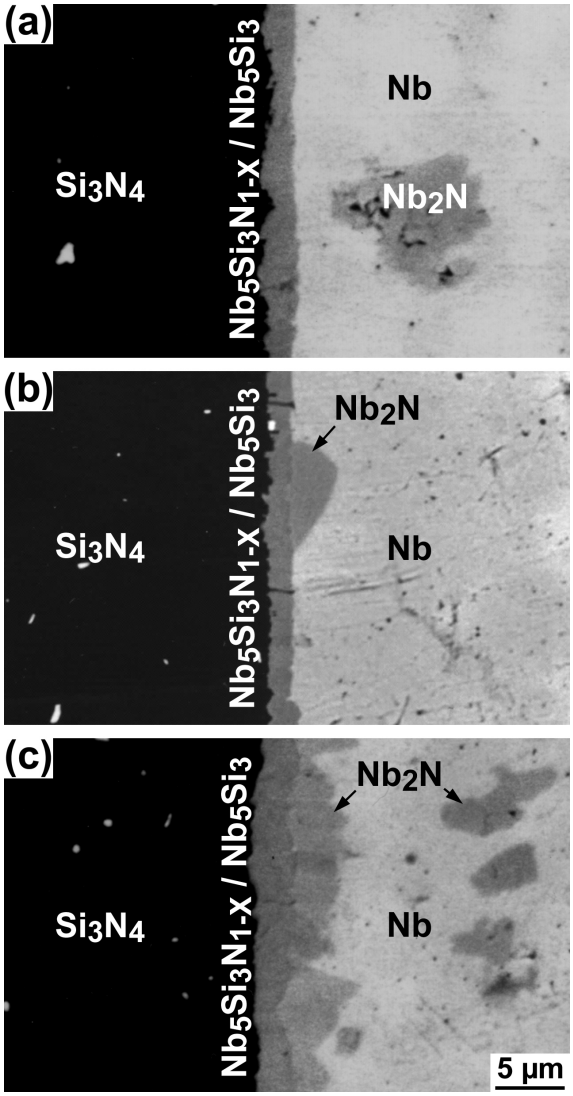

Fig. 6.11 Interfacial microstructure of the Si_3N_4 / Nb joints bonded at 1673 K for 14.4 ks using niobium insert with different initial grain sizes. (a) single crystal, (b) ordinary polycrystalline, (c) deposited film.

The difference of the three types of niobium foils is only the initial grain size of niobium. The deposited films have significantly higher density of grain boundaries, which enhances the grain boundary diffusion of the elements. On the other hand, the density of grain

boundaries enhances also the frequency of Nb_2N nucleation. This role of the grain boundary allows the formation of Nb_2N as a layer adjacent to Nb_5Si_3. Taking into account that the growth of the $Nb_5Si_3N_{1-X}$ / Nb_5Si_3 layer is dominated by the diffusion of niobium through the layer, Nb_2N formed as a layer is considered to work as the diffusion barrier for niobium. Thus, only a slight enhancement in the growth rate of the $Nb_5Si_3N_{1-X}$ / Nb_5Si_3 layer is observed at the interface of Si_3N_4 / deposited Nb joints by these two competitive mechanism of the diffusion of niobium.

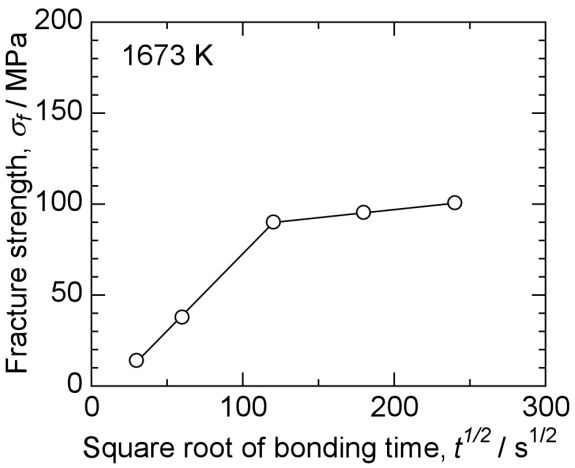

Fig. 6.12 Dependence of the fracture strength of Si_3N_4 / deposited Nb film joints on the bonding time.

Fig. 6.12 shows the dependence of the fracture strength of the Si_3N_4 / deposited Nb joints bonded at 1673 K on the bonding time. Although the joints bonded for 0.9 ks perform a low strength of 17 MPa, the strength increases by increasing the bonding time, reaching 97 MPa with the bonding time of 14.4 ks. Then, the strength increases rather slowly by the prolonged bonding time. The highest strength of 100 MPa is obtained with the bonding time of 57.6 ks, though it is not still the maximum. The strength of the Si_3N_4 / deposited Nb joints appears slightly lower than that of the Si_3N_4 / ordinary Nb joints bonded at 1673 K (*cf.* Fig. 6.7) in the range of the bonding time from 0.9 ks to 32.4 ks. However, the Si_3N_4 / deposited Nb joints retain the high strength of 100 MPa after the bonding treatment for 57.6 ks, while the strength of the Si_3N_4 / ordinary Nb joints is deteriorated by the bonding time longer than 32.4 ks. This result implies that the strength of the Si_3N_4 / deposited Nb joints is scarcely affected by the growth of the reaction products, being adequate for fabrication of long-life high-temperature structures.

IV. Summary

Si_3N_4 was bonded to niobium foils by solid state diffusion bonding. The interfacial microstructure and reaction behavior were analyzed by means of SEM, EPMA and XRD and

considered on the basis of the Nb-Si-N ternary chemical potential diagram. The strength of the joints was estimated by a shear fracture test. The following points were clarified.

1) The interfacial phase sequence is considered to be Si_3N_4 / $Nb_5Si_3N_{1-X}$ / Nb_5Si_3 / Nb_2N + Nb / Nb. The phase sequence does not change by changing the bonding temperature and time in the range from 1573 K to 1773 K and from 3.6 ks to 32.4 ks, respectively.
2) The reaction products grow monotonously obeying the parabolic law. The values of the pre-exponential factor for the growth rate and the apparent activation energy for the growth of the $Nb_5Si_3N_{1-X}$ / Nb_5Si_3 layer are 6.1×10^{-10} m^2s^{-1} and 2.0×10^2 kJ mol^{-1}, respectively, while those of the Nb_2N grains are 1.2×10^{-7} m^2s^{-1} and 2.7×10^2 kJ mol^{-1}, respectively.
3) The maximum fracture strength of 131 MPa was obtained with the joints bonded at 1573 K for 14.4 ks. The strength changes sensitively to the bonding time, when the joints are bonded at 1573 K. However, the change becomes mild when they are bonded at 1673 K. The fracture occurs at the Si_3N_4 / $Nb_5Si_3N_{1-X}$ interface in a brittle mode.
4) The interfacial microstructure of the joints bonded using fine-grained (86 nm-diameter) films of niobium appears with the phase sequence of Si_3N_4 / $Nb_5Si_3N_{1-X}$ / Nb_5Si_3 / Nb_2N / Nb+Nb_2N, which is different from those bonded using ordinary polycrystalline (46 μm-diameter) foils or single-crystal foils. The growth rate of the $Nb_5Si_3N_{1-X}$ / Nb_5Si_3 layer is slightly enhanced by the grain refinement, as the result of competitive two mechanisms: the enhancement of grain boundary diffusion and the formation of the Nb_2N diffusion barrier layer. The interfacial microstructure and the growth rate of the reaction products of the joints using ordinary polycrystalline foils and single crystals appear almost the same.
5) The joints bonded using deposited films of niobium retain high fracture-strength of 100 MPa even after a prolonged bonding treatment of 57.6 ks at 1673 K.

References

[6.1] Y. Nakao, K. Nishimoto and K. Saida: Trans. Jpn. Weld. Soc., 1990, Vol. 21, pp. 135-143.

[6.2] Y. Nakao, K. Nishimoto and K. Saida: ISIJ Int., 1990, Vol. 30, pp. 1142-1150.

[6.3] Y. Morizono, T. Nakata, M. Nishida and A. Chiba: J. Ceram. Soc. Jpn., 1995, Vol. 103, pp. 810-815, in Japanese.

[6.4] Y. Ishida, J.-Y. Wang and T. Suga: *ISIJ Int.*, 1990, Vol. 30, pp. 1041-1045.

[6.5] M. Kohyama and R. Yamamoto: *Bull. Jpn. Inst. Met.*, 1990, Vol. 29, pp. 893-901, in Japanese.

[6.6] F.S. Ohuchi: *Bull. Jpn. Inst. Met.*, 1990, Vol. 29, pp. 902-909, in Japanese.

[6.7] B. Gibbesch and G. Elssner: *Acta Metall. Mater.*, 1992, Vol. 40, Suppl., pp. S59-S66.

[6.8] I.E. Reimanis: *Acta Metall. Mater.*, 1992, Vol. 40, Suppl., pp. S67-S74.

[6.9] C.H. Lee and K.S. Liang: *Acta Metall. Mater.*, 1992, Vol. 40, Suppl., pp. S143-S147.

[6.10] W. Mader and D. Knauss: *Acta Metall. Mater.*, 1992, Vol. 40, Suppl., pp. S207-S215.

[6.11] J. Mayer, G. Gutekunst, G. Möbus, J. Dura, C.P. Flynn and M. Rühle: *Acta Metall. Mater.*, 1992, Vol. 40, Suppl., pp. S217-S225.

[6.12] D.X. Li, P. Pirouz, A.H. Heuer, S. Yadavalli and C.P. Flynn: *Acta Metall. Mater.*, 1992, Vol. 40, Suppl., pp. S237-S247.

[6.13] D. Korn, G. Elssner, H.F. Fischmeister and M. Rühle: *Acta Metall. Mater.*, 1992, Vol. 40, Suppl., pp. S355-S360.

[6.14] K. Suganuma, T. Okamoto, Y. Miyamoto, M. Shimada and M. Koizumi: *Mater. Sci. Technol.*, 1986, Vol. 2, pp. 1156-1161.

[6.15] Y. Iino and N. Taguchi: *J. Mater. Sci. Lett.*, 1988, Vol. 7, pp. 981-982.

[6.16] *Powder Diffraction File*, JCPDS–ICDD, 33-1160.

[6.17] *Powder Diffraction File*, JCPDS–ICDD, 8-422.

[6.18] *Powder Diffraction File*, JCPDS–ICDD, 30-874.

[6.19] *Powder Diffraction File*, JCPDS–ICDD, 40-1274.

[6.20] *Powder Diffraction File*, JCPDS–ICDD, 35-789.

[6.21] T. Shimoo, S.-I. Adachi and K. Okamura: *J. Jpn. Inst. Met.*, 1994, Vol. 58, pp. 796-802, in Japanese.

[6.22] *Phase Diagrams of Ternary Boron Nitride and Silicon Nitride Systems*, P. Rogl and J.C. Schuster (Eds.), ASM International, Materials Park, Ohio (USA), 1992, pp. 172-174.

[6.23] Yu.V. Levinskiy: *Alloy Phase Diagrams*, H. Baker (Ed.), ASM Handbook, Vol. 3, ASM International, Materials Park, Ohio (USA), 1992, pp. 2·298.

[6.24] H. Okamoto, A.B. Gokhale and G.J. Abbaschian: *Alloy Phase Diagrams*, H. Baker (Ed.), ASM Handbook, Vol. 3, ASM International, Materials Park, Ohio (USA), 1992, pp. 2·306.

[6.25] J.C. Schuster, F. Weitzer, J. Bauer and H. Nowotny: *Mater. Sci. Eng.*, 1988, Vol. A105/106, pp. 201-206.

[6.26] P. Lamparter, S. Steeb and A. Gukelberger: High Temp. High Press., 1971, Vol. 3, pp. 727-740.

Chapter 7 Discussion

On the basis of the results presented in Chapters 4, 5 and 6, this chapter discusses the philosophy to design and control the interfacial microstructures of silicon nitride / metal joints by solid state diffusion bonding. The basic knowledge on the diffusion path, the fracture path and the growth behavior of the target phase is essential to design and control the interfacial microstructures. The chemical potential diagrams, which visualize the tendency of each constituent element for diffusion and reaction, suggest the phase sequences consistent with the metallurgical thermodynamics. Two newly developed techniques in the present study for artificial modification of the interfacial microstructures are explained using the corresponding chemical potential diagrams: the nitrogen presolution and the grain size refinement of the active metals.

I. Introduction

Active metal bonding of ceramic materials is understood as a two-step process; a step to remove the passive layer on the surface of the ceramics and metals by diffusion and reaction and that to form a chemical bond between the "activated" surfaces of ceramics and metals. Generally, heat is used as the energy for the process, which conducts the steps simultaneously. The surface activation bonding has proven that the steps can be divided and that high-temperatures is not a necessary condition for bonding materials [7.1-7.3]. Some ceramic / metal combination achieve a strong bond without formation of reaction products. Therefore, to form a reaction product is also not a necessary factor for good bonding, but a subsidiary result of the removal of passive layers and bond formation by heat. In some particular cases, as proposed by Ishida *et al.* [7.4-7.6], the reaction products can reduce the residual stress and

improve the strength of the joints. In most cases, however, the brittleness and weakness of the reaction products show a negative effect on the strength of the joints. Therefore, to control the interfacial microstructure to minimize the effect is important.

II. Comparison of Titanium, Vanadium and Niobium as Bonding Fillers

A. Bondability and Fracture Strength of the Joints

Solid state diffusion bonding of Si_3N_4 using titanium, vanadium and niobium foils are successful in the limited condition of bonding time and temperature. Among these three active metal elements, vanadium shows the highest bondability with Si_3N_4. Although a prolonged bonding time is required, vanadium can bonded to Si_3N_4 at the bonding temperature of 1273 K. The bondability of titanium follows vanadium, which can bonded at 1473 K. Niobium requires higher bonding temperature and longer bonding time than other two elements.

The joints with the highest fracture strength in the present research were obtained with those bonded at 1573 K for 14.4 ks using niobium foils, which have marked 131 MPa. The joints bonded using vanadium foils showed the maximum fracture strength of 94 MPa with those bonded at 1673 K for 0.4 ks. However, the joints bonded using titanium foils showed very poor strength. A shear stress of 3.5 MPa is enough to fracture every joint bonded at 1573 K for 3.6 ks. The greatest carefulness was required during handling of the Si_3N_4 / Ti joints.

In most cases, the bondability of Si_3N_4 using active metals reflects the onset temperature of the reactions of the surface activation and the bond formation. These reactions are driven by the reduction of the Gibbs energy of the system and dominated by the mobility of the constituent atoms represented by the diffusion coefficient. The change of the Gibbs energy can be estimated with the standard Gibbs energies of

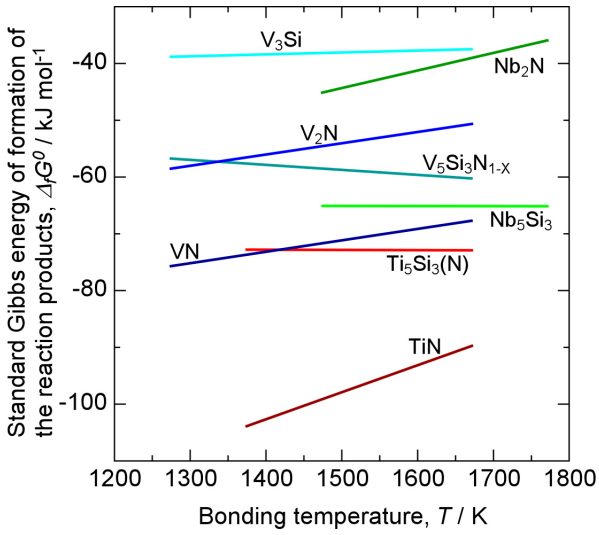

Fig. 7.1 The standard Gibbs energy of formation of the reaction products observed at the Si_3N_4 / active-metal interfaces as a function of the bonding temperature.

formation of the reaction products. On the other hand, the diffusion coefficients and their temperature dependence are hardly found on the literature. Thus, the mobility is estimated by the melting temperature, an another property dominated by the chemical constraint each constituent atoms suffer. **Fig. 7.1** shows the standard Gibbs energies of formation of the reaction products observed at the Si_3N_4 / active-metal interfaces in relation with the bonding temperature. TiN and $Ti_5Si_3(N)$ show the largest amount of Gibbs energy reduction indicating that the reactivity of titanium with Si_3N_4 is the highest among these three active elements. The melting temperature of titanium, vanadium and niobium are 1953 K, 2108 K and 2793 K, respectively (*cf.* Table 1.6). Titanium has the lowest melting temperature among the elements. Based on these data, the highest bondability will be expected with the titanium insert. Indeed, the reaction between Si_3N_4 and titanium occurs even at 1373 K and below. However, the bonding experiments of bulk Si_3N_4 using titanium foils failed to obtain joints at these low temperatures. The formation of the brittle and weak $Ti_5Si_3(N)$ layer adjacent to Si_3N_4 has been argued as the weakening factor in Chapter 4. However, this argument cannot successfully explain the experimental result that the higher bonding temperature and the longer bonding time resulting in the thicker formation of the $Ti_5Si_3(N)$ layer achieves the bonding of bulk Si_3N_4. The experimental results are understood by introducing the bond-formation efficiency (η) described as

$$\eta = \sum_{i=1}^{n}\left(\zeta_i\sigma_b - \sigma_{ri}\right) \Big/ \sum_{j=1}^{N}\left(\zeta_j\sigma_b - \sigma_{rj}\right), \tag{7.1}$$

Table 7.1 A list of factors causing the reduction of the actual atomic bond formation.

Factors	Causes
Insufficient removal of the passive layer on the surface	Low bonding temperature Short bonding time Insufficient removal of the surface oxide scales Insufficient surface cleaning and degreasing
Insufficient interfacial contact	Surface roughness Insufficient bonding pressure Low bonding temperature (high yield stress of the materials)
Void formation	Interfacial reaction (especially in the cooling process) Insufficient bonding pressure (regard to the Le Chatelier's principle)

Table 7.2 Phase sequence and fracture path of solid state diffusion bonded Si_3N_4 / metal interfaces observed in the present research.

System	Phase sequence	Fracture path
Si_3N_4 / Ti	[observed at the room temperature] at 1473 K: Si_3N_4 / Ti_5Si_3 / Ti_5Si_3 + α-Ti(N) / α-Ti(N) + Ti_5Si_3 at 1573 K: Si_3N_4 / Ti_5Si_3 / Ti_5Si_3 + α-Ti(N) / Ti_5Si_3 / α-Ti(N) + Ti_5Si_3 at 1673 K: Si_3N_4 / Ti_5Si_3/ Ti_5Si_3 + TiN / Ti_5Si_3 / α-Ti(N) + Ti_5Si_3 [actual phase sequence at elevated temperatures] Si_3N_4 / Ti_5Si_3(N) / α-Ti (N) + Ti_5Si_3(N)	at the Si_3N_4 / Ti_5Si_3 interface
Si_3N_4 / V	[at 1473 K and below] (1) Si_3N_4 / V_3Si / V+V_2N / V (2) Si_3N_4 / $V_5Si_3N_{1-X}$ / V_3Si / V+V_2N (3) Si_3N_4 / $V_5Si_3N_{1-X}$ / V_3Si / V_2N (4) Si_3N_4 / $V_5Si_3N_{1-X}$ / V_2N + VN / V_2N [at 1498 K and above] (1) Si_3N_4 / V_3Si / V(Si) / V+V_2N (2) Si_3N_4 / $V_5Si_3N_{1-X}$ / V_3Si / V(Si) / V+V_2N (3) Si_3N_4 / $V_5Si_3N_{1-X}$ / V_3Si / V_2N (4) Si_3N_4 / $V_5Si_3N_{1-X}$ / V_2N + VN / V_2N (5) Si_3N_4 / $V_5Si_3N_{1-X}$ / VN	[high-strength joints] at the Si_3N_4 / V_3Si interface and partly in the V_3Si layer [strength-deteriorated joints by prolonged bonding time] in the $V_5Si_3N_{1-X}$ layer
Si_3N_4 / Nb	Si_3N_4 / $Nb_5Si_3N_{1-X}$ / Nb_5Si_3 / Nb_2N + Nb / Nb	at the Si_3N_4 / $Nb_5Si_3N_{1-X}$ interface

where N is the total number of bond-sites existing at the interface, n is the actual number of bonds formed at the interface, σ_b is the ideal bond strength of atoms, ζ_i is the bond-deterioration factor by the crystallographic mismatch of atomic arrangement at the interface, $-\sigma_{ri}$ is the deterioration of the bond strength by the residual stress for the bond i. When the ideal bond is achieved (*i.e.*, $\eta = 1$), the joints perform the fracture strength (σ_f^0) described as

$$\sigma_f^0 = \sum_{j=1}^{N} \left(\zeta_j \sigma_b - \sigma_{rj} \right) . \tag{7.2}$$

However, the actual bond strength (σ_f), described as

$$\sigma_f = \sum_{i=1}^{n} \left(\zeta_i \sigma_b - \sigma_{ri} \right) = \eta \sigma_f^0 , \tag{7.3}$$

is deteriorated by taking the smaller value of n than N. The number of bonds formed at the interface is reduced by the insufficient removal of the passive surface, the insufficient interfacial contact and the void formation, as listed in **Table 7.1**. The first and the second factors dominate the failure of the bonding experiments at low bonding temperatures and short bonding times. Although the titanium shows the highest reactivity with Si_3N_4, the reaction product $Ti_5Si_3(N)$ is considered to form fewer and weaker atomic bonds with Si_3N_4. As the result of low η and σ_f^0, the Si_3N_4 / Ti joints show low strengths which fail without additional external force, even though the interfacial reaction takes place.

B. Interfacial Microstructure, Reaction Kinetics and Fracture Locations

The results of the present research have shown that titanium, vanadium and niobium react with Si_3N_4 during solid state diffusion bonding at sufficient high temperatures. The interfacial phase sequences observed in the present research are successfully expressed using the chemical potential diagrams (*cf.* Figs. 4.5, 5.3, 5.6 and 6.2). The phase sequence and the fracture path of the joints observed in the present research are summarized in **Table 7.2**. Two characteristic points appear in the table. One is the reaction product formed adjacent to Si_3N_4. By the reaction of Si_3N_4 and these active metals, a layer of metal-silicide (Ti_5Si_3, V_3Si) or metal-silicide-based ternary phase ($V_5Si_3N_{1-X}$, $Nb_5Si_3N_{1-X}$) is formed adjacent to Si_3N_4. The other point is the fracture path. The joints always fracture at the interface between Si_3N_4 and its neighboring layered reaction product or inside the layered reaction product formed adjacent to Si_3N_4.

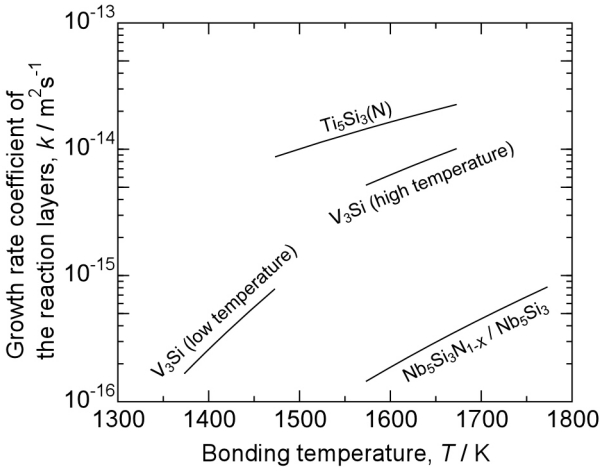

Fig. 7.2 Growth rate coefficients of the reaction products formed adjacent to Si_3N_4 as the functions of the bonding temperature.

The growth rate coefficients of the $Ti_5Si_3(N)$, V_3Si and $Nb_5Si_3N_{1-X}$ / Nb_5Si_3 layers formed adjacent to Si_3N_4 are depicted in **Fig. 7.2** as the functions of the bonding temperature. Comparing the growth rates of $Ti_5Si_3(N)$, V_3Si and $Nb_5Si_3N_{1-X}$ / Nb_5Si_3 (k_{Ti}, k_V and k_{Nb},

respectively), the order of the growth rates of the reaction products appear as $k_{Ti} \geq k_V \geq k_{Nb}$ within the range of the bonding temperature employed in the present study. This order of the growth rates agrees well with the reactivity of the active metals with Si_3N_4, discussed in the last subsection.

III. A Philosophy to Control the Interfacial Microstructure

The appropriate design and control of the interfacial microstructure should be made on the basic knowledge on the following three points.

The first point is the interfacial phase sequence and local phase equilibria, which the Si_3N_4 / active-metal system tends to achieve. At this point, an attention to the actual phase sequence at the elevated temperatures should be paid. Some systems like Si_3N_4 / Ti reveal phase sequences after cooling down to the room temperature different from those at the bonding temperatures. Although the phase transformation during cooling is also an important issue for the performance of the joints, the issue is not taken with severity because it can be controlled by the state of the interfacial microstructure when the cooling starts and by the cooling rate.

The second point is the determination of the target phase for control. In the present study, the purpose of the control of the interfacial microstructure is to improve the strength of the joints. To improve the strength of the joints by the control of the interfacial microstructure corresponds to suppress the microstructural factors deteriorating the strength of the joints. The formation of brittle-and-weak reaction products and defects such as voids and cracks are considered as the strength-deteriorating microstructural factors. The target phase for control is determined on the basis of the fracture analysis, which reveals the weakest microstructure at the interface.

The third point is the growth behavior of the target phase. To understand the growth behavior, the following two issues are required to be clarified. One is the growth rate. Although the growth rate is proven that it is affected by the composition and the grain size of the active-metal, the growth rate coefficient and the apparent activation energy of growth for ordinary cold-rolled active-metal foils has to be known. The other issue is the growth front of the phase. The knowledge on the growth front is indispensable, since it indicates the element

dominating the growth of the target phase.

Based on the knowledge on these three points, the interfacial microstructure of the joints are designed. Against the brittle-and-weak reaction products and voids, the strength-deteriorating factors resulted from the interfacial reaction, the microstructure is designed to avoid the formation of the phases which are brittle-and-weak and drastically change the solubility of nitrogen depending on the temperature. On the other hand, the microstructure is designed to be the appropriate phase sequence to relax the thermal residual stress, derived from the thermal mechanical properties of the individual phases, against the cracks.

The phase sequence must be designed keeping the consistency with the metallurgical thermodynamics. The chemical potential diagrams and the phase diagrams are the essential charts which guide and verify the design from the thermodynamical point of view. The chemical potential diagrams visualize the relation between the chemical potential of each constituent element and the phase equilibria in the system. They describe the diffusion path of the constituent elements with a simple curve, indicating the driving force working to each element for monotonous transition from the high chemical potential state to the low. Thus, a phase sequence designed on the corresponding chemical potential diagram with a monotonous curve is consistent with the metallurgical thermodynamics. In other words, the designed phase sequence can be verified using the chemical potential diagrams. This property of the diagrams is indispensable for controlling the diffusion and reaction at the interfaces, which cannot be obtained from the phase diagrams. On the other hand, the phase diagrams visualize the relation between the chemical composition and the phase equilibria. The diffusion path described on the phase diagrams crosses the straight line connecting the end member phases at least one time, which indicates the conservation of the stoichiometric condition. However, the phase diagrams cannot verify the designed phase sequences whether they are allowed thermodynamically. They are applied for the design of the phase sequence to prevent void formation, taking advantage of the diagrams that directly indicate the solubility change by temperature. In addition, the phase diagrams are important for phase identification from composition analysis.

IV. Control of the Interfacial Microstructure in Individual Systems

A. The Si_3N_4 / Ti Interface

The reaction between Si_3N_4 and titanium forms the $Ti_5Si_3(N)$ layer adjacent to Si_3N_4. The growth of the layer is dominated by the diffusion of silicon through the $Ti_5Si_3(N)$ layer, indicating that the growth front is located on the metal side of the layer. The solubility of nitrogen in $Ti_5Si_3(N)$ decreases by cooling from the bonding temperature to the ambient temperature. Thus, α-Ti(N) or TiN precipitate in the layer and the precipitation free zones on both sides of the layer are formed during cooling. Ti_5Si_3 is known as a brittle-and-weak phase, whose fracture strength is only 70 MPa [7.7]. In addition, as shown in **Table 7.3**, its thermal expansion mismatch with Si_3N_4 is large ($\Delta\alpha = 7.8\times10^{-6}$) [7.8]. As the result, the joints fracture at the Si_3N_4 / Ti_5Si_3 interface. Therefore, a method to prevent the formation of the $Ti_5Si_3(N)$ layer adjacent to Si_3N_4 is required.

Table 7.3 Thermal expansion coefficients of the phases formed adjacent to Si_3N_4 [7.8].

Phase	Thermal expansion coefficient, α
(Si_3N_4)	(3.2×10^{-6})
Ti_5Si_3	11.0×10^{-6}
V_3Si	10.2×10^{-6}
$V_5Si_3N_{1-X}$	10.0×10^{-6}
$Nb_5Si_3N_{1-X}$	not presented

Fig. 7.3 shows the Ti-Si-N ternary chemical potential diagram at 1573 K. From the diagram, a route to establish the phase sequence from Si_3N_4 to Ti preventing the formation of $Ti_5Si_3(N)$ adjacent to Si_3N_4 is found; to form a layer of TiN adjacent to Si_3N_4. To settle this route of interfacial phase sequence corresponds to a shift of the diffusion path from the observed "natural" path to a higher state of chemical potential of nitrogen. The nitrogen presolution treatment of titanium foils has successfully proven that the artificial modification of the phase

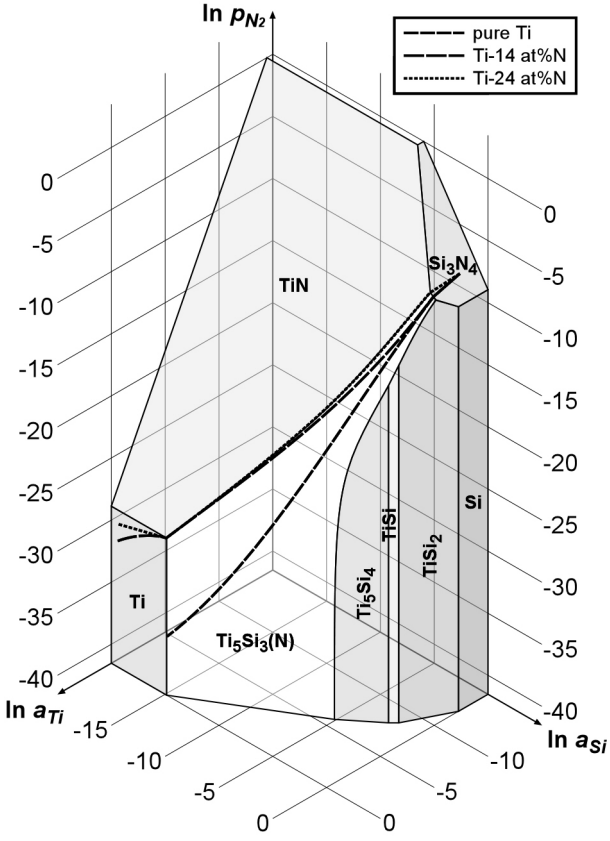

Fig. 7.3 Chemical potential diagram for Ti-Si-N ternary system at 1573 K.

sequence is possible, though it was insufficient for perfect prohibition of the formation of $Ti_5Si_3(N)$. This result indicates that the formation of TiN adjacent to Si_3N_4 from the beginning of the bonding treatment is required. Consequently, a layer of TiN is required to be coated to one side of the bonding surfaces prior to the bonding treatment. Taking into account that TiN is a hard material, the coating to the Si_3N_4 side is preferred, which side is hardly expected to deform plastically to achieve a close fitting at the interface, rather than the titanium metal side. An attention should be paid on the nature of TiN, being stable in a wide range of off-stoichiometric composition [7.9]. This property causes the variation of the chemical potential of nitrogen in the TiN. Therefore, not every TiN layer prevents the formation of $Ti_5Si_3(N)$, but only those having sufficiently high chemical potential of nitrogen, *e.g.*, –101 kJ mol^{-1} at 1573 K. In addition, the measurement of the nitrogen composition in TiN is quite difficult, as described in Chapter 4.

Ishida [7.4, 7.6] and Nomura *et al.* [7.10] have demonstrated the formation of thin TiN layer adjacent to Si_3N_4 using Cu-Ti and Ag-Cu-Ti braze alloys, respectively. The materials they used for bonding were not the high-purity titanium. However, if to persist in keeping the metal side of the joints to be pure titanium is not required, their results present a good suggestion for the control of the interfacial microstructure. That is to reduce the chemical potential of titanium in the filler metal by dilution (*i.e.*, alloying) with some appropriate refractory elements. The chemical potential diagram indicates that a filler alloy with the chemical potential of titanium lower than –138 kJ mol^{-1} will never form $Ti_5Si_3(N)$ at the interface.

B. The Si_3N_4 / V Interface

The interfacial microstructures of Si_3N_4 / V joints change by the bonding time showing five representative stages of phase-sequences. Moreover, the phase sequences at the bonding temperature of 1473 K and below appear different from that at 1498 K and above. The fracture behavior of the joints suggests that these stages of phase-sequences can be divided into two states: the primary state in which the V_3Si layer is formed adjacent to Si_3N_4 and the developed state in which the $V_5Si_3N_{1-X}$ layer is formed adjacent to Si_3N_4. The Si_3N_4 / V_3Si interface in the primary state is thermodynamically metastable, whose equilibrium is achieved

with the formation of the $V_5Si_3N_{1-X}$ layer, *i.e.*, in the developed state. The joints with the interfacial microstructure categorized in the primary state perform a higher fracture strength than those in the developed state. Furthermore, the present research have proven that the maximum performance in the joint strength is achieved when the thickness of the V_3Si layer is 2.0 μm. Therefore, the formation of the V_3Si layer adjacent to Si_3N_4 maintaining its thickness at 2.0 μm and preventing the formation of the $V_5Si_3N_{1-X}$ layer is the proposition of control for this system.

The formation of the 2.0 μm-thick V_3Si layer adjacent to Si_3N_4 can be achieved by ordinary solid state diffusion bonding of Si_3N_4 using high-purity vanadium foils. Taking the transient change of the growth behavior of the V_3Si layer at the temperature between 1473 K and 1573 K into account, the thickness can be predicted on the basis of the parabolic law and the Arrhenius function as follows:

$$\text{at 1473 K and below:} \quad t \,/\, \mathrm{s} = 3.08\times10^{-6} \exp(3.13\times10^{4}\ (T \,/\, \mathrm{K})^{-1}) \,, \tag{7.4}$$

$$\text{at 1573 K and above:} \quad t \,/\, \mathrm{s} = 1.09\times10^{-2} \exp(1.76\times10^{4}\ (T \,/\, \mathrm{K})^{-1}) \,, \tag{7.5}$$

where t and T are the bonding time and temperature, respectively. However, to suppress the further growth of the 2.0-μm-thick V_3Si layer and to prevent the formation of the $V_5Si_3N_{1-X}$ layer is difficult to achieve simultaneously. As shown in Fig. 5.8, the growth of the V_3Si layer will stop and maintain the thickness only by the formation of the $V_5Si_3N_{1-X}$ layer without the V_3Si / V_2N contact. Since the Si_3N_4 / V_3Si interface is metastable, the interface tends to form the $V_5Si_3N_{1-X}$ layer to achieve the local thermodynamic equilibrium. In addition, the growth front of the V_3Si and the $V_5Si_3N_{1-X}$ layers are located on the Si_3N_4 side of each layer, which is different from the case of titanium. Due to this difference in the growth front, to suppress the growth of the $V_5Si_3N_{1-X}$ layer by the nitrogen presolution treatment becomes impossible. The analysis of the evolution behavior of the interfacial microstructure has shown that the formation of the $V_5Si_3N_{1-X}$ layer onsets when the spatial gradient of the chemical potential of vanadium decreases to a value below -3.3×10^{9} J mol^{-1} m^{-1}. This result implies that when a diffusion barrier of vanadium is introduced in order to suppress the growth of the V_3Si layer, the $V_5Si_3N_{1-X}$ layer is formed at the interface, *i.e.*, the contrary effect takes place.

These results suggest that the growth of the V_3Si layer after achieving the thickness of 2.0 μm and the formation of the $V_5Si_3N_{1-X}$ layer are both inevitable. However, the apparent

activation energy for growth of the V_3Si layer at 1473 K and below is considerably high (260 kJ mol^{-1}), indicating that the growth rate of the layer significantly decreases by lowering the operation temperature of the joints. Furthermore, the stability of the Si_3N_4 / V_3Si interface is higher at lower temperatures. The interface is maintained for 57.4 ks at 1473 K, which allows the V_3Si layer to grow up to 6.71 μm (*cf.* Fig. 5.7). On the other hand, the interface is stable for only 1.2 ks at 1673 K, until the thickness of 3.55 μm (*cf.* Fig. 5.8). Thus, the Si_3N_4 / V joints are recommended to be operated at low temperatures below 1473 K, otherwise the strength of the joints is rapidly deteriorated.

C. The Si_3N_4 / Nb Interface

The reaction between Si_3N_4 and niobium forms the $Nb_5Si_3N_{1-X}$ / Nb_5Si_3 layer adjacent to Si_3N_4. The joints fracture at the Si_3N_4 / $Nb_5Si_3N_{1-X}$ interface. Although the fracture strength of the joints changes depending on the bonding time, the strength cannot be clearly correlated with the thickness of the $Nb_5Si_3N_{1-X}$ / Nb_5Si_3 layer. This result implies that the joint strength is dominated by the bond efficiency (η) of the Si_3N_4 / $Nb_5Si_3N_{1-X}$ interface. The fact that the obtained maximum strength of the Si_3N_4 / Nb joints is the highest among the three active metals employed in the present study indicates that the ideal bond strength (σ_f^0) is sufficiently high. Therefore, the change of the joint strength by the bonding time is considered as the effect of change in the actual number of bonds formed at the interface, *n* (*cf.* equations (7.1) and (7.3)). The deterioration of the fracture strength of the joints after achieving the maximum strength is explained by the reduction of *n*, induced by the formation of a thin nitrogen-terminated passive layer during cooling. The phase diagram suggests that the $Nb_5Si_3N_{1-X}$ is no more stable at 1273 K and below [7.11], indicating that the phase releases nitrogen to the Si_3N_4 / $Nb_5Si_3N_{1-X}$ interface during cooling. Since the defects of this type are in atomic-order scale, they are hardly observed on the cross-sectional microstructures by SEM. Consequently, the behavior of nitrogen at the Si_3N_4 / $Nb_5Si_3N_{1-X}$ interface has to be controlled by trapping them in the $Nb_5Si_3N_{1-X}$ phase, *e.g.*, by forming Nb_2N in the layer. This modification of the interfacial microstructure corresponds to shift the phase sequence in the vicinity of Si_3N_4 to a little higher chemical potential of nitrogen (*cf.* Fig. 6.2).

The growth of the Nb_2N grains without being embedded in the $Nb_5Si_3N_{1-X}$ / Nb_5Si_3 layer

indicates that the growth front of the $Nb_5Si_3N_{1-X}$ / Nb_5Si_3 layer is located on the Si_3N_4 side and that the diffusion of niobium is dominating the growth of the layer. The growth behavior of the $Nb_5Si_3N_{1-X}$ / Nb_5Si_3 layer being similar to that of the V_3Si layer in the Si_3N_4 / V system indicates that the nitrogen presolution cannot suppress the growth of the $Nb_5Si_3N_{1-X}$ / Nb_5Si_3 layer. In addition, the phase sequence in the vicinity of Si_3N_4 cannot be raised to a state with higher chemical potential of nitrogen by this method. The Nb_2N grains grow anomalously on the habit plane of the Nb matrix. Their growth rate is suppressed when the grains have grown to contact the opposite side of the interface (*cf.* Fig. 6.5(b)). This result implies that the frequency of Nb_2N nucleation at the Nb_5Si_3 / Nb interface is significantly low. Therefore, to introduce a high-density grain boundaries in the Nb matrix by its grain size refinement is expected to enhance the nucleation. In addition, the increased number of grain boundaries will enhance the diffusion of nitrogen toward niobium, which will reduce the amount of nitrogen released to the Si_3N_4 / $Nb_5Si_3N_{1-X}$ interface.

The utilization of fine-grained niobium inserts, synthesized directly on Si_3N_4 by radio-frequency magnetron sputter deposition, has proven successfully that the interfacial microstructure can be modified to form the Nb_2N as a layer between Nb_5Si_3 and Nb. This result indicates that the frequency of nucleation of Nb_2N is significantly increased. **Fig. 7.4** depicts the change of the interfacial phase sequence on the Nb-Si-N ternary chemical potential diagram at 1673 K. The change appears at the vicinity of Nb. The increase in the frequency of nucleation of Nb_2N allows the system to take a smooth and direct phase sequence between the both end-members.

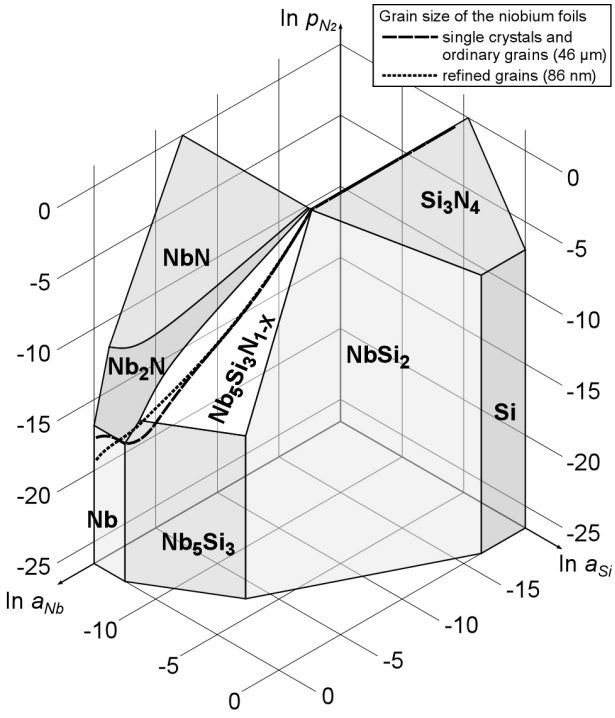

Fig. 7.4 Modification of the interfacial microstructure by grain-size refinement described on the Nb-Si-N ternary chemical potential diagram at 1673 K.

Although the formation of Nb_2N in the $Nb_5Si_3N_{1-X}$ layer is difficult with the grain-

size refinement of the Nb foils, the behavior of nitrogen at the Si_3N_4 / $Nb_5Si_3N_{1-X}$ interface is successfully controlled by this technique. The fracture strength of Si_3N_4 / fine-grained Nb does not deteriorate even after the prolonged bonding time of 57.6 ks at 1673 K, indicating that the nitrogen which works as the bond terminator at the Si_3N_4 / $Nb_5Si_3N_{1-X}$ interface is effectively suppressed.

V. Conclusion

The philosophy to design and control the interfacial microstructure of silicon nitride / active-metal joints by solid state diffusion bonding was discussed. Two techniques for artificial modification of the interfacial microstructures were shown on the basis of the corresponding chemical potential diagrams. The discussion is summarized as follows.

1) The knowledge on the diffusion path, the precise determination of the target phase to control, and the growth behavior of the target phase is essential for appropriate design and control of the interfacial microstructures.
2) The method to control the interfacial microstructure varies by the behavior of the constituent elements at the interface. The behavior of the constituent elements can be understood on the basis of the corresponding chemical potential diagrams.
3) Chemical potential diagrams provide the essential information of the phase sequence and the appropriate route for artificial modification of the sequence.
4) The nitrogen presolution treatment of the active-metals shifts the phase sequence at the interface to a higher side of the chemical potential of nitrogen when the diffusion of silicon is dominating the growth of the target phase.
5) The grain size refinement of the active-metals enhances the diffusion and reaction of the constituent elements by introducing a large amount of grain boundaries, which work as the high-speed route for diffusion and the efficient nucleation sites for reaction products. This property of grain boundaries modifies the phase sequence on the chemical potential diagram to a smoother path which the both end-members of the system can take.

References

[7.1] T. Suga: *Bull. Jpn. Inst. Met.*, 1990, Vol. 29, pp. 944-947, in Japanese.

[7.2] T. Suga, Y. Takahashi, H. Takagi, B. Gibbesch and G. Elssner: *Acta Metall. Mater.*, 1992, Vol. 40, Suppl., pp. S133-S137.

[7.3] T. Suga: *Bull. Ceram. Soc. Jpn.*, 1995, Vol. 30, pp. 106-109, in Japanese.

[7.4] Y. Ishida: *Bull. Jpn. Inst. Met.*, 1990, Vol. 29, pp. 888-892, in Japanese.

[7.5] Y. Ishida, J.-Y. Wang and T. Suga: *ISIJ Int.*, 1990, Vol. 30, pp. 1041-1045.

[7.6] Y. Ishida, J. Wang and T. Suga: *Acta Metall. Mater.*, 1992, Vol. 40, Suppl., pp. S289-S293.

[7.7] T. Iseki, T. Yano and Y.S. Chung: *J. Ceram. Soc. Jpn.*, 1989, Vol. 97, pp. 710-714, in Japanese.

[7.8] J.C. Schuster, F. Weitzer, J. Bauer and H. Nowotny: *Mater. Sci. Eng.*, 1988, Vol. A105/106, pp. 201-206.

[7.9] *Phase Diagrams of Ternary Boron Nitride and Silicon Nitride Systems*, P. Rogl and J.C. Schuster (Eds.), ASM International, Materials Park, Ohio (USA), 1992, pp. 198-202.

[7.10] M. Nomura, C. Iwamoto and S.-I. Tanaka: *Acta Mater.*, 1999, Vol. 47, pp. 407-413.

[7.11] *Phase Diagrams of Ternary Boron Nitride and Silicon Nitride Systems*, P. Rogl and J.C. Schuster (Eds.), ASM International, Materials Park, Ohio (USA), 1992, pp. 172-174.

Chapter 8 Conclusion

The present research was implemented to clarify the interfacial microstructure and the reaction behavior at the silicon nitride / active metal interface and to propose some methods to control the interfacial microstructure for solid state diffusion bonding, on the basis of metallurgical thermodynamics and diffusion and reaction theories.

In Chapter 1, the motivation of the author to conduct the present research was expressed at first. Then, the properties of silicon nitride was compared with those of other fine-ceramic materials to show the potential of silicon nitride as the high-temperature structural material for the next generation and the current issues for practical application of silicon nitride to structural components. The bonding of silicon nitride with metallic materials was extracted as the severest problem. In the next step, the science and technology of ceramic / metal bonding was overviewed extensively. Short in the basic knowledge on the interfacial microstructure and the interfacial reaction was extracted as the factor obstructing to control the interfacial microstructure of the joints and to predict and assess the performance and life of the joints.

In Chapter 2, the basic theories of metallurgical thermodynamics, diffusion, reaction, X-ray diffraction and electron-probe microanalysis, on which the present research stands, were described.

In Chapter 3, the detailed experimental procedure employed in the present research was described.

In Chapter 4, solid state diffusion bonding of silicon nitride using titanium foils containing different amounts of nitrogen as solute was investigated. The interfaces of the joints were analyzed by means of SEM, EPMA and XRD. The strength of the joints was estimated by a shear fracture test. The following points are clarified.

1) The interfacial phase sequence of Si_3N_4 / pure-Ti joint bonded at each employed temperature is identified as follows:

   at 1473 K: Si_3N_4 / Ti_5Si_3 / Ti_5Si_3 + α-Ti(N) / α-Ti(N) + Ti_5Si_3,

   at 1573 K: Si_3N_4 / Ti_5Si_3 / Ti_5Si_3 + α-Ti(N) / Ti_5Si_3 / α-Ti(N) + Ti_5Si_3,

   at 1673 K: Si_3N_4 / Ti_5Si_3/ Ti_5Si_3 + TiN / Ti_5Si_3 / α-Ti(N) + Ti_5Si_3.

   However, the actual phase sequence at those bonding temperatures is described as;

   Si_3N_4 / Ti_5Si_3(N) / α-Ti (N) + Ti_5Si_3(N).

2) The strength of the Si_3N_4 / pure Ti joint bonded at 1573 K for 3.6 ks is 3.5 MPa. The fracture occurs at the Si_3N_4 / Ti_5Si_3 interface.

3) The Ti_5Si_3 layer grows according to the parabolic law until the nitrogen content in the remaining α-Ti phase reaches the value of C_N*, which is a function of the bonding temperature. After achievement of C_N*, the growth of the Ti_5Si_3 layer stops.

4) The use of nitrogen presolved Ti foil effectively suppresses the growth of the Ti_5Si_3 layer. The phase adjacent to Si_3N_4 changes from a Ti_5Si_3 single phase to a Ti_5Si_3 + TiN mixed phase. The formation of granular Ti_5Si_3 on Ti grain boundaries is completely prevented.

5) Joints of Si_3N_4 / Ti - 24at% N have a fracture strength of 10.6 MPa, which is three times higher than that of Si_3N_4 / pure Ti joints bonded under the same condition. The fracture path is changed to Si_3N_4 / Ti_5Si_3 and TiN / Ti_5Si_3 interfaces.

In Chapter 5, solid state diffusion bonding of silicon nitride using vanadium foils was investigated. The interfacial microstructure and reaction kinetics were analyzed in detail by means of SEM, EPMA and XRD. The strength of the joints was estimated by a shear fracture test. The following points were clarified.

1) The interfacial phase sequence of the Si_3N_4 / V joints bonded at 1473 K and below changes revealing four stages of transition as follows:

   (i) Si_3N_4 / V_3Si / V+V_2N / V,

(ii) Si_3N_4 / $V_5Si_3N_{1-X}$ / V_3Si / V+V_2N,

(iii) Si_3N_4 / $V_5Si_3N_{1-X}$ / V_3Si / V_2N, and

(iv) Si_3N_4 / $V_5Si_3N_{1-X}$ / V_2N + VN / V_2N.

At the bonding temperatures of 1498 K and higher, the V_2N grains are prohibited to contact with the V_3Si layer by the V(Si) zone. At these temperatures, five stages of transition in the interfacial phase sequence are observed as follows:

(i) Si_3N_4 / V_3Si / V(Si) / V+V_2N,

(ii) Si_3N_4 / $V_5Si_3N_{1-X}$ / V_3Si / V(Si) / V+V_2N,

(iii) Si_3N_4 / $V_5Si_3N_{1-X}$ / V_3Si / V_2N,

(iv) Si_3N_4 / $V_5Si_3N_{1-X}$ / V_2N + VN / V_2N, and

(v) Si_3N_4 / $V_5Si_3N_{1-X}$ / VN.

The Si_3N_4 / V_3Si interface observed in the first stage is metastable. These phase sequences except the metastable interface are successfully expressed on the proposed chemical potential diagram.

2) The growth front of the V_3Si layer is located on the Si_3N_4 side, indicating that the diffusion of vanadium through the V_3Si layer dominates the growth of the layer.

3) The increase and decrease behavior in the thickness of each reaction product interacts with each other. Every reaction product grows obeying the parabolic law in its initial stage of growth. The pre-exponential growth constant and the activation energy for the growth of the V_3Si layer appear different between the high- and low-temperature bonding conditions. The formation of the $V_5Si_3N_{1-X}$ layer starts when the spatial gradient of the chemical potential of vanadium in the V_3Si layer decreases to a value below -3.3×10^9 J mol^{-1} m^{-1} by the growth of the V_3Si layer.

4) The maximum fracture strength is achieved when the thickness of the V_3Si layer is 2.0 μm. The higher bonding temperature leads to the higher maximum fracture strength. The fracture of the joints bonded at this condition occurs in a brittle mode mainly at the Si_3N_4 / V_3Si interface and partly inside the V_3Si layer. The prolonged bonding time gradually reduces the fracture strength down to 42 MPa. The joints are fractured at the $V_5Si_3N_{1-X}$ in the vicinity of the Si_3N_4 / $V_5Si_3N_{1-X}$ interface by crack propagation connecting the voids.

In Chapter 6, solid state diffusion bonding of silicon nitride using niobium foils with various initial grain size was investigated. The interfacial microstructure and reaction behavior were analyzed by means of SEM, EPMA and XRD and considered on the basis of the Nb-Si-N ternary chemical potential diagram. The strength of the joints was estimated by a shear fracture test. The following points were clarified.

1) The interfacial phase sequence is considered to be Si_3N_4 / $Nb_5Si_3N_{1-X}$ / Nb_5Si_3 / Nb_2N + Nb / Nb. The phase sequence does not change by changing the bonding temperature and time in the range from 1573 K to 1773 K and from 3.6 ks to 32.4 ks, respectively.
2) The reaction products grow monotonously obeying the parabolic law. The values of the pre-exponential factor for the growth rate and the apparent activation energy for the growth of the $Nb_5Si_3N_{1-X}$ / Nb_5Si_3 layer are 6.1×10^{-10} m^2s^{-1} and 2.0×10^2 kJ mol^{-1}, respectively, while those of the Nb_2N grains are 1.2×10^{-7} m^2s^{-1} and 2.7×10^2 kJ mol^{-1}, respectively.
3) The maximum fracture strength of 131 MPa was obtained with the joints bonded at 1573 K for 14.4 ks. The strength changes sensitively to the bonding time, when the joints are bonded at 1573 K. However, the change becomes mild when they are bonded at 1673 K. The fracture occurs at the Si_3N_4 / $Nb_5Si_3N_{1-X}$ interface in a brittle mode.
4) The interfacial microstructure of the joints bonded using fine-grained (86 nm-diameter) films of niobium appears with the phase sequence of Si_3N_4 / $Nb_5Si_3N_{1-X}$ / Nb_5Si_3 / Nb_2N / Nb+Nb_2N, which is different from those bonded using ordinary polycrystalline (46 μm-diameter) foils or single-crystal foils. The growth rate of the $Nb_5Si_3N_{1-X}$ / Nb_5Si_3 layer is slightly enhanced by the grain refinement, as the result of competitive two mechanisms: the enhancement of grain boundary diffusion and the formation of the Nb_2N diffusion barrier layer. The interfacial microstructure and the growth rate of the reaction products of the joints using ordinary polycrystalline foils and single crystals appear almost the same.
5) The joints bonded using deposited films of niobium retain high fracture-strength of 100 MPa even after a prolonged bonding treatment of 57.6 ks at 1673 K.

In Chapter 7, a general discussion is performed on the interfacial microstructure, reaction behavior, the joint strength and fracture path and the philosophy to control the interfacial microstructure, on the basis of the research achievements obtained in the present

study. Through the discussion, the following conclusions were obtained:

1) The knowledge on the diffusion path, the precise determination of the target phase to control, and the growth behavior of the target phase is essential for appropriate design and control of the interfacial microstructures.
2) The method to control the interfacial microstructure varies by the behavior of the constituent elements at the interface. The behavior of the constituent elements can be understood on the basis of the corresponding chemical potential diagrams.
3) Chemical potential diagrams provide the essential information of the phase sequence and the appropriate route for artificial modification of the sequence.
4) The nitrogen presolution treatment of the active-metals shifts the phase sequence at the interface to a higher side of the chemical potential of nitrogen when the diffusion of silicon is dominating the growth of the target phase.
5) The grain size refinement of the active-metals enhances the diffusion and reaction of the constituent elements by introducing a large amount of grain boundaries, which work as the high-speed route for diffusion and the efficient nucleation sites for reaction products. This property of grain boundaries modifies the phase sequence on the chemical potential diagram to a smoother path which the both end-members of the system can take.

In Chapter 8, the achievements of the present research are summarized.

Acknowledgement

First of all, I express my gratitude to Prof. Masaaki Naka, Prof. Shiro Kubo, Prof. Shinsaku Hanasaki, Prof. Kazutoshi Nishimoto and Prof. Hirotaro Mori for their critical suggestion and advice to this thesis.

To be my pleasure, I express my sincere gratitude to Prof. Julius Clemens Schuster, Prof. Feng Ji Cai, Prof. Toshiya Shibayanagi, Prof. Kazuyoshi Saida, Prof. Hidetoshi Fujii, Prof. Tadatomo Suga, Prof. Naoe Hosoda, Dr. Reinder Hindrik Vegter, Mr. Osamu Igarashi, Mr. Ryozo Oomoto, Mr. Daisuke Baba, Mr. Ichiji Nakade, the late Mr. Toshiro Nakatsuka, Mr. Tsuneo Sakai, Dr. Harumi Yokokawa, and Dr. Takashi Fukai for their powerful support and fruitful discussion. In many tough situations during this work, Prof. Hiroyuki Yasuda, Dr. Takao Sakata, Prof. You-Chul Kim, Prof. Manabu Tanaka, Mr. Akio Takahashi, Prof. Yuichi Setsuhara, Prof. Hisashi Serizawa, Prof. Masahiro Tsukamoto, Prof. Yoshihiro Sakino, Prof. Taihei Matsumoto, Prof. Takuya Tsumura, Prof. Makoto Takahashi, Prof. Em. Yasushi Kikuchi, Prof. Kiyoshi Nogi, Prof. Masao Ushio, Prof. Kenji Ikeuchi, Mr. Hirosato Sakai, Mr. Masahiko Hirono, Mr. Hiroshi Miyake, Mr. Takeyuki Katsumata, Mr. Michiyuki Nakazaki, Mr. Toshiyuki Yoshikawa, Dr. Akinori Inoue, Mr. Hideyuki Hirota, Dr. Masakazu Mori, Mr. Hiroshi Uozumi, Mr. Tatsushi Okamoto, Mr. Kazuyuki Tenyama, Mr. Akinobu Yoshimura, Mr. Daisuke Watanabe, Mr. Tōru Okada, Mr. Tohru Sekido, Dr. Yasuhiro Aoki, Prof. Akio Nishimoto, and so many classmates, friends and colleagues in recent and past of the Joining and Welding Research Institute, Osaka University have advised, stimulated, and supported me technically, mentally and financially.

The final column in this acknowledgement, my best wishes are expressed to my wife, parents, brothers and sisters for their love, support and patience. Especially, my wife Naoko, who has been kept enduring so irregular life-style of mine, is far beyond praise.

List of Publication Related to the Present Study

Chapter 1

1) M. Maeda: "Overview of Research on Welding in Japan, Section II-3-1 Ceramics", *J. Jpn. Weld. Soc.*, 1997, Vol. 66, pp. 341-342, in Japanese.
2) M. Maeda: "Overview of Research on Welding in Japan, Section II-3-1 Ceramics", *J. Jpn. Weld. Soc.*, 1998, Vol. 67, pp. 386-388, in Japanese.
3) M. Maeda: "Overview of Research on Welding in Japan, Section II-3-1 Ceramics", *J. Jpn. Weld. Soc.*, 1999, Vol. 68, pp. 358-360, in Japanese.
4) M. Maeda: "Overview of Research on Welding in Japan, Section II-4-1 Ceramics", *J. Jpn. Weld. Soc.*, 2000, Vol. 69, pp. 387-389, in Japanese.
5) M. Maeda: "Overview of Research on Welding in Japan, Section II-4-1 Ceramics", *J. Jpn. Weld. Soc.*, 2001, Vol. 70, pp. 520-522, in Japanese.
6) M. Maeda: "Overview of Research on Welding in Japan, Section II-4-1 Ceramics", *J. Jpn. Weld. Soc.*, 2002, Vol. 71, pp. 329-330, in Japanese.
7) M. Maeda: "Overview of Research on Welding in Japan, Section II-4-1 Ceramics", *J. Jpn. Weld. Soc.*, 2003, Vol. 72, pp. 358-359, in Japanese.

Chapter 4

8) M. Maeda, R. Oomoto, T. Shibayanagi and M. Naka: "Solid-State Diffusion Bonding of Silicon Nitride using Titanium Foils", *Metall. Mater. Trans. A*, 2003, Vol. 34, pp. 1647-1656.
9) M. Maeda, R. Oomoto, T. Shibayanagi and M. Naka: "Solid State Diffusion Bonding of Si_3N_4 with Ti Foil", *Proc. Int. Conf. on Processing and Manufacturing of Advanced Materials* (THERMEC 2000), Las Vegas (USA), Dec. 2000, CDROM: Session G2, *J. Mater. Process. Technol.*, Special Issue, Elsevier Science, 2001.

10) M. Maeda, R. Oomoto, T. Shibayanagi and M. Naka: “Reaction Control during Solid State Diffusion Bonding of Si_3N_4 with Ti Foil”, *Proc. 6th Int. Conf. on Brazing, High Temperature Brazing and Diffusion Bonding* (LÖT 2001), Aachen (Germany), May 2001, pp. 284-287.
11) M. Maeda and M. Naka: “Reaction and Structure at the Solid State Diffusion Bonded Ti / Si_3N_4 Interface”, *Trans. JWRI*, 1997, Vol. 26, No. 2, pp. 23-26.
12) M. Maeda, R. Oomoto, M. Naka and T. Shibayanagi: “Interfacial Reaction between Titanium and Silicon Nitride during Solid State Diffusion Bonding”, *Trans. JWRI*, 2001, Vol. 30, No. 2, pp. 59-65.

Chapter 5

13) M. Maeda, O. Igarashi, T. Shibayanagi and M. Naka: “Solid State Diffusion Bonding of Silicon Nitride using Vanadium Foils”, submitted to *Mater. Trans.*
14) M. Maeda, O. Igarashi, T. Shibayanagi and M. Naka: “Relation between Interfacial Structure and Strength of Solid State Diffusion Bonded V / Si_3N_4 Joints”, *Proc. Int. Symp. on Environment-Conscious Innovative Materials Processing with Advanced Energy Sources* (ECOMAP-98), Kyoto (Japan), Dec. 1998, pp. 589-594.

Chapter 6

15) M. Maeda, D. Baba, T. Shibayanagi and M. Naka: “Solid State Diffusion Bonding of Si_3N_4 using Nb Foils”, *Proc. 7th Int. Welding Symp.* (7WS), Kobe (Japan), Nov. 2001, pp. 899-904.
16) M. Maeda, T. Shibayanagi, D. Baba and M. Naka: “Interfacial Structure of Solid State Diffusion Bonded Silicon Nitride Joints Using Grain Size Controlled Niobium Foils”, *Proc. Int. Conf. on Designing of Interfacial Structures in Advanced Materials and their Joints* (DIS'02), Osaka (Japan), Nov. 2002, pp. 557-561.
17) M. Maeda, T. Shibayanagi, D. Baba and M. Naka: “Interfacial Microstructure of Solid State Diffusion Bonded Silicon Nitride using Niobium Foils”, *JOINING & WELDING SOLUTION TO INDUSTRIAL INNOVATION, Proc. 30th Anniversary Int. Symp. Join. Weld. Res. Inst.*, Osaka (Japan), Mar. 2003, pp. 213-214.

Award

1) **DVS AWARD**, LÖT 2001, 08 May 2001, for "Reaction Control during Solid State Diffusion Bonding of Si_3N_4 with Ti Foil", appeared in *Proc. Int. Conf. on Brazing, High Temperature Brazing and Diffusion Welding*, DVS, Aachen (Germany), 8-10 May 2001, pp. 284-287.